A Measurement of α_s from the Gross-Llewellyn Smith Sum Rule

John H. Kim
Columbia University, New York, NY

September 28, 1998

Abstract

A set of values for the Gross-Llewellyn Smith sum rule are extracted at different values of 4-momentum transfer squared (Q^2), by combining revised CCFR neutrino data with data from other neutrino deep-inelastic scattering experiments for $1 < Q^2 < 15 \;\; GeV^2/c^2$. A comparison with the order α_s^3 theoretical predictions yields a determination of the α_s at the scale of the Z-boson mass of $\alpha_s(M_Z^2) = 0.114 \pm^{.009}_{.012}$. This measurement tests perturbative Quantum Chromodynamics at low Q^2 with a precise level of theoretical understanding.

Contents

1 Introduction **1**

1.1 The Standard Model 2

The Proton 3

The Neutrino 3

Organization 4

1.2 Structure Functions and Deep Inelastic Scattering 4

Kinematics of Scattering 5

The Quark Parton Model 7

General Structure Functions 9

The GLS Sum Rule 10

1.3 Quantum Chromodynamics 10

Features of QCD 11

Perturbative QCD Corrections 14

Non-perturbative QCD Corrections 15

QCD Prediction of GLS 16

2 Neutrino Beamline **17**

2.1 Beam Extraction 17

2.2 Secondary Beam and Magnet Train 19

2.3 Decay region 20

2.4 Neutrino Spectrum 21

3 The CCFR Detector **23**

3.1 Scintillation Counters . . . 23
3.2 Phototubes and Readout . . . 24
3.3 Drift Chambers . . . 27
3.4 Toroid Spectrometer . . . 29
3.5 Triggering . . . 30
3.6 Data Acquisition . . . 31

4 Event Reconstruction **33**

4.1 Pulse Heights . . . 33
Counter Gain Calibration . . . 34
Map and Time Variation Corrections . . . 35
Identifying Calorimeter Regions . . . 37
4.2 Hadron Energy Measurement . . . 38
Converting MIPs to Energy . . . 38
Parameterized Muon Subtraction . . . 40
4.3 Muon Tracking . . . 41
4.4 Muon Energy Measurement . . . 44
4.5 Analysis Cuts . . . 45
Fiducial Volume Cuts . . . 45
Dimuon Cut . . . 46
Geometric Cuts . . . 47
Cross-sectional Cuts . . . 48
Structure-Function Cuts . . . 48

5 Event Monte Carlo **49**

5.1 Purpose . . . 49
5.2 Methodology . . . 50
5.3 Overview . . . 50
5.4 Muon Tracking . . . 52
Muon dE/dX Calculation . . . 52

Muon Scattering Calculation . . . 53
5.5 Muon Energy Smearing . . . 53
Spectrometer Simulation (E_μ^{FF}) . . . 53
Muon Pulse Heights . . . 54
Within the Shower Region . . . 55
5.6 Hadron Energy Smearing . . . 56
Hadronic Component . . . 56
Simulated Muon Response . . . 56
5.7 Simulated Cuts . . . 57

6 Physical Models **58**
6.1 Iteration Procedure . . . 58
6.2 Cross-section and Buras Gaemers Fitting . . . 60
Quark Parton Distributions . . . 60
Choice of Functions in x . . . 62
Scaling in Q^2 . . . 63
Systematic Error . . . 65
Previous Models . . . 70
6.3 Flux Extraction Procedure . . . 73

7 Integration of xF_3 **77**
7.1 Data Handling . . . 77
Combining Experiments . . . 79
Target Mass Correction . . . 79
Calculating the Integral . . . 80
7.2 Low-x Extrapolation . . . 81
Regge Theory . . . 81
Fitting Procedure . . . 82
Estimating Fitting Error . . . 83
7.3 High-x Interpolation . . . 83

SLAC F_2 Data 84
Estimating Fitting Error 85
Quasi-elastic Term 85
7.4 Systematic Errors 86

8 Extraction of α_s and Conclusions **87**
8.1 GLS Theory 87
Perturbative Terms 88
Calculating Alpha 89
Higher Twist 89
8.2 Fitting Procedure and Results 92
Systematic Uncertainties 93
8.3 Comparison to other Measurements and Conclusions 94
8.4 Conclusions 95

A The CCFR/NuTeV Collaboration **101**

B Structure Function Tables **102**

C Detector Material **114**
C.1 Calculating Correct LENGTH 115
C.2 Previous Estimates 116

List of Figures

1.1 Neutrino-nucleon deep inelastic scattering as observed in the laboratory frame, with measured variables noted. . . . 5

1.2 Neutrino-nucleon deep inelastic scattering from a theoretical perspective. . . . 6

1.3 Possible helicity configurations for high-energy neutrinos and anti-neutrinos scattering from quarks and anti-quarks. . . . 8

1.4 QCD field theory diagrams and their mathematical meaning. . . . 11

1.5 The running coupling constant α_s as a function of Q^2. . . . 14

1.6 Sketch illustrating perturbative versus non-perturbative effects. . . . 15

2.1 Fermilab neutrino beamline layout. . . . 18

2.2 Tevatron magnet current cycle versus time. . . . 19

2.3 Quad triplet magnet train. . . . 20

2.4 The fully corrected flux $\times$ energy spectra for E744 and E770. The normalization along the left axes is arbitrary. . . . 21

3.1 Overhead view of the CCFR detector. . . . 24

3.2 Side view of a CCFR target unit. . . . 25

3.3 Front and side views of a CCFR scintillation counter. . . . 26

3.4 Readout electronics for a single scintillation counter. . . . 27

3.5 Sketch of a CCFR target drift chamber. . . . 28

4.1 Contours of the relative muon response for counter 1. . . . 36

4.2 Pulse heights of an event versus counter number, showing vertex PLACE and shower parameter SHEND. . . . 37

4.3 Energy response of the CCFR calorimeter, relating MIPs to GeV. . . . 39

4.4 Distribution of reconstructed test beam hadronic energy. 40
4.5 The fitted energy resolution for all test beam runs. 41

5.1 Muon momentum resolution in the toroid spectrometer. 54

6.1 Flowchart of the iterative analysis procedure. 59
6.2 Conceptual diagram of valence quark function in x. 62
6.3 Extracted F_2 data and best BGPAR fit for $x > 0.06$. 66
6.4 Extracted F_2 data and best BGPAR fit for $x < 0.06$. 67
6.5 Extracted xF_3 data and best BGPAR fit for $x < 0.1$. 68
6.6 Extracted xF_3 data and best BGPAR fit for $x > 0.1$. 69
6.7 Comparison of different BGPAR fits on F_2 vs x. 71
6.8 Comparison of different BGPAR fits on xF_3 vs x. 72
6.9 B/A as a function of energy for experiment E744. 75
6.10 The fully corrected flux × energy spectra for E744 and E770. 76

7.1 The range of each experiment in x and Q^2. 78
7.2 Target mass correction function. 80
7.3 Combined data for $xF_3(x)$ showing the low-x fit. 82
7.4 High-x data for combined xF_3 and fits. 84

8.1 The data for the GLS integral as a function of Q^2. 88
8.2 α_s as a function of $\Lambda_{\overline{MS}}^{(5)}$. 90
8.3 Two-loop and three-loop predictions for $\alpha_s(Q^2)$. 91
8.4 $\alpha_s(Q^2)$ for different experiments. 96
8.5 $\alpha_s(M_Z^2)$ for different experiments. 97

List of Tables

1.1 The fundamental particles of matter: quarks and leptons. 2

1.2 The four fundamental forces and their properties. 3

3.1 Number of triggers written to tape in E744 and E770. 31

4.1 Calibration constants and energy resolution of the CCFR detector. 42

4.2 Constants A and B for muon angular resolution. 43

4.3 Definitions and rejection rates of the analysis cuts. 46

6.1 The final parameters for the best BGPAR fit. 63

6.2 The final parameters for the alternate BGPAR fit. 65

6.3 The χ^2/DOF for each BGPAR fit. 71

7.1 Results from fitting $x < 0.1$ to Ax^B and $Cx^{0.5}$. 83

7.2 Results from fitting $x > 0.5$ to $D(1-x)^E$ and $F(1-x)^3$. 85

7.3 Contributions to the GLS integral from different regions of x 86

8.1 The total GLS integral and α_s for each bin in Q^2. 93

8.2 Uncertainties in $\alpha_s(M_Z^2)$. 94

B.1 F_2 and xF_3 for the central GLS result, including their associated statistical errors. . 102

B.2 F_2 and xF_3 for the acceptance model systematic error. 107

B.3 xF_3 data from BEBC/Gargamelle [Amm78]. 111

B.4 xF_3 data from FNAL-E180 [Amm82]. 112

B.5 xF_3 data from SKAT [Amm86]. 112

B.6 xF_3 data from WA25 [All85]. 113

B.7 xF_3 data from WA59 [Var87]. 113

C.1 Detector material summary table. 117

Chapter 1

Introduction

In essence, this thesis is a measurement of the strength of the strong nuclear force which binds the proton. This is designed as a test of the current theory of the strong nuclear force, known as Quantum Chromodynamics or QCD. If our understanding of QCD is accurate, then this measurement should confirm other measurements done of the strength by different methods. By comparison, this method is better understood and has fewer assumptions than many of the other methods.

The data for this measurement is from an experiment which measures the scattering of high-energy neutrinos off of iron. The experiment, known as CCFR, was conducted at the Fermi National Accelerator Laboratory from 1985 to 1988. Neutrinos are common elementary particles found throughout space, but they interact so rarely that the average solar neutrino will pass through the entire diameter of the Earth without interacting.

This data is used to extract the structure of the proton based on how neutrinos scatter off of it using simple mechanical principles (relativistic spin mechanics). We then calculate a total for part of this structure – the Gross-Llewellyn Smith (GLS) integral – and compare it to what QCD theory claims. This comparison is known as the GLS Sum Rule.

Of course, there are other ways to measure the strong nuclear force. The strength of this technique is primarily in the nature of neutrino scattering. The scattering process is simple and well understood. Also, neutrinos only interact with a specific fraction of the proton, allowing us to see more directly the part we are interested in. Lastly, neutrinos interact much more rarely than any other particle. Thus, we are virtually guaranteed that the neutrino interaction we see will not be complicated by other neutrino reactions (known as "radiative corrections").

On the other side, the theoretical calculation for the GLS Sum Rule is much more complete than most comparable calculations. It is calculated to a high degree and does not depend on the choice of model nearly as much as many other QCD calculations.

1.1 The Standard Model

The Standard Model is a term for the dominant view of particle physics developed over the past two decades. It postulates 12 fundamental particles of matter and their 12 antimatter counterparts. These are known as fermions, for their property of spin-1/2 which defines the statistics of how they interrelate. In addition are five fundamental particles which mediate their interactions, called bosons for their being spin-1. The Standard Model includes the unified theory of electroweak interactions along with Quantum Chromodynamics, the dominant theory of strong interactions. What follows is a brief summary.

The fermions of the standard model are listed in the table below. They are broken up into quarks and leptons. Quarks are the constituents of protons and neutrons – they interact primarily through the strong nuclear force. However, they also interact through the electromagnetic and weak nuclear forces.

Leptons include electrons and neutrinos. They do not interact at all through the strong nuclear force, which makes them ideal probes of how that force operates. Charged leptons include the electron and its heavier cousins the muon and tau – these interact through both the electromagnetic and weak nuclear forces. Neutral leptons are called neutrinos – they interact only through the weak nuclear force and thus have an extremely clean signature.

	Electric Charge	First Generation	Second Generation	Third Generation
Quarks	+2/3	up(u)	charm(c)	top(t)
	-1/3	down(d)	strange(s)	bottom(b)
Leptons	-1	election(e)	muon(μ)	tau(τ)
	0	e-neutrino(ν_e)	μ-neutrino(ν_μ)	τ-neutrino(ν_τ)

Table 1.1: The fundamental particles of matter: quarks and leptons.

The table shows the 12 matter fermions broken up into three generations – each of which has an anti-matter partner. The first generation are the most common particles in the world around us, including the majority of protons and neutrons. The higher generations are higher mass and tend to decay quickly.

The fermions interact through four forces, which in particle physics are represented by the exchange of particles known as gauge bosons. The strong nuclear force is carried by gluons, which interact only with quarks and other gluons. The electromagnetic force is carried by photons, which interact with all charged fermions (i.e. all fermions except neutrinos). The weak nuclear force operates between all fermions, and is carried by three bosons: the $W+$, Z_0, and $W-$. It is notable in neutrinos because these are the only way that neutrinos interact.

Most of these forces have an associated quantum field theory, which lets us understand how energy fluctuates into matter and vice-versa. On the quantum level, we view the force as being carried by particles called bosons: these carry the attractive or repulsive force between particles.

Force	Carried by:	Acts on:	Standard Model Field Theory	Responsible for:
Strong	gluons	quarks	Quantum Chromodynamics	Binding protons and nuclei
Weak	$W\pm$,Z	all	Electroweak Symmetry Breaking	Nuclear decays
Electromagnetic	photons	charged	Quantum Electrodynamics	Binding atoms, molecules, solids
Gravity	graviton(?)	all	none	Binding solar system, galaxies

Table 1.2: The four fundamental forces and their properties.

The electromagnetism is mediated by the photon; the strong nuclear force is mediated by a boson called the gluon; the weak nuclear force is carried by a set of heavy bosons called the $W+$, $W-$, and Z_0. Gravity is not currently understood at the quantum level, and its hypothetical boson (the graviton) has not been observed.

The Proton

In the Standard Model, the proton is formed at base from two up quarks and one down quark (known as the *valence quarks*). This set of three quarks forms a bound state, held together by the strong nuclear force. In quantum theory, this force is represented by the exchange of virtual gluons between the quarks.

These virtual gluons have a very limited range, as they must interact (becoming real) in a time span roughly given by the Heisenberg Uncertainty Principle (i.e. $t \sim \hbar/E$). Further, a gluon can also briefly fluctuate into a quark paired with an antiquark, provided that the pair as a whole have the same quantum numbers as the original gluon. Unless interacted with, these will recombine into the gluon on a similar time scale.

In quantum theory, then, the structure of the proton is complicated first by the gluons, and second by the constantly forming and recombining quark-antiquark pairs. This latter phenomena is known as the quark-antiquark *sea*.

The Neutrino

In theory, the neutrino is the ideal probe of the proton. The proton is frequently studied by scattering charged particles like electrons and muons. These make good probes because they are point particles, and because the electromagnetic force which they usually interact by is well understood.

The neutrino is also a point particle, interacting through the weak nuclear force which is also

well understood. Whereas charged particles can interact through both the electromagnetic and weak nuclear force, the neutrino only interacts weakly. Because the interaction is weak, the probabilities of secondary interactions are smaller than for charged particles. This means that in general, smaller correction factors (*radiative corrections*) are needed to modify the basic cross-section. Thus, an individual neutrino scattering is cleaner than an individual charged particle scattering.

On a practical side, however, neutrinos are difficult to produce in the quantities necessary for statistically precise measurements. Precision experiments must be geared to maximize the number of measured interactions rather than precision measurement. The incident beams are high-intensity but not well measured, and the detectors are extremely massive and coarsely-grained.

Organization

This thesis is broken up into eight chapters, which will cover the steps in the measurement of α_s. The current introductory chapter provides the theoretical background for understanding the GLS sum rule. The remaining chapters will cover in order the collection and analysis of experimental data and each of the steps taken in analyzing that data.

- Chapters 2 and 3 describes the experimental apparatus for creating a high-energy neutrino beam and measuring neutrino interactions.
- Chapters 4 and 5 describes the methods for reconstructing the physics of the neutrino interaction based on the raw data from the detector.
- Chapter 6 outlines the physics models which we use to interpret the reconstructed events.
- Chapter 7 covers how we integrate the experimentally-measured structure function xF_3 to get the GLS integral.
- Chapter 8 explains the theoretical prediction for the Gross-Llewellyn Smith integral and how we compare it to the experimentally-measured integral to extract a value for the strong coupling constant: α_s.

1.2 Structure Functions and Deep Inelastic Scattering

The data for this thesis comes from a single basic physical process, the scattering of high-energy neutrinos off of nucleons. An incoming high-energy muon-neutrino passes through the nucleus, and interacts with it via the weak nuclear force. The neutrino emits a virtual W-boson and is transformed into a muon. The nucleus receives the transfered momentum of the W-boson. At the energies used here, the nucleon is almost always blown apart into a shower of hadrons by the scattering. This is known as "deep inelastic scattering."

A view of this reaction in the laboratory frame is shown in Figure 1.1. The single outgoing muon is sufficiently distinct that we can measure both the angle and energy. The hadron shower is diffuse and reacts quickly, thus we can only measure the total energy of it.

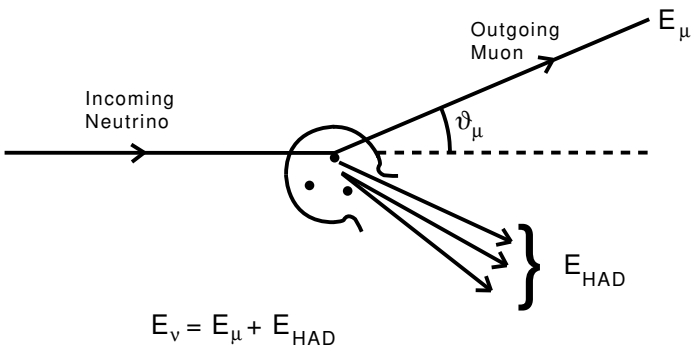

Figure 1.1: Neutrino-nucleon deep inelastic scattering as observed in the laboratory frame, with measured variables noted.

Figure 1.2 shows this reaction in theoretical terms. The weak nuclear interaction is represented by a W-boson with 4-momentum q. The W-boson is virtual, having effectively a negative mass.

Kinematics of Scattering

In general, any scattering process involves 4 vector quantities: the momentum of the scatterer and the momentum of the target, both before and after the reaction. In deep inelastic scattering, the mass of the hadronic final state is also unknown. This is 13 degrees of freedom (DOF). One vector (3 DOF) can be derived from the others by conservation of momentum. One scalar (1 DOF) can be derived by conservation of energy.

In deep-inelastic scattering, we assume that the proton is at rest, or that the momentum of the proton is much less than the other momenta. This accounts for another vector (3 DOF). Further, we know the direction of the neutrino although not the energy (2 DOF), because we know the source where it is coming from. Finally, the scattering should be radially symmetric (1 DOF) as long as the target is unpolarized. This leaves three variables which must be measured to determine the kinematics.

In the laboratory , these variables are measured as (1) E_μ the energy of the outgoing muon, (2) θ_μ the angle of the outgoing muon, and (3) E_{HAD} the added energy of the outgoing hadrons. This is shown in Figure 1.1. However, these are all measured in the lab frame, of course, and are not Lorentz invariant. Thus, to study the kinematics in general we translate these into Lorentz invariant quantities.

The first kinematic quantity is Q^2, the negative square of the four-momentum transfer (q). In qualitative terms, this can be thought of as how hard the nucleus is being struck. Q^2 determines the energy level of the basic reaction. If we look at this in regions:

"Hard" Processes ($Q^2 >> M_p$)

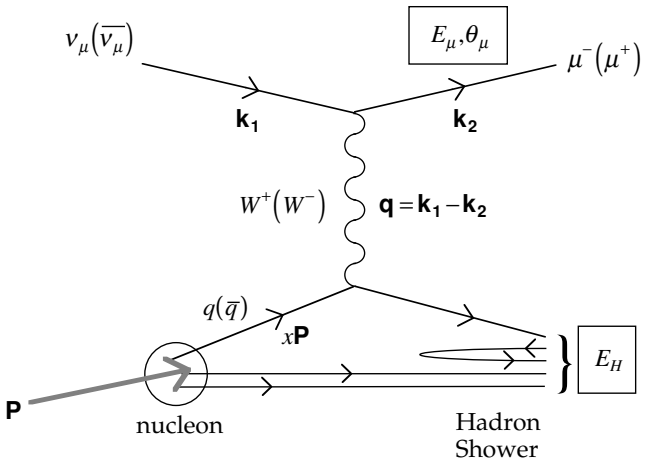

Figure 1.2: Neutrino-nucleon deep inelastic scattering from a theoretical perspective, with kinematic four-vectors noted in boldface ($\mathbf{k_1}$, $\mathbf{k_2}$, $\mathbf{q}$, $x\mathbf{P}$).

Here the scattering energy transfer is much larger than the proton binding energy. This means that terms for nuclear effects tend to drop out of the scattering equations.

"Soft" Processes ($Q^2 < M_p$)

Here the scattering energy transfer is on the same scale as nuclear effects. Thus, to calculate scattering technically requires a quantum calculation of the nucleus. These are known as "higher twist" effects.

The second kinematic quantity is known as x-Bjorken, or simply x, which varies from 0 to 1. This is calculated as ($Q^2/2M_pE_{HAD}$). x-Bjorken can be thought of as the length scale within the proton which is being probed – or more technically as the fractional momentum of the struck quark in the nucleon. Again we describe this in terms of regions:

Elastic ($x = 1$)

In these events the four-momentum transfer is the same as the energy transfer, and thus the proton remains whole scattered off with momentum E_{HAD}. Thus data with $x = 1$ sees the proton only as a solid object.

High-X $(0.3 < x < 1.0)$

In these events the proton is broken apart, and we can see the three primary quark constituents ("valence quarks"). The

Low-X $(x < 0.1)$

In these events, the cross-section becomes dominated by quantum fluctuations within the proton. On a smaller scale than the valence quarks, we see that the proton is filled with gluons and quark-antiquark pairs.

Besides Q^2 and Bjorken x, other kinematic variables include the invariant mass of the hadronic system, W^2, and the inelasticity, known as Bjorken y.

$$W^2 = (p')^2 = (p+q)^2 = M^2 + 2ME_{HAD} - Q^2 \tag{1.1}$$

$$y = \frac{p \cdot q}{p \cdot k} = \frac{E_{HAD}}{E_\nu} \tag{1.2}$$

The Quark Parton Model

Measuring the structure of the proton is complicated by the fact that the proton is constantly changing. At base, the proton consists of two up-quarks and one down-quark (known as the "valence quarks"). However, these quarks will exchange gluons, which interact with each other and further can split into quark/anti-quark pairs. These pairs are known as the "quark sea".

The Quark Parton Model is a predecessor of the Standard Model, which simply assumes that the quarks are spin-1/2 point particles. Then the chance of an incoming point particle scattering off of a parton should depend on only one component of the momentum: the one parallel to the momentum of the incoming particle. Thus, the structure of the proton can be represented by a set of probability distributions which tell us the chance of finding, say, an up-quark with a given x-momentum.

Now, quantum mechanics would tell us that this is technically incorrect. Since the quarks are interacting, we should need to know the full wave-function of the quarks to properly calculate scattering. Here we rely on the *impulse* approximation. In modern experiments, the scattering energy is usually much larger than the binding energy of the proton.

We can estimate the effect of this using the Heisenberg uncertainty relation, $(\Delta E \Delta t > \hbar)$. If the transfer of energy is large enough, the time of the scattering is very small. Thus, the scattering sees a collection of partons which are effectively "frozen" in time. They have positions and momentums which are determined by the wave-function, but they don't have enough time to interact during the scattering period.

A simple picture is to consider a collision with an object attached to a spring. If the collision is hard, quick knock, it can be calculated as just a two body problem, and then look at what the spring does in reaction. On the other hand, if the spring bends or contracts during the time of the collision, you must consider it as a part of the collision.

This is in effect the classical limit. The cross-section for scattering then may be written as the probability of finding a quark with given momentum fraction, times the cross-section with that quark.

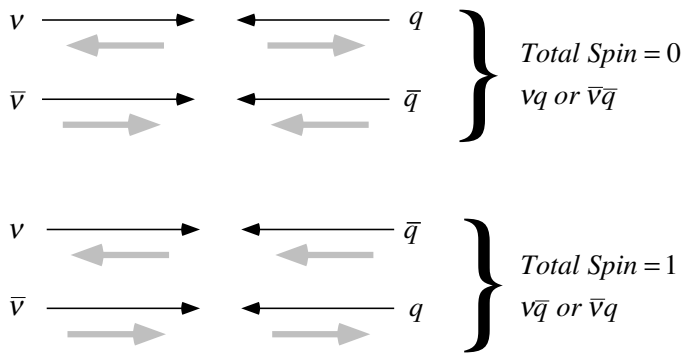

Figure 1.3: Possible helicity configurations for high-energy neutrinos and anti-neutrinos scattering from quarks and anti-quarks.

The cross-section for colliding with a quark is a simple elastic scatter of two point particles. It depends only one kinematic variable: Bjorken y, the angular momentum of the system (including helicity/spin). This is made simpler by the fact that neutrinos are always left-handed helicity and anti-neutrinos are always right-handed.

The kinematics of this scattering are shown in Figure 1.2. The neutrino is designated by four-momentum k, the quark by momentum p, and after scattering their four-momenta are designated by k' and p' respectively. This results in a four-momentum transfer, Q and an energy transfer we will call E_{HAD}. Note that in many formulas, the energy transfer is known as ν, but because of confusion with the neutrino symbol we designate it differently.

Thus, considering spin-1/2 and spin-0 constituents of the nucleon, the possible helicity-dependent cross-sections for elastic neutrino-quark scattering are given by:

$$\begin{aligned}
&\text{total spin } 0: && \frac{d\sigma^{\nu q}}{dy} = \frac{d\sigma^{\overline{\nu}\overline{q}}}{dy} = \frac{2G^2 M E_\nu}{\pi\left(1+Q^2/M_W^2\right)^2} \\
&\text{total spin } 1: && \frac{d\sigma^{\nu \overline{q}}}{dy} = \frac{d\sigma^{\overline{\nu} q}}{dy} = \frac{2G^2 M E_\nu}{\pi\left(1+Q^2/M_W^2\right)^2}(1-y)^2 \\
&\text{total spin } \tfrac{1}{2}: && \frac{d\sigma^{\nu g}}{dy} = \frac{d\sigma^{\overline{\nu} g}}{dy} = \frac{2G^2 M E_\nu}{\pi\left(1+Q^2/M_W^2\right)^2}\left(\tfrac{1}{2}-y\right)^2
\end{aligned} \tag{1.3}$$

Here q represent spin-1/2 quarks, $\overline{q}$ represent spin-1/2 anti-quarks of opposite helicity, and g represents the spin-0 gluons. Note that in the V-A structure of the weak interaction, the neutrino does not directly interact with the gluons – however, we include this for completeness. The transverse momentum of the quark can give rise to an effective spin-0 component of the cross-section.

Now according to the parton model, we can represent the cross section of the total proton as the sum of these cross-sections multiplied by a "parton distribution function" – i.e. the chance of

finding a quark with a given value of x. The quantity $q(x)dx$ is interpreted as the probability of finding a quark in a hadron carry a fraction x to $(x + dx)$ of the total proton's momentum. The quantity $\overline{q}(x)dx$ represents the same for anti-quarks. Thus, the combined cross-section is:

$$\frac{d^2\sigma^{\nu P}}{dxdy} = \frac{G^2 xs}{\pi \left(1 + Q^2/M_W^2\right)^2} \left[q^{\nu P}(x) + (1-y)^2\ \overline{q}^{\nu P}(x)\right] \tag{1.4}$$

Since a quark cannot exist in an isolated state, the struck quark undergoes a process known as "fragmentation", resulting in a shower of hadrons in the detector. For the purposes of this analysis, the details of fragmentation are ignored in favor of the total summed outgoing hadron energy: E_{HAD}. (Note that many deep inelastic scattering experiments refer to this as ν, but this is easily confused with the neutrino symbol and hence is not used here.)

General Structure Functions

The Parton Model outline above assumes the impulse approximation and a particular nature to the constituents of the proton. This is thus approximately true and forms an intuitive basis for interpreting our results. However, in a general treatment we cannot afford these assumptions. This section will outline the derivation of general "structure functions" which are independent of the model by which we are interpreting.

Let us consider the general case of a neutrino scattering off of a proton, without making these assumptions about the proton's constituents. Figure 1.1 shows a neutrino-nucleon charged current interaction and the measurable kinematic variables in our experimental detector. During the interaction, a neutrino with an incident energy E_ν exchanges a charged boson $W^{+(-)}$ with the proton. A muon emerges having energy E_μ. The emerging muon makes an angle θ_μ with respect to the incident neutrino beam axis direction in the laboratory frame.

Averaging over spin, the inclusive cross-section for this interaction is:

$$\frac{d^2\sigma^{\nu\ P}}{d\Omega_\mu dE_\mu} = \frac{1}{\left(1 + Q^2/M_W^2\right)^2} \frac{G_F^2}{2} \frac{m_\nu}{E_\nu} \frac{m_\mu}{E_\mu} \frac{E_\mu^2}{(2\pi)^2} L_{\alpha\beta} W^{\alpha\beta} \tag{1.5}$$

A generalized expansion of this differential cross-section can be divided into the helicity behaviors described before. Assuming only relativistic spin mechanics, it can be shown that the most general form of the differential cross-section is derivable from the V-A theory and is:

$$\frac{d^2\sigma}{dxdy} = \frac{G^2 ME}{\pi} \left[(1 - y - \frac{Mxy}{2E})F_2 + \frac{y^2}{2} 2xF_1 \pm (1 - \frac{y}{2})xF_3\right] \tag{1.6}$$

This equation defines the three *structure functions* (SFs) which depend only two variables: Bjorken x and momentum transfer Q^2. The three structure functions represent a mix of the three possible helicity configurations.

Note that if you compare this equation to equation 1.4 from the Quark Parton Model, you can associate the structure functions with the quark probabilities:

$$2xF_1^{\nu P} = 2\left[xq^{\nu P}(x) + x\overline{q}^{\nu P}(x)\right] \tag{1.7}$$

$$F_2^{\nu P} = 2\left[xq^{\nu P}(x) + x\overline{q}^{\nu P}(x)\right] \quad (1.8)$$

$$xF_3^{\nu P} = 2\left[xq^{\nu P}(x) - x\overline{q}^{\nu P}(x)\right] \quad (1.9)$$

$$(1.10)$$

where the (Q^2/M_W^2) and $(Mxy/2E)$ terms have been neglected. Note that to this first approximation in neutrino scattering, F_2 and $2xF_1$ are equal.

The GLS Sum Rule

The Gross-Llewellyn Smith Sum Rule concerns the integral $\int_0^1 xF_3\frac{dx}{x}$, where $xF_3(x,Q^2)$ is the non-singlet structure function measured in νN scattering. As shown above, within the simple Parton model xF_3 is the difference between quark and anti-quark momentum distributions. Since each anti-quark must be paired with a corresponding quark, in an integral over all momentums the pairs should cancel out. Thus, the GLS integral should equal the number of valence quarks in a nucleon: $\int_0^1 F_3 dx = 3$.

This thesis concerns how the actual GLS integral differs from this simplistic prediction. Quantum Chromodynamics (QCD) is a theory which allows a more complex prediction of what the GLS integral should be. Higher order QCD corrections to the GLS integral have been calculated which introduce a dependence on the strong coupling constant α_s, of the form:

$$\int_0^1 (xF_3)\frac{dx}{x} = 3\left[1 - F_{QCD}(\alpha_s, Q^2)\right] \quad (1.11)$$

By measuring the GLS integral, we extract a value of α_s at several values of Q^2. To compare with other experiments, we extrapolate to $\alpha_s(M_Z^2)$ using the known behavior of α_s with Q^2. Thus, this method uses a fundamental, well-understood prediction of QCD which is independent of the gluon distribution.

1.3 Quantum Chromodynamics

The underlying field theory for describing quark interactions is known as Quantum Chromodynamics or QCD. The exact details of QCD calculations are not relevant for this thesis, and could not be covered in any case. Instead, I will describe more qualitatively features of QCD which are relevant to understanding the significance of the result.

QCD is a field theory similar in many ways to the theory of electromagnetism, Quantum Electrodynamics or QED. Where QED has electric charge, QCD has "color charge". Where QED has exchange of photons, QCD has exchange of gluons.

As a field theory, QED and QCD calculations are represented by integration over a number of Feynman diagrams, where each diagram is a symbolic representation of terms in the calculation. The symbols and related terms for QCD are shown in Figure 1.4.

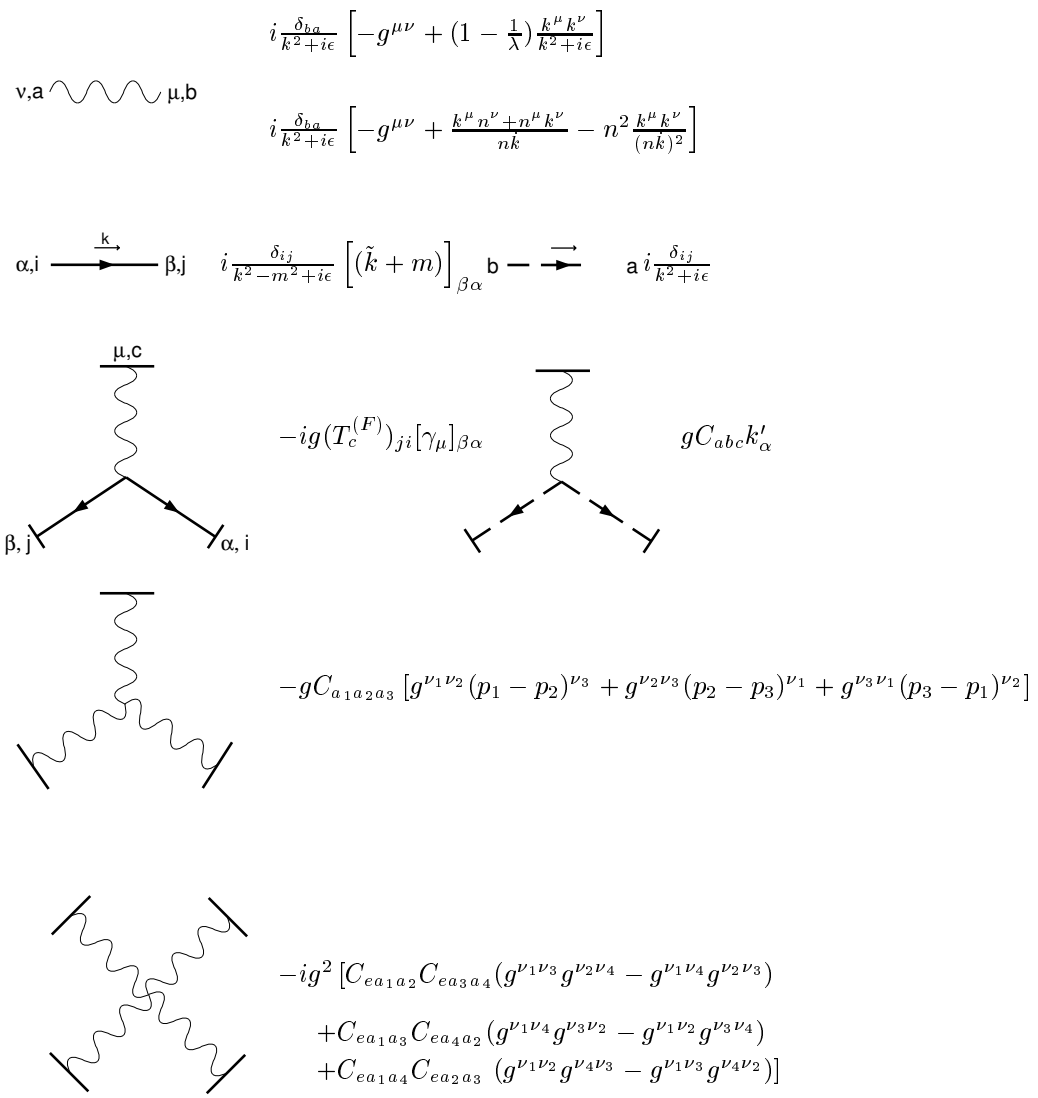

Figure 1.4: QCD field theory diagrams and their mathematical meaning.

Features of QCD

There are many features which are unique to QCD and bear discussion. Experimentally, we know that it conserves quark flavor as well as baryon number. Second, we expect it to prevent quarks from appearing singly, or in groupings other than three-quark baryons and quark-antiquark mesons – this property is known as "confinement." Finally, at high scattering energies it must give the same behavior as the parton model described in Section 1.2. In other words, for high energies (high Q^2) and hence short distance scales, the quarks must be weakly bound. This is known as "asymptotic

freedom."

QCD fulfills these predictions. However, in doing so QCD has a number of properties which make practical calculations more difficult.

Color: The charge in QCD is known as 'color', but whereas QED has only two charges (+ and -), QCD has three color charges (red, green, and blue) plus three anticolor charges (antired, etc.). Thus, a color-neutral bound state must have one of each charge, or a colored particle and same color anti-particle.

Asymptotic Freedom: The observations from early scattering experiments are in rough agreement with the Quark Parton Model described in Section 1.2. Since the QPM assumes non-interacting quarks, QCD must reproduce this by making quarks weakly interacting at these scales. The QPM is very successful for scales $Q^2 > 1\ GeV^2$, which correspond to short distance interactions.

Confinement: Conversely, no free quarks have ever been observed. Thus, the strong force must be extremely powerful at longer distances – or equivalently very low scattering energies. This is the revolutionary feature of QCD: accommodating both asymptotic freedom and confinement. Qualitatively, when two quarks are close together, the force is relatively weak (asymptotic freedom), but when they move farther apart the force becomes stronger (confinement).

Non-Abelian: In QCD, quarks can change their color while keeping all other properties the same. Since color is conserved, the color must be transfered by gluons. Thus, unlike QED where the photon is neutral, gluons themselves have color charge and can directly interact with other gluons. This property (called *non-Abelian*) makes the couplings different than in QED.

UV Divergence: Field theory calculations involve integration over a number of diagrams, where each diagram is a symbolic representation for terms in the calculation. These symbols and the related terms are shown in Figure 1.4.

However, cross-sections calculated according to the unmodified Feynman rules have a severe problem. To calculate real cross-sections, you must integrate diagrams over all of momentum space for a loop diagram. The problem is that the resulting cross-sections are infinite.

Renormalization: In order to make this a workable theory, these calculations are renormalized. Instead of integrating to infinite momentum, the loop integral is cut off at a scale known as μ. To begin with, μ is arbitrary and may differ from integral to integral. But to be physical, any observable σ cannot depend on our choice of μ. That is, the choice of μ must satisfy:

$$\mu \frac{d}{d\mu} \sigma(p, \mu) = 0 \tag{1.12}$$

To achieve this, it is necessary to specify a set of rules to determine the value of μ for each divergent diagram. Such a set of rules is called a *renormalization scheme* (RS).

Running Coupling Constant: To fulfill the condition of Equation 1.12, we must define our terms to eliminate dependence on μ. In un-renormalized field theory, the vertex has a constant g

which represents the strength of the force. To renormalize, we must make this "constant" a function of the scale μ (i.e. $g \rightarrow g(\mu)$).

Since any physical quantity cannot depend on the choice of μ, we define an amplitude $A(t)$ and expand it in a perturbation series. By Equation 1.12 this amplitude must satisfy:

$$\mu \frac{d\left[tA(t)\right]}{d\mu} = 0 \tag{1.13}$$

Expanding A in the perturbation series around $\alpha_s = 0$, this defines a condition for the general behavior of $\alpha_s(\mu)$. Conventionally, this condition is expressed using linear coupling $g(\mu) = \sqrt{4\pi\alpha_s(\mu^2)}$. The condition is then a power series in g beginning at order $O(g^3)$, known as a *beta function.*

$$\mu \frac{d\ g(\mu^2)}{d\mu} = -g\left(\frac{\alpha_s}{4\pi}\beta_1 + \frac{{\alpha_s}^2}{(4\pi)^2}\beta_2 + ...\right) \tag{1.14}$$

$$\mu \frac{d\alpha_s(\mu^2)}{d\mu} = -\frac{\beta_0}{2\pi}{\alpha_s}^2(\mu^2) - \frac{\beta_1}{8\pi^2}{\alpha_s}^3(\mu^2) - \frac{\beta_2}{4\pi^2}{\alpha_s}^4(\mu^2) + ... \tag{1.15}$$

We can solve this for α_s by defining a boundary condition $\alpha_s(\mu_0^2)$ and expanding the differential equation. To first order, this gives a solution of:

$$\alpha_s(\mu^2) = \frac{\alpha_s(\mu_0^2)}{1 + (\beta_0/4\pi)\alpha_s(\mu_0^2)\ln(\mu^2/\mu_0^2)} \tag{1.16}$$

The result is that α_s varies with scale, as shown in Figure 1.5. Note that the behavior of α_s provides for *confinement* by being very strong at low scales; while allowing for *asymptotic freedom* by becoming weak at very high scales.

The difficulty is that α_s is only known by a perturbative expansion. Thus, the renormalization condition (Eq 1.12) is only true if the series is calculated out to infinite order. In practice, QCD calculations are sufficiently difficult that most quantities are only calculated to a two or three orders. Thus, practical QCD predictions depend on the renormalization scheme (RS) that is chosen.

Quark Masses: The wide range of quark masses make them difficult to incorporate into most QCD calculations. The invariant quark masses cannot be measured directly, but they have been estimated. The u, d, and s quarks are light ($m_q < 0.3\ GeV$); while the c, b, and t quarks range in mass from $\sim 1.3\ GeV$ to $\sim 180\ GeV$ respectively.

Adding explicit quark masses tends to destroy the convergence of mass-independent QCD expansions for $m_q^2 >> Q^2$. Mass-dependent schemes are technically possible, but in practice are extremely difficult. The general solution is to continue to neglect quark masses, and take the number of quark flavors (n_f) to depend on the momentum scale (i.e. $n_f \rightarrow n_f(Q^2)$). At low momentum scales, only the light quarks will be accessible and thus $n_f = 3$. At higher momentum scales, we switch to $n_f = 4$ and $n_f = 5$ as warranted.

Thus, in practical QCD calculations, it is inherent that the result will depend on the renormalization scheme as well as the number of quark flavors (n_f).

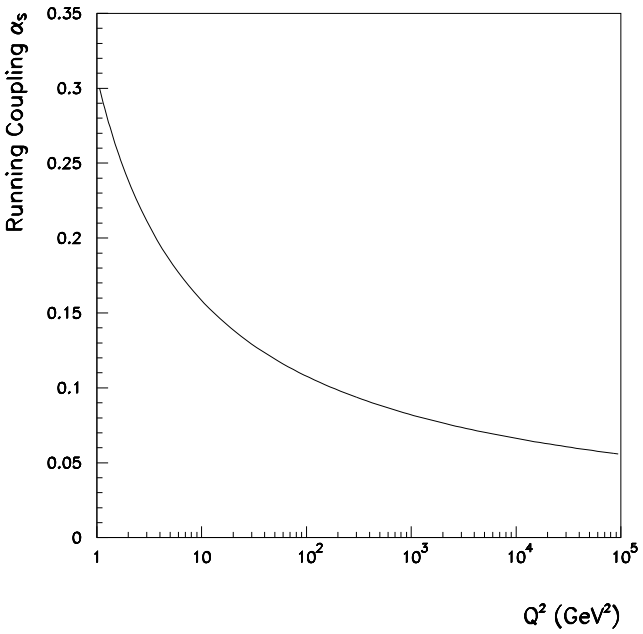

Figure 1.5: The running coupling constant α_s as a function of Q^2.

Perturbative QCD Corrections

For deep inelastic scattering, perturbative QCD allows us to calculate certain quantities. The leading order of this perturbative calculation corresponds to the naive Quark Parton Model described in Section 1.2. The quarks are described by "parton distribution functions" (or PDFs), and are considered non-interacting to leading order. Additional terms (in increasing powers of α_s) then add quark-gluon interactions to this picture.

The key to this approach is the theorem of *factorization* of long-distance from short-distance dependence for deep inelastic scattering. This theorem states that the sum of all the diagrammatic contributions to the structure functions is a direct generalization of the parton model results , given by:

$$F_a^{(Vh)}(x,Q^2) = \sum_{i=f,\bar{f},G} \int_0^1 \frac{d\xi}{\xi} C_a^{Vi}(x/\xi, Q^2/\mu^2, \mu_f^2/\mu^2, \alpha_s(\mu^2)) \quad (1.17)$$

$$F_2^{(Vh)}(x,Q^2) = \sum_{i=f,\bar{f},G} \int_0^1 d\xi C_2^{Vi}(x/\xi, Q^2/\mu^2, \mu_f^2/\mu^2, \alpha_s(\mu^2)) \times \phi_{i/h}(\xi, \mu_f, \mu^2) \quad (1.18)$$

Here μ_f is called the factorization scale, which serves to define the separation of short-distance from long-distance effects. Roughly speaking, any propagator that is off-shell by μ_f^2 or more will

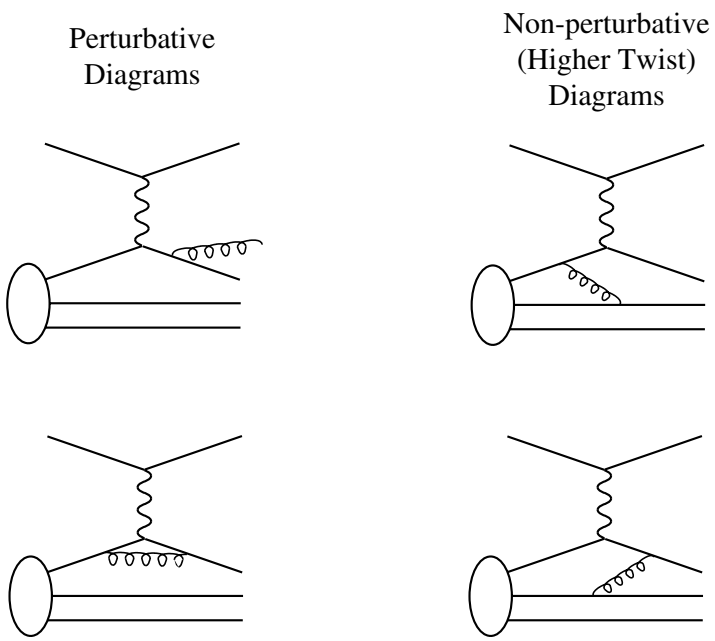

Figure 1.6: Sketch illustrating perturbative versus non-perturbative effects.

contribute to $C_a^{(Vi)}$. Below this scale, it will be grouped into $\phi_{i/h}$. The factorization scale μ_f is often chosen to be the same as the renormalization scale μ, but this is not strictly necessarily.

Non-perturbative QCD Corrections

By definition, perturbative QCD only considers operators which do not involve more than one target quark. More explicitly, perturbative operators must have a vacuum expectation of zero. This is known as the free field condition. However, this approach neglects many operators which will have non-zero vacuum expectation values, representing interactions with other quarks in the proton.

Within perturbative QCD, one can classify operators according to their "twist" τ, where $\tau = \rho - j$ with ρ the (free field) dimension and j the spin of the operator. The leading operators are those of twist-2. Operators of twist $\tau = 2n + 2$ are suppressed by a factor of $(M^2/Q^2)^n$ with respect to the former.

The leading, twist-2 operators have no dependence on inter-quark interactions. Thus, these operators will represent only the struck quark and quark loops (as shown in Figure 1.6). Operators of $\tau > 2$ are known as "higher twist" and include interactions with other quarks. Within QCD, higher twist contributions must be calculated using phenomenological approximations to define the quark confinement and hence the proton wave function.

QCD Prediction of GLS

Perturbative QCD predicts the value of the GLS integral as a function of α_s, Q^2, and the number of accessible quark flavors, n_f. This predictions has been calculated out to the next-to-next-to- leading order (NNLO) in perturbative QCD. In addition, non-perturbative QCD calculations predict a higher-twist correction term. In its final form, the NNLO perturbative QCD and non-perturbative QCD calculations result in a prediction of:

$$GLS(n_f) = 3(1 - \tfrac{\alpha_s}{\pi} - a(n_f)(\tfrac{\alpha_s}{\pi})^2 - b(n_f)(\tfrac{\alpha_s}{\pi})^3) - \frac{\Delta HT}{Q^2} \quad (1.19)$$

$$a(n_f) = 55/12 - n_f/3 \quad (1.20)$$

$$b(n_f) = 41.441 - 8.02 n_f + 0.177 n_f^2 \quad (1.21)$$

$$\Delta HT = 0.15 \pm .15 \; GeV^2 \quad (1.22)$$

This is using the $\overline{MS}$ renormalization scheme, although the values for other renormalization schemes have also been calculated. Because of the high order to which this has been calculated, the differences between renormalization schemes are minimal.

The goal of this thesis is to maximize the theoretical accuracy of this prediction. This involves evaluating $\int F_3 dx$ without using any QCD-based fits or extrapolations in Q^2. While the measurement of α_s assumes a QCD prediction, use of lower-order QCD functions in the analysis would invalidate the high-order accuracy of this prediction.

An earlier measurement of the GLS integral was published by the CCFR collaboration[Leu93]. That analysis used a leading-order (LO) QCD-based fit to extrapolate all data to $Q^2 = 3 \; GeV^2$, fitted the extrapolated data to a single function over all x, and numerically integrated that function. The resulting integral was compared against the LO GLS prediction. A similar result was obtained by a NLO global fit analysis of the same data [Kat94]. However, these approaches cannot make full use of the accuracy of the NNLO calculation shown above, since they depend on lower order pQCD for extrapolation. Also, the previous CCFR analysis did not correct for quark mass thresholds, target mass or higher-twist effects. These corrections are important at the effective mean Q^2 of the result ($Q^2 \sim 3 \; GeV^2$).

The current GLS analysis evaluates $\int F_3 dx$ without any QCD-based extrapolations by combining the CCFR xF_3 data and data from earlier neutrino experiments. Using the other data, we can expand the CCFR kinematic region to measure $\int F_3 dx$ for $1 < Q^2 < 20 \; GeV^2$ without Q^2 extrapolation.

Chapter 2

Neutrino Beamline

As mentioned in the introduction, neutrinos have an extremely small cross-section. On average, a 100 GeV neutrino will pass through 200 thousand miles of steel before it reacts. Further, its chance of reacting is linear with energy: i.e. a 10 GeV neutrino will pass through an average of 2 million miles of steel. Thus, the priority of our neutrino beamline was simply to produce as many neutrinos as possible – at as high an energy as possible.

The high energy was provided by the Fermilab Tevatron accelerator, currently the highest energy accelerator in the world. By using superconducting electromagnets, it is able to contain and accelerate protons up to 900 GeV. The Fermilab Tevatron accelerator and neutrino beamline is show in Figure 2.1.

The figure shows high-energy protons generated in the main ring, which were extracted into a switchyard which guides via magnets to different fixed-target experiments. The protons used for neutrino generation were guided from the switchyard using a series of dipole and quadrupole magnets onto a 30.5 cm thick beryllium oxide target. The secondary particles (notably pions and kaons) from collision then continued towards the neutrino detector, focused by the quad magnet train and decaying within the 320 m decay pipe into muons and neutrinos. The muons and surviving other particles were blocked by the ~ 915 m of shielding after the decay pipe.

2.1 Beam Extraction

During the E744 and E770 runs, the 800 GeV protons in the Tevatron were generated and released on a 60 second cycle. The protons used for neutrino generation were concentrated into three packets, which were released in fast-spill "pings" of duration ~ 1 $msec$. This procedure greatly reduced the cosmic ray background, since the detector was only active for order ~ 3 $msec$ out of every minute.

The full 60 second cycle is shown in Figure 2.2. Starting at time T1, the Tevatron was filled with approximately 2×10^{13} protons from the Main Ring. At time T2 (~ 10 sec), the protons were accelerated and the Tevatron magnet currents are ramped up accordingly. After 10 seconds

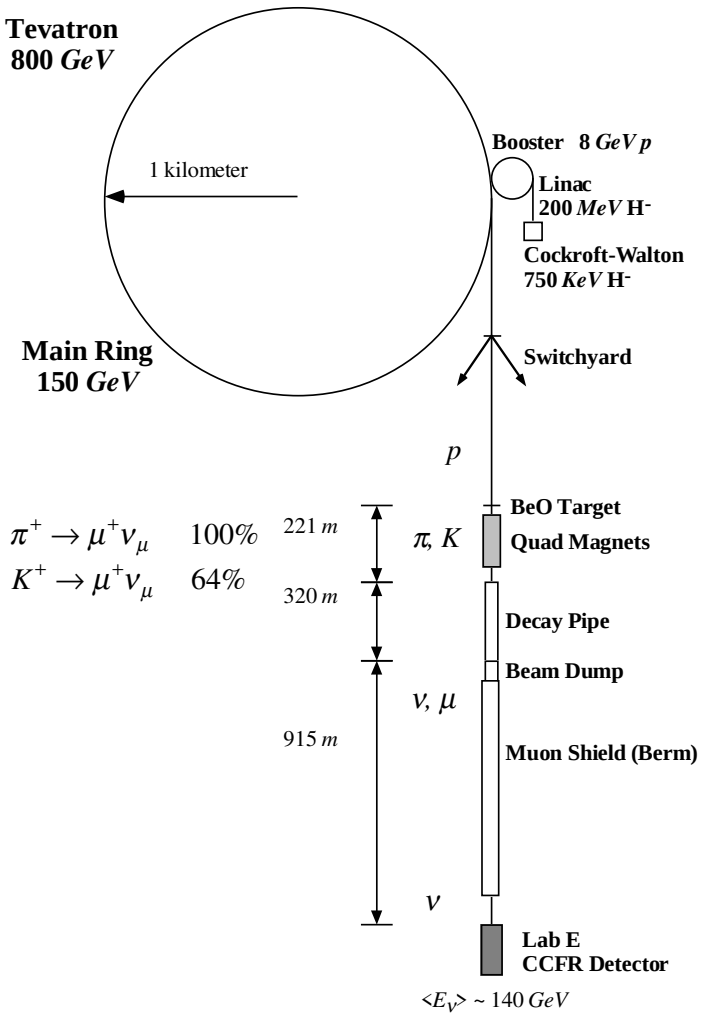

Figure 2.1: Fermilab neutrino beamline layout.

of acceleration (time T5), the protons reached 800 GeV. Over the next 23 seconds, protons were extracted in two slow spills (each 2 seconds) and three fast spills (~ 1 $msec$ "pings"). After this (at time T6), the magnets begin to ramp down and the cycle repeats.

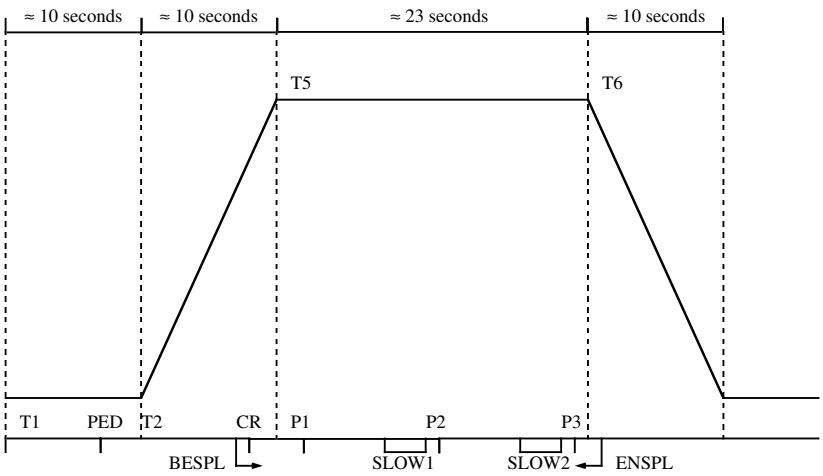

0 x 300

Figure 2.2: Tevatron magnet current versus time during fixed-target operation. P1, P2, and P3 indicate the fast-spill "pings" described in the text.

2.2 Secondary Beam and Magnet Train

After striking the BeO target, the emerging hadrons consisted primarily of surviving protons and mesons such as charged hadrons and kaons. Over the next 221 meters, these were focused by the so-called "quad-triplet" magnet train (which actually contained 7 quadrupole magnets), shown in Figure 2.3. By not selecting a particular momentum or sign of particle, this design focuses a wide range of secondary particles towards the detector. The beamline was tuned to optimally focus 300 GeV secondaries of either sign, and is known as a "wide-band" beamline because it selects a wide range of momenta around this value. The quadrupole magnets focus in one transverse direction and defocus in the orthogonal direction – which depends on the charge of the particle. A train such as this one, with two or more quadrupole magnets of alternating focusing directions can simultaneously provide focusing for both charge signs.

The quad-triplet beamline replaced the earlier "sign-selected narrow-band beamline" used in Fermilab experiments E616 and E701 (also by the CCFR collaboration). There, dipole bending magnets and collimation were used to select a narrow momentum range of either positive or negative secondaries.

The new experiment, NuTeV, features a "sign-selected quadrupole triplet" beamline which selects sign by dipole bending, but accepts a wide range of momentums by quadrupole re-focusing.

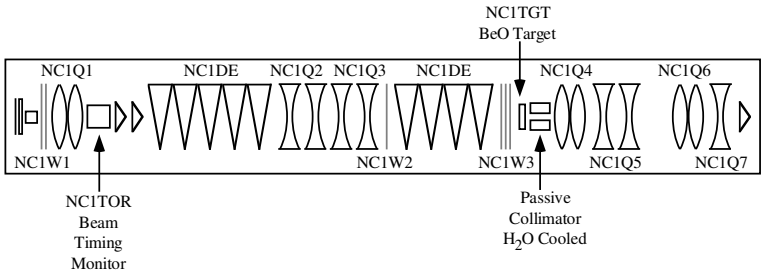

Figure 2.3: Quad triplet magnet train. Dipole magnets are indicated by prisms (triangles), and quadrupole magnets are indicated by concave and convex lenses.

2.3 Decay region

After the quad triplet train, the secondaries enter a 320 m decay region. There, pions and kaons decay in flight, with dominant decay modes:

$\pi^+ \to \mu^+ \nu_\mu$ BR=99.99%
$K^+ \to \mu^+ \nu_\mu$ BR=63.5%

Anti-neutrinos ($\overline{\nu_\mu}$) are produced from π^- and K^- by the charge-conjugated processes. The maximum neutrino energy is governed by the mass ratio of the muon and the decaying particle. Thus, the neutrino beam exhibits a dichromatic spectrum:

$$E_\nu^{max} = E_{\pi,K}\left[1 - \left(\frac{m_\mu}{m_{\pi,K}}\right)^2\right] \quad (2.1)$$

$$\left(E_\nu^{max}\right)_K = 0.95 E_K \quad (2.2)$$

$$\left(E_\nu^{max}\right)_\pi = 0.43 E_\pi \quad (2.3)$$

Approximately 10% of the mesons decay in the decay region, and the remainder is dumped into a 6m block of aluminum. The CCFR detector is positioned 915 m beyond the dump. The muons and neutrinos that penetrate the aluminum beam dump encounter approximately 241 m of steel shielding and 582 m of earth "berm" before reaching the detector. The amount of material is sufficient for the muons from meson decays to range out, so that of all the particles entering the berm, only the neutrinos penetrate into the experimental areas.

However, some neutrinos interact inside the earth berm, and thus some muons produced by charged-current neutrino interactions just upstream of Lab E enter the detector. These events are identified and vetoed by a wall of scintillation counters on the upstream end of the detector (the "veto wall").

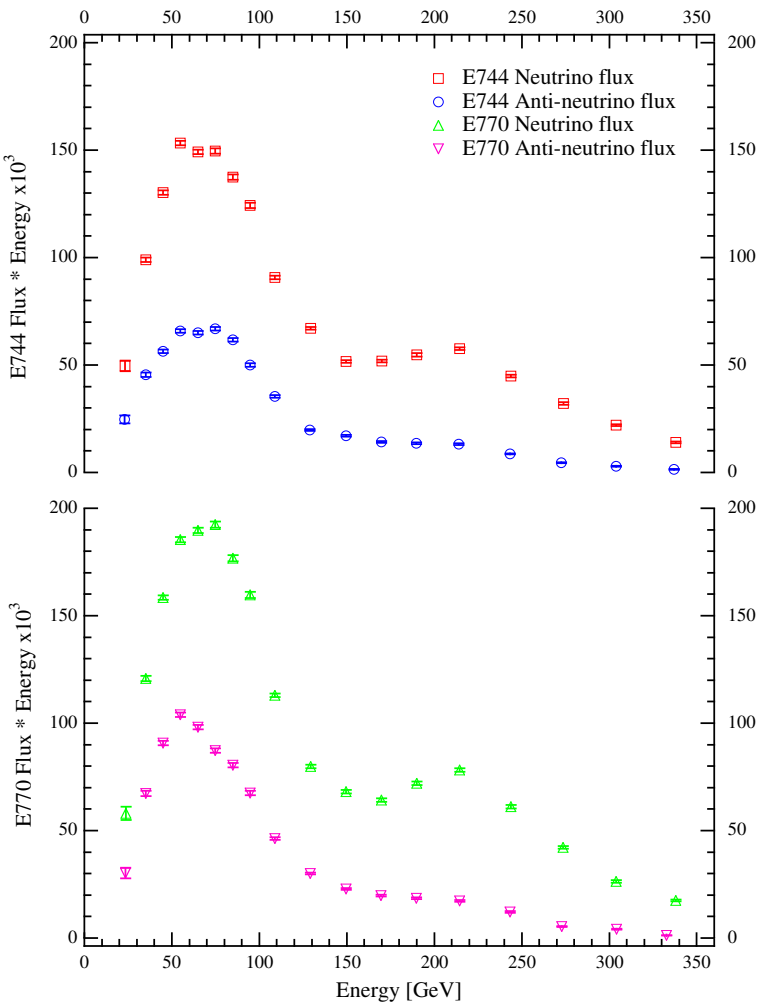

Figure 2.4: The fully corrected flux × energy spectra for E744 and E770. The normalization along the left axes is arbitrary.

2.4 Neutrino Spectrum

Figure 2.4 shows the estimated spectrum of neutrino flux incident on the Lab E detector within a 30" radius of the centerline. The procedure for extracting the flux is explained in Section 2.3. Approximately 86.4% of the E770 final event sample came from ν_μ interactions, 11.3% from $\overline{\nu_\mu}$, and 2.3% from ν_e or $\overline{\nu_e}$. Antineutrino-induced events were suppressed relative to neutrinos by lower secondary production rates and a factor of two suppression in the total cross-section.

Charged pions and kaons accounted for more than 99.8% of the ν_μ's in the final event sample.

80% of the production of ν_es came from the Ke3 decay mode of charged kaons, and 16% from neutral kaons, with the remaining 4% from various charmed mesons, pions, muons, deltas, and sigmas.

$K^+ \to \pi^0 + e^+ + \nu_e$ BR=4.8%
$K^0 \to \pi^- + e^+ + \nu_e$

The front face of the CCFR detector is 915 m from the end of the decay region, and neutrinos strike the detector within about one meter radius of the beam axis. Therefore, the neutrinos have an incident angle no larger than about 1 $mrad$.

Chapter 3

The CCFR Detector

The CCFR neutrino detector design had many requirements. First, it must be be very massive, in order to maximize the number of interactions. Second, it must be able to sample hadronic particle showers in order to measure the energy of the hadronic system. Third, it must have charged particle tracking and part of it must be magnetized in order to measure muons which result from charged-current interactions.

The detector must measure the following basic quantities:

- E_{HAD} : the hadronic energy deposited in the calorimeter, measured by sampling the hadronic shower with scintillators.
- V_x, V_y, V_z : the vertex position of the interaction, measured by particle tracking within the target calorimeter.
- θ_μ : the angle between the emerging muon and the detector Z-axis, measured by particle tracking within the target calorimeter.
- E_μ : the energy of the emerging muon, derived from muon bend angle within the magnetic spectrometer as determined by particle tracking.

The actual CCFR detector (shown in Figure 3.1) consists of a 690 ton iron target calorimeter and a 420 ton toroidal magnet muon spectrometer. The calorimeter has 84 scintillation counters to sample energy loss, spaced every 4 inches of iron – as well as 42 drift chambers to measure particle position. The spectrometer consists of three toroidal magnets, each with eight 8-inch washers with 5 drift chambers placed after each magnet.

3.1 Scintillation Counters

The target calorimeter has 84 liquid scintillation counters evenly spaced along its length. Thus, for roughly every 4" of iron passed through, particles pass through 1" of liquid scintillator – a more

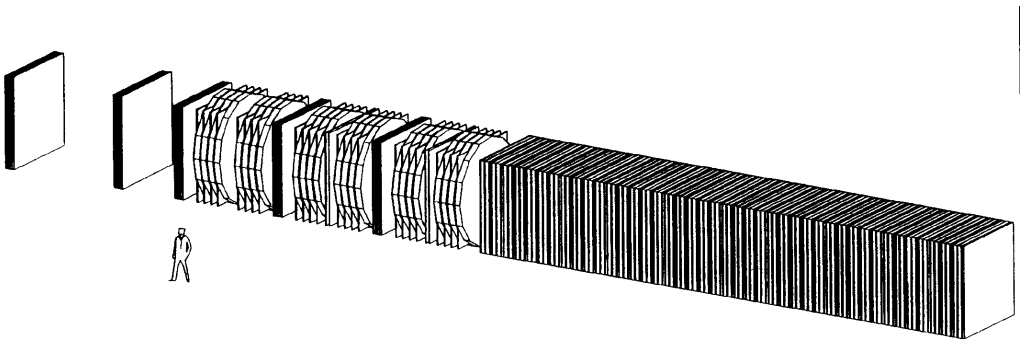

Figure 3.1: Overhead view of the CCFR detector.

exact breakdown of the matter in Appendix C. Taking into account density, this means that for each counter, a minimum ionizing particle (or "MIP") loses 0.2 GeV in the iron and .006 GeV in the scintillator (an energy sampling fraction of 3%). See Chapter 4 for more details.

The counters themselves are hollow lucite containers filled with a solution of mineral oil and active scintillating fluors. The primary fluors emit ultraviolet light in response to the passage of charged particles. This UV light is absorbed by secondary fluors in the oil, which emits visible blue light. The blue light has a longer attenuation length in the oil (about 50 cm), and thus is dominant. The light is absorbed along the edges of the counters by $\frac{1}{2}$" thick BBQ doped plastic "waveshifter" bars which absorb the blue light and re-emit green light. The green light is collected at the four corners of the counters by phototubes which were held against the ends of the waveshifter bars.

Details of the counter structure can be found in Appendix C.

The tubes were RCA 6342A phototubes, operated at approximately 1400 volts. Each incident photon on the cathode has about a 20% chance of liberating an electron. The tube multiplies this signal with a series of 10 dynodes, each of which emit 4 electrons per 1 absorbed – thus a single initial photoelectron produces a signal of about 0.25 picoCoulombs. Overall, the sensitivity to a muon passing through the center of the counters is about 2.5 photoelectrons per phototube.

3.2 Phototubes and Readout

The phototube signal is digitized by a LeCroy 4300 FERA, a fast and buffered readout system with analog-to-digital (ADC) converters with 11 bits of dynamic range. The counter readout has sever ADC channels of differing sensitivity and the phototube signal is fanned out, giving the system an effective dynamic range of 19 bits. One counter's readout is show in Figure 3.4. The gate width of the ADC's is 240 $nsec$, beginning 25 $nsec$ before the leading edge of the phototube signal, for an integration time of 215 $nsec$. The charged collected is stored on a capacitor and the digitization is

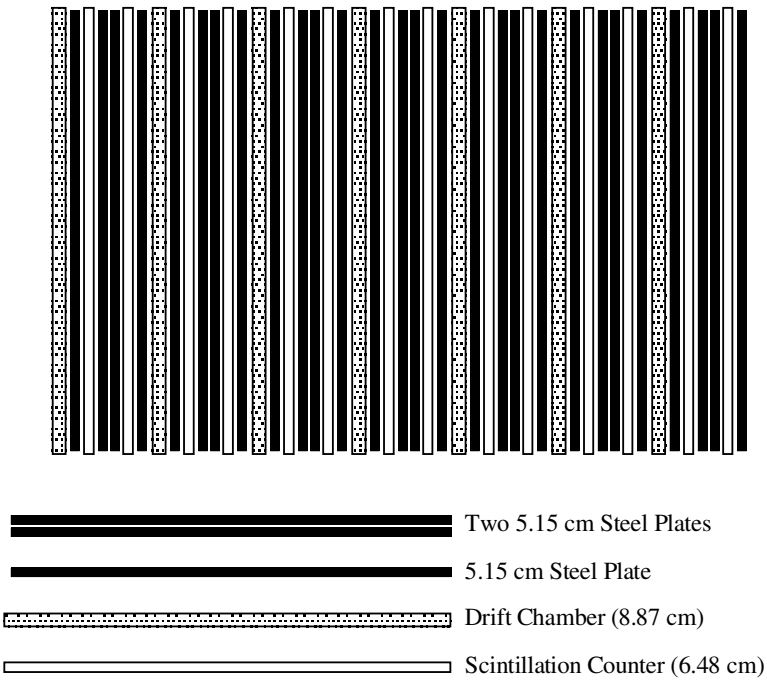

Figure 3.2: Side view of a CCFR target unit. A single unit consists of two scintillation counters, each sandwiched by two steel plates, followed by a single drift chamber.

accomplished by measuring the time required to discharge the capacitor through a resistor. Digitizing the signal required 8.5 μsec and another 3.2 μsec is needed to buffer the data, leading to a dead time of 11.7 μsec. A pedestal voltage of approximately 50 counts is applied to each ADC. This pedestal is recorded every accelerator cycle, before the first ping, by taking 20 fake events, so that it can be subtracted from the data readings.

The analog phototube outputs from each counter are fanned out and digitized by seven ADC channels of differing sensitivity, to maximize the dynamic range:

Lows(4): (A_j^{LO}) are four channels, one for each of the phototubes in a counter. A muon passing through the center of a counter will typically produce 2 ADC counts at each low channel. This is used for measurement of the hadron shower.

Combination-Low: (A^{COMBLO}) is the analog sum of the four low signals. A muon yields 8 ADC counts at this channel. This is used to produce a logical signal known as a scintillator-bit or s-bit, when the COMBLO signal is over 1/4 of minimum ionizing level.

Super-low: This channel $A^{SUPERLO}$ is a sum of lows from phototube j from every tenth consecutive counter, attenuated by a factor of ten. The typical muon signal at this channel is only 0.2

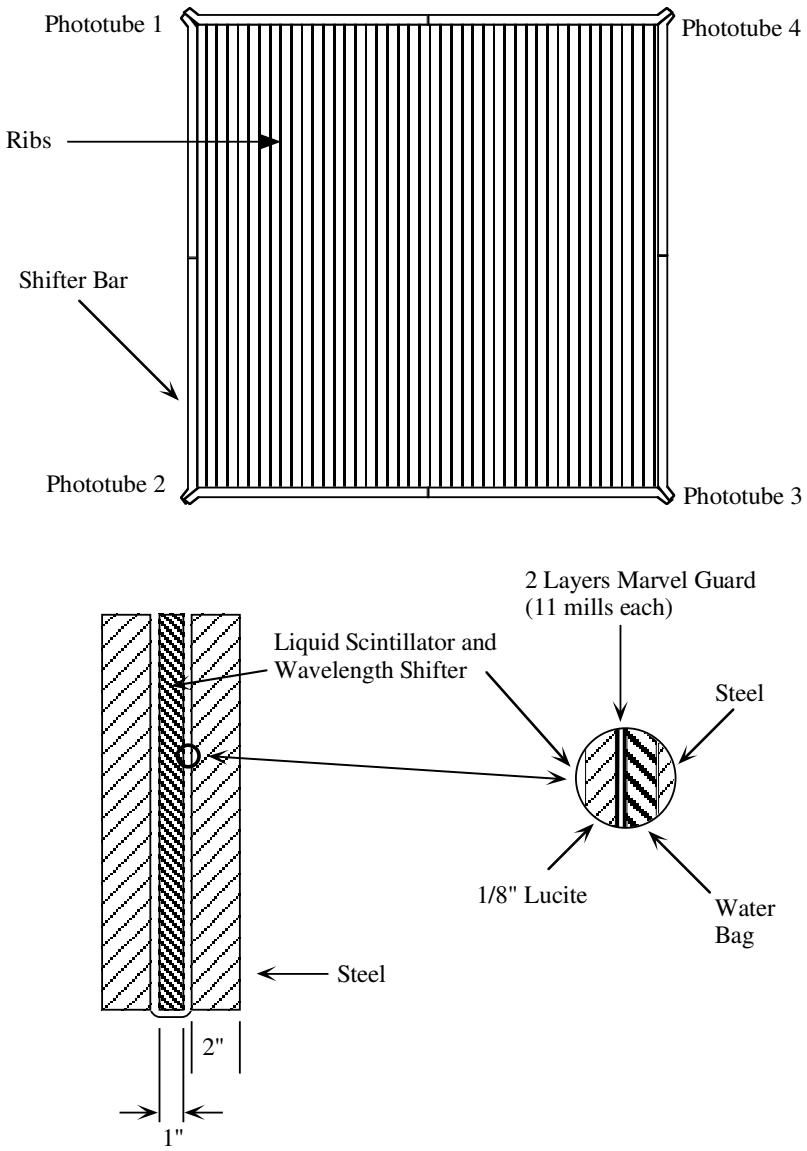

Figure 3.3: Front and side views of a CCFR scintillation counter.

counts. This channel is used to measure the hadron shower in the event of an overflow in the lows – caused by greater than $(2^{11} - 1) = 2047$ counts. A typical hadron shower will produce 1000 to 2000 counts in one counter.

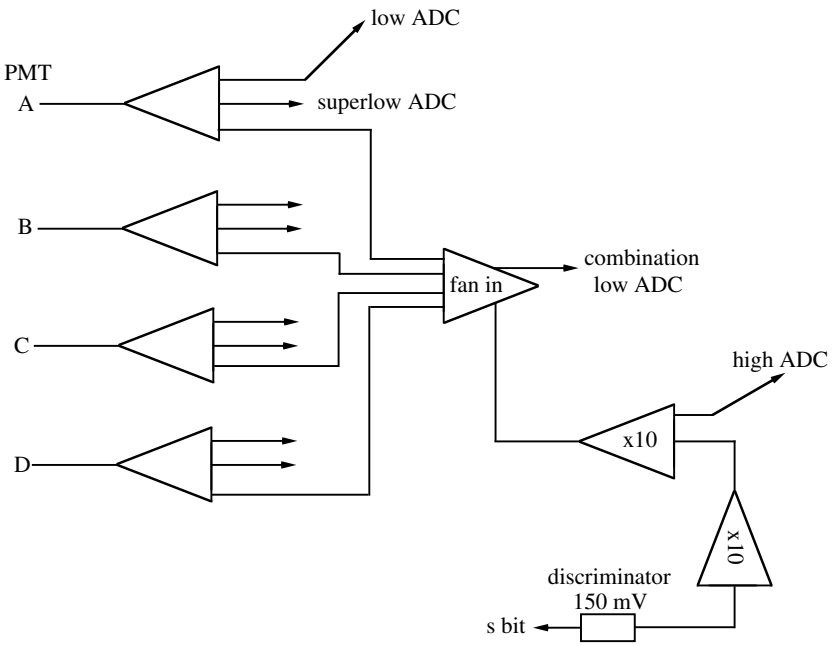

Figure 3.4: Readout electronics for a single scintillation counter. Each counter's signal is digitized into the seven ADC channels described in the text. The threshold of the s-bit discriminator is set at one-quarter of a single minimum ionizing particle (MIP).

High: (A^{HI}) is the sum of the four low signals amplified by a factor of ten. The muon signal at this channel is 80 counts. This is used to measure the passage of a muon.

At the Tevatron, the accelerator rf buckets arrive in intervals of 18.8 *nsec*. Event timing is measured at each counter using the same time-to-digital converters (TDCs) that are used for the drift chambers (see below). Each counter's s-bit pulse is fed to the TDC, providing a time resolution of 4 *nsec*. When information from all active counters is combined, the overall event time resolution has an RMS of 2.4 *nsec*.

3.3 Drift Chambers

The detector has 42 three-wire Drift Chambers along its calorimeter, plus single-wire Drift Chambers within and behind the toroidal magnet spectrometer. These measure the transverse position of charged particles, allowing us to closely reconstruct the path of the muon and roughly estimate the direction of the hadron shower.

Each device consists of two planes (X and Y): each is divided into 24 parallel chamber cells filled with a gas mixture of argon and ethane. (See Figure 3.5). When a charged particle passes through a chamber cell, it ionizes electrons from the gas mixture, which drift in an electric field towards

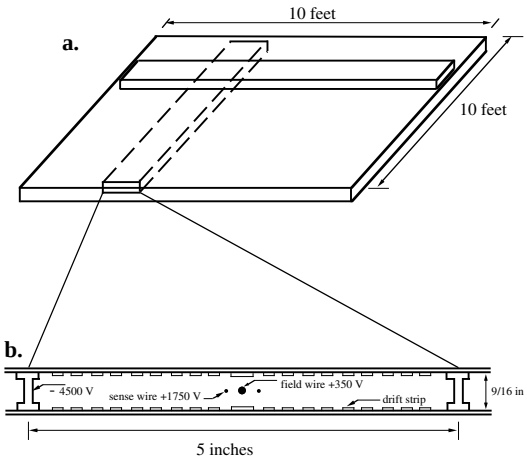

Figure 3.5: Sketch of a CCFR target drift chamber. **a.** shows one chamber, consisting of two planes each with 24 three-wire cells. **b.** shows the cross-section of a single three-wire cell.

the wires at the center. When the electrons hit, their charge is registered on the sense wire. By measuring the drift time of the electrons compared to the known time of the event, the perpendicular distance of the charged particle from the axis of the sense wire is determined.

The electric field is provided by applying a high voltage differential between the wires at the center of the cell and the strips along the walls of the cell.

Each chamber is constructed of Hexcel covered aluminum walls. Parallel aluminum I-beams spaced every 5 inches support G10 cover plates and define the drift chamber cells. Within each cell, a 127 μm diameter coper-beryllium central field wire is held at +350 volts. Two 30 μm diameter gold-plated tungsten wires run on either side of the field wire and are held at +1750 volts. Nylon spacers placed every 12 inches maintain 2 mm spacing between each sense wire and the field wire. The I-beams are maintained at -4500 volts. Finally, the inside of the G10 cover within each cell is clad with 19 copper cathode strips, each of which is held at a particular voltage so that a uniform electric field of 690 V/cm is created.

The chambers are filled with an equal mix of argon and ethane. A noble gas, argon lacks vibrational or rotational modes of excitation. Therefore, argon readily ionizes when excited by a passing energetic charged particle. After the primary ionization, the electrons and ions separate due to the applied electric field. The electrons drift towards the anode sense wires and accelerate, producing secondary ionizations. Ethane, an organic compound, is included to render the chamber self-quenching. That is, the ethane absorbs the ultraviolet photons liberated in the argon as the electrons drift toward the sense wires. This prevents the avalanche of charge that would otherwise smear the signal pulse.

The drift velocity of electrons in the drift chambers is 50 $\mu m/nsec$, so that the total drift time to

cross 2.5" inside a cell is 1.3 μsec. The arrival time of the drift chamber pulse on one wire relative to the event time allows the determination of the particle's position in one dimension, up to the ambiguity of knowing on which side of the wire the particle passed. Having two sense wires per cell resolves this ambiguity, as the wire closer to the particle receives the ionization first. Combining the hit information from two adjacent orthogonal cells provides the determination of the particle's position in the x-y plane.

The signal from the sense wires is amplified and sent to two coupled TDCs, which have their 8 $nsec$ time bins staggered by 4 $nsec$. Thus the coupled TDC digitizes the time of the pulse in 4 $nsec$ bins. The TDC is capable of buffering hits in 512 bins, so its live time is slightly in excess of 2 μsec and so can buffer the full drift range of the cell. The TDC then takes 8 μsec to transfer its information into a first-in, first-out memory. The FIFO memory can store 32 events per spill.

The overall position resolution of the drift chambers is 225 μm. This depends on the time resolution of the TDCs, variations in the electric field and misalignment of the chambers. All elements of the detector were aligned with an optical survey, and precise alignment of the chambers was accomplished by using high energy straight-through muons ($p_\mu > 125\ GeV/c$). The alignment procedure iteratively varied the chamber coordinates to provide the best fit to the sample of straight-through muons. In the target, the alignment procedure was straightforward: there was no magnetic bending, and multiple Coulomb scattering is small at high energy (see Section 5.4).

3.4 Toroid Spectrometer

The "front face" of the spectrometer is $\sim 30\ in$ downstream of the last target counter (Counter #1). It consists of three large instrumented toroidal magnets (referred to as a toroid cart), plus instrumentation in the gaps and in a downstream structure called the "blue cart". Each toroid cart is segmented into eight 8-inch thick toroidal "washers" with 70-inch outer radius and a 5-inch inner radius. Each washer is divided horizontally into semicircles separated by 0.95 cm with aluminum spacers to allow the insertion of a Hall probe. The bottom of each washer includes two iron legs that support the magnets on movable platforms.

Four copper coils of 12 turns each encircle the magnets at 90^o intervals. A current of 1500 A produces a magnetic field ranging from 1.9 T near the center of the toroid to 1.55 T near the outer edge. The field was found to be azimuthal throughout the magnets except for a small radial component at the iron legs. A muon traveling the length of the spectrometer receives an additional 2.4 GeV/c transverse momentum component.

Tracking muons through the spectrometer is accomplished by five sets of 5 drift chambers: one set downstream of each toroid, and two in the blue cart (3 m and 7 m downstream of the last toroid). These are single-wire-per-cell drift chambers, staggered by 1/4 of a cell width to resolve the left-right ambiguity. The five chambers are set directly against each other, for multiple redundancy.

3.5 Triggering

The data acquisition was activated by triggers, which used only the quickly-processed scintillation signals.

The backgrounds which we would seek to exclude are cosmic rays and particles emanating from neutrino interactions in the upstream berm. The cosmic ray events were greatly reduced by restricting our timing to the brief periods of neutrino production. Particles from the berm were excluded by the "Veto Wall" – two $17.5x4.5\ m$ arrays of scintillation counters positioned immediately upstream of the first calorimeter cart. The veto wall counters were shielded from low energy particles by a 1m thick concrete wall, and lead sheets were mounted between the two scintillators of the veto wall.

Also, secondary particles produced in the berm will interact with the air above the detector and illuminate the detector with low energy tertiaries (known as "skyshine"). A layer of lead bricks is stacked above the toroid gaps to shield the trigger counters from this.

The triggers used only the target scintillation counters and the scintillators located in the toroid gaps. Six separate triggers were used during the run:

- **Trigger 1** ("Charged Current") was designed to select charged-current interactions in which a muon originates in the target and penetrates into the toroid for momentum-analysis. The logic requires the presence of a charged particle in the most downstream target cart (#1) and in the toroid, with no activity in the veto wall.

  Either of two topologies must be satisfied: Either **(A)** at least 2 out of counters #1-4 must fire their s-bits, and a minimum ionizing signal is recorded in both T2 and T3; or **(B)** at least 2 out of counters #9-12 *and* at least 2 out of counters #1-4 must fire their s-bits, and a minimum ionizing signal is recorded in T2. See Figure ??.

  This is the trigger which was used for all the structure function analysis.

- **Trigger 2** ("Neutral Current") was designed to select neutral current events as well as charged current events. It requires that at least $8\ GeV$'s are deposited in 8 adjacent counters, coincident with two times minimum ionizing energy deposited in 2 counters out of a set of 4 consecutive counters, and no veto. No muon requirement is made.

- **Trigger 3** ("Penetrating Muon") was designed to study muons ranging out in the calorimeter. It requires that 16 counters in the target (not necessarily consecutive) fire their s-bits with no veto, along with 4 GeV of hadronic energy deposited in a set of 8 consecutive counters (but not necessarily those that fired their s-bits).

- **Trigger 4** ("Redundant Charged Current") was designed to measure the trigger 1 inefficiency. It is similar to trigger-1; but instead of counters 1-4 and 9-12, it uses counters 5-8 and 13-16. Instead of T2 and T3, it requires that "PTOR" be satisfied, which is that 2 out of the 4 acrylic counters in the same quadrant in each of the half-carts fire their s-bits.

  Since trigger-4 makes stricter requirements than trigger-1, all of the trigger-4's should be included in the trigger-1 sample. This showed trigger-1 inefficiency to be less than 10^{-4}.

Trigger Type	E744	E770
1	1,740,427	1,981,136
2	2,267,724	2,915,707
3	1,611,230	2,001,988
4	696,664	806,985
5	16,447	64,627
6	166,682	1,406,410
Total	3,235,717	5,095,487

Table 3.1: Number of triggers written to tape in E744 and E770. Note that a single event can satisfy more than one trigger.

- **Trigger 5** ("Test Beam") was reserved for test beam running, which occurred in different spills from neutrino running.
- **Trigger 6** ("Straight Through Muon") was designed to select muons produced upstream of Lab E that pass through the entire detector (created by charged-current interactions in upstream material). One s-bit out of a set of 4 in each target cart must fire, along with the veto, and the muon must penetrate the toroid system and satisfy the PTOR requirement.

  The stiff muon tracks passing this trigger are used for calibration and drift chamber alignment. In E744 this trigger was pre-scaled down by a factor of 8. In E770 the trigger was generally not pre-scaled in order to accumulate additional events for counter energy calibration.

3.6 Data Acquisition

The raw data collected in both runs of the experiment consists of approximately 300 gigabytes of information. This raw data consists of the sum of the read-outs described above, namely:

- 6 trigger bits
- 7-channels of ADC information for each of 84 target counters
- TDC information for each of 84 target counters
- ADC and TDC information for the toroid acrylic counters
- TDC information for each drift chamber hit
- Flash ADC information for drift chamber hits

The toroid acrylic counters and the flash ADC information is not used in this analysis. The number of events for each trigger type is given below:

Once written onto tape, the data was "*stripped*" and then "*crunched*" to convert it to Data Summary Tapes (DSTs) of physics-relevant variables. The "Stripper" compressed and rewrote the data – for example, unpacking ADC pulse heights and subtracted their pedestal values. The stripped data was passed to the "Cruncher", which did most of the time-consuming data processing, turning raw data into physics variables like muon angle and energy. Pulse heights were converted to hadron energies, TDC times to hit positions, etc. A pattern recognition algorithm fits muon tracks to the hit positions, producing muon vertex angle from the target track and muon energy from the toroid bend angle.

During analysis, several flavors of DST were used with slightly different format. The format used in this analysis was the "SuperDST", which included the corrected counters pulse heights as well as crunched physics variables. These were read in by a program called PHDST, which applied some final corrections to the data as well as applying the cuts (see Data Analysis).

Chapter 4

Event Reconstruction

This chapter is devoted to how to reconstruct real physical quantities of a neutrino event in the CCFR target, based on the raw data output of the the hardware described in the previous chapter. This raw data must be used to eliminate all spurious triggers and measure all the relevant physics variables from true neutrino events.

For the structure function analysis measuring charged current events, only three variables are relevant in the end: the angle of the muon (θ_μ), the energy of the muon (E_μ), and the total energy of the hadron shower (E_{HAD}). The goals of the event reconstruction, then, are to convert the raw data output described last chapter into useful information: the three variables above plus well-defined variables for cuts. This occurs in several steps:

- The counter ADC information is combined to a single corrected pulse height from each counter.
- The pulse heights used to roughly determine the z-position of the interaction and the z-length of the shower.
- The drift chamber TDC information is used to track the path of the muon as it passes through the target and toroid. The track coming from the interaction is used to find the muon angle θ_μ.
- With the shower region identified, the hadron energy E_{HAD} is calculated.
- The muon path through the toroid magnetic spectrometer is fitted to find the momentum, which with added contributions for the muon energy loss in the target determines E_μ.

Each of these steps are covered in more detail in the following sections.

4.1 Pulse Heights

The calorimeter response to charged particle energy loss varies with the type of particle and how it tends to interact. We divide the calibration into (1) muon tracks, (2) hadronic showers, and (3)

electromagnetic showers.

As charged particles pass through the calorimeter, we can measure how much energy those particles are depositing, but only in small slices. Only roughly 3% of the mass of the calorimeter is "active" in detecting energy loss. Therefore, when we try to measure the integrated total energy loss, the *shape* of how it deposits energy between the slices is important.

The energy deposited in material is largely independent of energy at these levels, so calorimetry is dominated by the *number* of high energy particles at that point in the shower. The number of particles is roughly determined by measuring the summed pulse heights registered by the four phototubes on each counter. This sum is then converted into units of minimum ionizing particles (MIPs), where one MIP represents the average summed pulse heights resulting from a single particle passing through the counter. The MIP is the standard unit for calorimeter measurements.

Although the counters are identical in design, variations in the exact optical connection between the elements, as well as differences in their PMT gains and electronics cause their response to vary. Therefore, each counter is calibrated separately.

Counter Gain Calibration

The counters are calibrated using the truncated mean of muon energy deposition, since muon energy loss is well understood. Muon energy loss is roughly described by a Landau distribution, with a peak due to ionization (roughly independent of muon energy) and a long tail from "catastrophic" energy losses from bremsstrahlung, pair production, and delta ray production.

We use muons from trigger-6 data ("straight-through muons") and trigger-1 data ("charged-current interactions"), using the muon peak well downstream of any hadron shower. To remove systematic energy-dependent effects, we cut off the long tail of high energy loss by an iterative "truncated mean" procedure. For each counter, the mean of the high channel response distribution is taken. Then a new mean is calculated for the distribution from $0.2 \times mean$ to $2. \times mean$, and a new means calculated around that value until the series converges. This truncated mean of the high channel is defined to be one *MIP* for that counter.

Whereas muon energy is measured by the high channel, the hadron energy is measured by the low channels (or the super-low channels if the low channels are saturated). To convert the muon energy measured by the high channels to that measured by the low channels and the combination low channels, a set of inter-channel calibration coefficients are used. The relationships between the channels for each counter are in terms of the counter's calibration coefficients:

$$A_i^{COMBLO} = \sum_{j=1}^{4} \alpha_{ij} A_{ij}^{LO} \tag{4.1}$$

$$A_i^{HI} = \beta_i A_i^{COMBLO} \tag{4.2}$$

where A_i refers to counter i's response in a particular channel, β, is each counter's high-to-low channel calibration coefficient for each phototube j in counter i. The calibration coefficients are

determined by minimizing the quantities,

$$\sum_{events} \sum_{i=counters} \left(A_i^{COMBLO} - \sum_{j=1}^{4} \alpha_{ij} A_{ij}^{LO} \right)^2 \tag{4.3}$$

$$\sum_{events} \sum_{i=counters} \left(A_i^{HI} - \beta_{ij} A_i^{COMBLO} \right)^2 \tag{4.4}$$

Typical values are $\alpha = 0.8$ and $\beta = 12$. These quantities are determined to better than 1%, both because of good overlaps in the dynamic range of the channels and because small nonlinearities in the electronics were well understood.

Assuming no variation in response over time or position within a counter, the low channel energy in MIPs for each counter is given by:

$$\triangle E_i = \beta_i \sum_{j=1}^{4} \alpha_{ij} A_{ij}^{LO} \tag{4.5}$$

Map and Time Variation Corrections

A counter's energy response varies with the position of the ionizing particle, and in addition can vary over time. Particles striking at the center of the counter will have lower response due to absorption along the walls of the counter and attenuation of light in the oil. Particles striking near the phototubes at the corner have a high response due to increased acceptance and reduced attenuation. Over time, the phototube gains tend to drift and the scintillation oil degrades, which alter the counter response.

Thus, the counter pulse-height responses were corrected to account for these variations. First, a position-dependent map correction was applied based on a sampling of muon responses. Further, frequent measurement of phototube gains were made to account for detector changes over time.

The map corrections were determined by dividing the active area of the counter into 9x9 inch squares, and measuring the counter's response to muons in each of these position bins separately. The most probable value of the energy distribution for each square bin was determined by a truncated mean, and a bin center correction was made due to the variation of energy response within each bin. The final map correction R_N for counter N is given by the equation:

$$R_N^{map}(x, y) = \frac{\triangle E_N(x, y, t = 0)}{\triangle E_N(x, y, t = 0)} \tag{4.6}$$

To smooth the distribution within the bins, a 15-term fourth-degree polynomial in x and y was fitted to the table. A sample counter map is given in Figure 4.1, shown as a contour plot of muon response relative to the center of the counter.

The time variations in counter response are measured at the center of each counter, where the event population is the highest. To account for drift in phototube gains, the gain for each tube relative to the four in the counter is determined by the quantity:

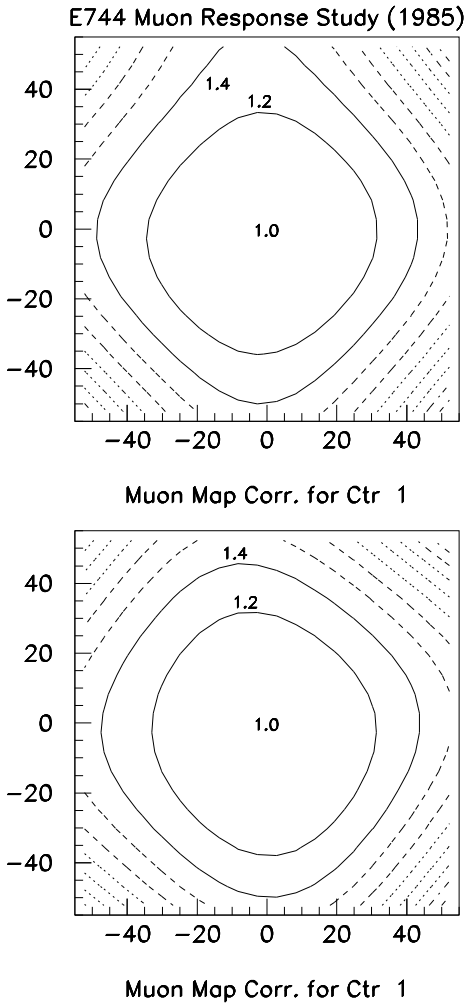

Figure 4.1: Contours of the relative muon response for counter 1. Separate studies were done in 1985 and 1988.

$$\beta_{N,i}(t) = \frac{4 \times \alpha_{N,i}(t) \times LOW_{N,i}(t)}{\sum_{j=1}^{4} \alpha_{N,j}(t) \times LOW_{N,j}(t)} \tag{4.7}$$

Measurements of the relative phototube gains were made frequently. At the start of E744 and at the start of E770, the phototube high voltages were grossly adjusted to equalize the relative gains of the counter's four tubes. In this procedure (known as "balancing"), a 1mCi source of ^{137}Cs was positioned at the rough center of the counter and the high voltages of each tube were set to make the tubes' anode currents equal to within $\pm 25\%$. The muon data were used to better determine the relative gain throughout the running. From time to time during the run, counters that fell severely out of balance were readjusted with the source.

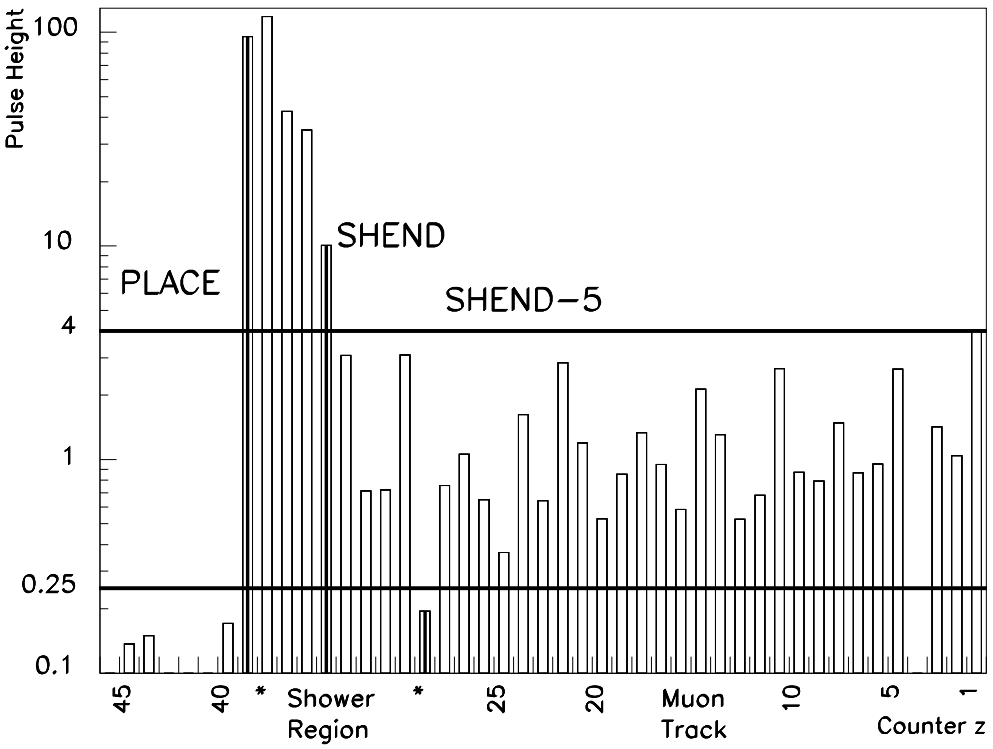

Figure 4.2: Pulse heights of an event versus counter number showing vertex PLACE and shower parameter SHEND. The shower region extends from PLACE to (SHEND-5). These are actual corrected pulse heights from event #111 from run #289 of experiment E744.

$$PH = \frac{\sum_{i=1}^{4} \alpha_{N,i}(t) \times LOW_{N,i}(t) \times \frac{\beta_{N,i}(t=0)}{\beta_{N,i}(t)}}{\frac{GAIN_N(t)}{HILO_N(t)} \times MAP_N(x,y,t=0)} - \sum_{k=1}^{\#\mu} \Delta(P_{\mu_k}) \tag{4.8}$$

Identifying Calorimeter Regions

The first use of the corrected pulse heights is to identify the extent of the interaction along the z axis of the detector. The beginning of the event is known as PLACE, which is in theory the number of first counter downstream of the vertex of the neutrino interaction.

This beginning of interaction should be marked by several large pulse heights caused by the start of the hadronic shower. However, there is the problem that upstream counters could have smaller pulse heights caused by counter noise or back-scatter from the interaction vertex. Thus PLACE requires that there be two counters each with pulse heights over 4 MIPs, in which case PLACE is the most upstream of the two counters. This is illustrated in Figure 4.2, which shows the pulse heights from a single event in experiment E744.

SHEND is the counter number which roughly defines the end of the hadronic shower. SHEND is the most upstream counter which is followed by three consecutive counters with less than 4 MIPs. Note that since the muon track should have average pulse height of 1, it is likely that counters downstream of SHEND will still have energy from the tail of the hadron shower. Thus, the true end of the shower is a small number of counters beyond SHEND.

Using these definitions, we can then break up the

Shower Region: This is the region dominated by hadronic shower, extending from the vertex (PLACE) to the tail of the shower (SHEND-5). This region is used to calculate the hadronic energy, and here the muon energy loss is not measured because it is mixed with the larger hadron energy loss.

Muon Track: This is the region in the calorimeter downstream of the hadronic shower, from (SHEND-6) to counter #1. Here the pulse heights of the counters represent muon energy loss.

Toroid: This is the toroidal magnetic spectrometer, where the muon energy is measured by the bend in the muon track. Scintillation counters here are used in triggering by confirming the presence of a muon, but are not used directly in the analysis.

These regions are illustrated in Figure 1.2. Note that this shows the pulse heights from an actual event in experiment E744.

4.2 Hadron Energy Measurement

The hadron energy is based on a simple sum of counter pulse heights within the shower region (PLACE to SHEND-5). The energy deposited by the muon must be subtracted from this – again requiring the assumption of average deposition by the muon.

Thus, the pulse heights are totaled, then the average expected pulse heights from the muon over that length is subtracted. Thus, if the pulse heights are below average for a small shower, it is possible for the measured E_{HAD} to be negative.

Converting MIPs to Energy

The target calorimeter was calibrated on an absolute scale twice with hadron test beams [Sak90]. The test beam was dominantly pions with a precisely-selected momentum, but there were impurities. For the positively-charged test beam, the proton fraction was about 20% at 100 GeV and increased with energy to 50% at 300GeV. Electrons were a significant component at low energies, amounting to 10% at 50 GeV and increasing with decreasing momentum. The kaon fraction was 5% or less, while muons were on the order of a percent (increasing with decreasing momentum).

The calibration data was separated into muon, hadron, and electron events. The results for the hadron test beam runs are shown in figures 4.3 and 4.4.

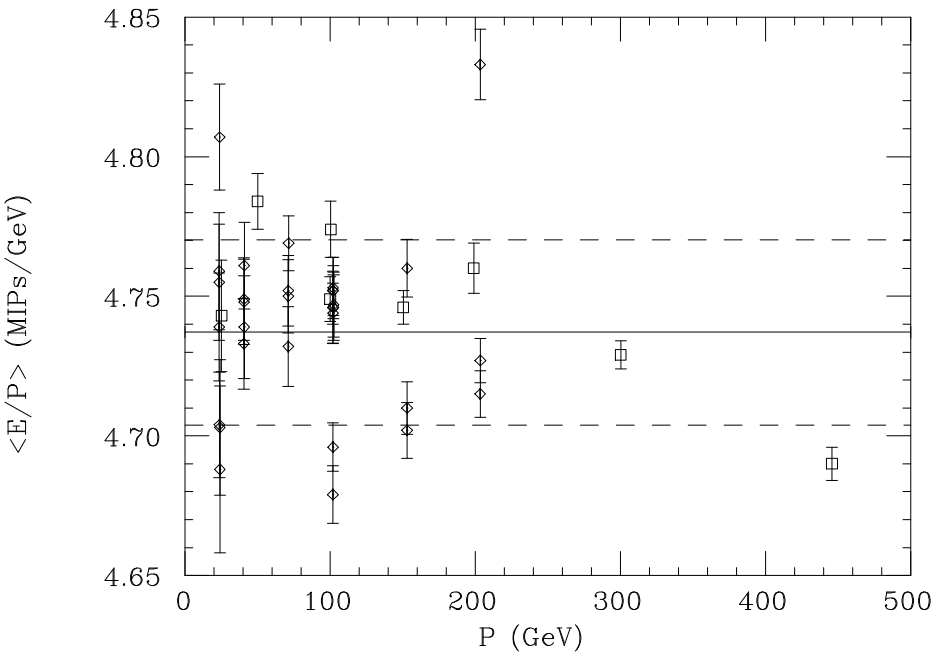

Figure 4.3: Energy response of the CCFR calorimeter, relating MIPs to GeV. Hadronic test beam data data are for E744 (squares) and E770 (diamonds). The horizontal line is a weighted mean of the E770 points, with the dashed lines representing one sigma dispersion about the mean.

The figures show the comparison of p, the true test beam momentum as measured by an upstream spectrometer, with E, the total pulse heights recorded by the calorimeter in MIPs. The average ration, $< E/p >$, defines our calibration constants for converting measured MIPs to actual GeV.

The test beam further tells us the energy resolution of our calorimeter (i.e. the error in our measurement E). For hadrons, this was determined by fitting Gaussian distributions to the two highest-statistics momentum runs: $P = 25\ GeV$ and $P = 200\ GeV$. This was extrapolated to all momenta by assuming the form of two terms: a 'resolution' term proportional to $1/\sqrt{P}$ and a 'noise' term proportional to $1/P$.

$$\frac{\sigma}{E} = \frac{(0.847 \pm 0.015)}{\sqrt{P}} + \frac{(0.297 \pm 0.115)}{P} \tag{4.9}$$

This is consistent with all the other test beam runs, as shown in Figure 4.5.

This calibration and resolution was also done for electrons using beams of $P = 25\ GeV$ and $P = 50\ GeV$. These did not appear to have a strong 'noise' term, and thus were fitted assuming a single $1/\sqrt{P}$ resolution term:

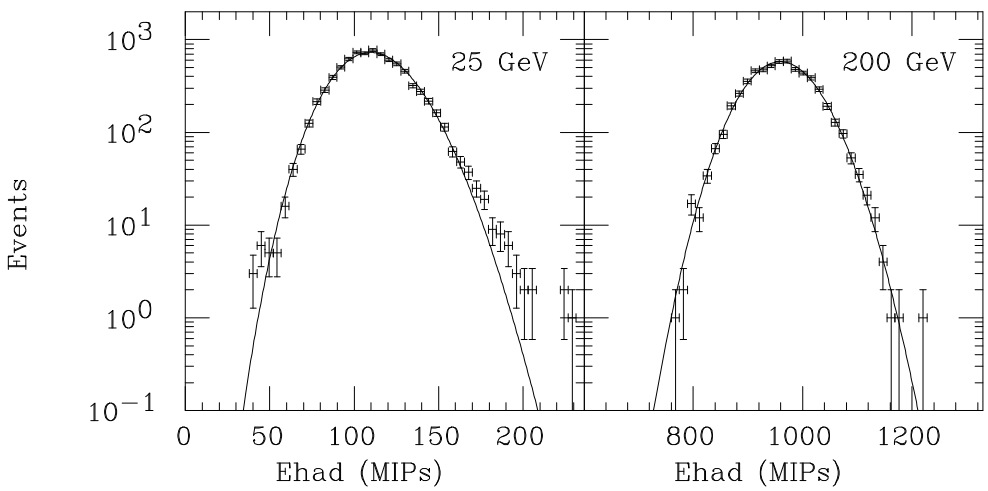

Figure 4.4: Distribution of reconstructed hadronic energy for 25 and 200 GeV test beam hadrons, taken in 1987. The curves show the Poisson-like parameterizations of this data.

Finally, the calibration was checked for low-energy muons which ranged out in our detector. At low energies, muon energy loss is dominated by ionization which is constant. Thus, we determine the muon energy directly from how far it travels in our detector before stopping (independent of the counter pulse heights). This used range-energy tables measured at Fermilab [Koi78]. With this assumed 'true' energy, we measure the average counter response and resolution. The resolution was found to be $\sigma_\mu/E = 0.17$.

Parameterized Muon Subtraction

The hadron energy is based on a simple sum of counter pulse heights within the shower region (PLACE to SHEND-5). The energy deposited by the muon must be subtracted from this – again requiring the assumption of average deposition by the muon.

The pulse heights are totaled, then the average expected pulse heights from the muon over that length is subtracted. Thus, if the pulse heights are below average for a small shower, it is possible for the measured E_{HAD} to be negative.

$$R_{MIP} = 0.92546 + 0.02418\ \log(E_\mu) \tag{4.10}$$

Here E_μ has a minimum of 0.1 GeV in this equation.

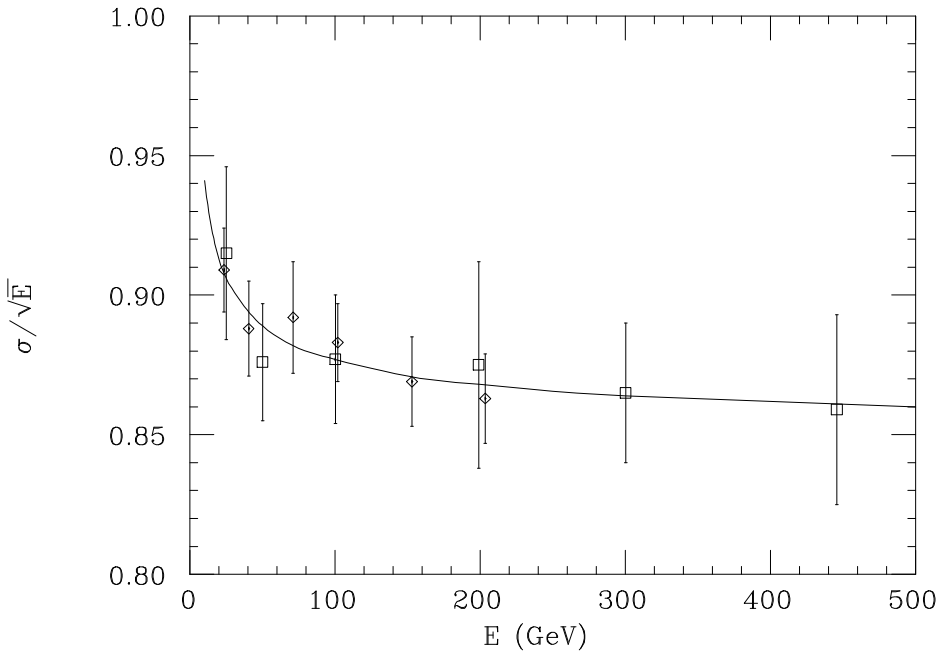

Figure 4.5: The fitted energy resolution for all test beam runs, ranging from 24 to 240 GeV. The curve is the resolution-versus-energy function shown in equation 4.9.

4.3 Muon Tracking

Muons in the CCFR detector will penetrate about 3 out of the 42 target drift chambers for every GeV of energy they have. On average, then, the primary muon (i.e. created directly by the CC neutrino interaction) will penetrate the entire target and penetrate through into the toroid where it is bent by the magnetic field there.

The muon is measured primarily by the drift chamber hits, which are linked together into tracks by various software algorithms. The hits in the target chambers are considered to be straight, and are fitted to calculate the muon angle θ_μ – i.e. the geometry of the CC neutrino interaction. The hits in the toroid chambers are considered to be bent according to the magnetic field, starting with the angle in the target. They are fitted to determine the muon's momentum at the front face of the calorimeter (E_μ^{FF} or EMUFF).

Complicating both measurements is the effect of multiple Coulomb scattering in the target and toroid steel. Due to scattering, θ and E_μ^{FF} are correlated, necessitating that they be determined together using an iterative procedure.

At the start of the iterative track fitting procedure, a line segment is chosen in the calorimeter

Type of signal	Calibration	σ/E
π	$4.73 \pm .02 MIPs/GeV$	$0.847/\sqrt{E} + 0.30/E$
e	$5.25 \pm .10 MIPs/GeV$	$0.60/\sqrt{E}$
μ	$6.33 \pm .17 MIPs/GeV$	0.17

Table 4.1: Calibration constants and energy resolution of the CCFR detector.

to fit the hits in the eight most downstream chambers. This line segment is extended upstream to PLACE, and in the first pass scattering effects are neglected. In the toroid spectrometer, line segments are fit to the hits in each set of five chambers following each toroid cart. A crude initial estimate of the muon momentum is made by using the track deflection $\triangle\theta_{bend}$ in the first toroid gap:

$$p_\mu = \frac{0.3 < B > L_k}{\triangle\theta_{bend}} \tag{4.11}$$

where $L_k = \rho\triangle\theta_{bend}$ is the distance traversed in the magnetic field in centimeters, ρ is the track's radius of curvature, and $< B >$ is the mean magnetic field strength in kilogauss: 17 kG.

In the next iteration, the initial determination of p_μ is used to include scattering effects. A particle with momentum p_μ traversing a distance L_k in a material with radiation length X_0 will undergo a mean Coulomb scattering deflection σ_k. This mean deflection is used over each discrete track segment to form a χ^2 function, which is minimized to fit the track.

$$\chi^2 = \sum_i \sum_j (x_i - x_i^p) M_{ij}^{-1} (x_j - x_j^p) \tag{4.12}$$

$$M_{ij} = < (x_i - x_i^p)(x_j - x_j^p) > \tag{4.13}$$

$$= \sum_{k=1}^{i} \sigma_k^2 \left[\frac{L_k^2}{3} + \frac{L_k}{2}(z_{kj} + z_{ki}) + z_{ki} z_{kj} \right] + \sigma_0^2 \delta_{ij} \tag{4.14}$$

$$\sigma_k = \frac{0.015}{p_\mu} \sqrt{L_k / X_0} \tag{4.15}$$

where here x_i are the measured chamber hit positions, and x_i^p are the predicted track positions in the i-th plane. L_k is the distance from k-th to the $(k+1)$-st chamber planes, z_{ki} is the distance from the k-th to the i-th plane, and σ_0 is the intrinsic drift chamber resolution ($= 225\ \mu m$). The track fit through the toroid includes the full error matrix, while the fit in the target omits the off-diagonal Z_{ki} terms.

The vertex angle is determined by fitting the track near the vertex at position V_Z. However, the large number of hits near the vertex from particles in the hadron shower limits the tracking ability. As

Track Length	$E_{HAD} < 25\ GeV$		$25 < E_{HAD} < 50\ GeV$		$E_{HAD} > 50\ GeV$	
(chamber)	A	B	A	B	A	B
4	0.535	35.4	0.547	46.0	0.407	75.0
5	0.366	49.5	0.393	57.3	0.343	77.8
6	0.294	56.6	0.361	59.4	0.260	84.9
7	0.235	61.5	0.337	62.2	0.235	87.0
8	0.235	61.5	0.337	65.8	0.235	87.7

Table 4.2: Constants A and B for muon angular resolution within the calorimeter, shown as a function of hadron energy and track length.

a result, a few chambers nearest the vertex are not used for tracking. The number of drift chambers nearest the vertex position that are omitted from tracking is known as the tracking vertex offset. A study of trigger-1 (charged-current) events determined the magnitude of the offset as a function of hadron energy and track length [Rab92]. To include a chamber in the track fit, the probability for choosing a good hit had to be twice that of selecting a bad one. Using this criterion, the study found that events with $E_{HAD} < 25\ GeV$ require no offset, those with $25 < E_{HAD} < 50\ GeV$ should be offset by one chamber, and those with $E_{HAD} > 50\,GeV$ should be offset by two chambers. Including the E_{HAD} offset, hits in the six chambers closest to the vertex are fit to a line making angle θ_μ with the beam axis.

The resolution of the muon angle at the event vertex is limited by the muon momentum and the hadron energy. Scattering effects are most severe at low muon momenta, as seen from the equations above, whereas large hadron energies lead to high hit multiplicities that make tracking near the vertex difficult. The angular resolution was determined by studying the trigger-6 sample of stiff muon tracks ($75 < p_\mu < 200\ GeV/c$), by comparing the track angle determined by upstream and downstream track segments on either side of a simulated "vertex" chosen at the center of the track. The angular resolution was found to be [Kin94]: $\sigma_\theta = A + B/p_\mu$, in milliradians. The parameters A and B are given by:

$$\sigma_\theta = A + \frac{B}{P_\mu}\ (mrad) \tag{4.16}$$

Since the muon angle measurement depends on the magnitude of the muon momentum, the θ_μ measurement is repeated, using the more precise measurement of E_μ^{FF} from fitting the muon track through the toroid spectrometer.

4.4 Muon Energy Measurement

The muon energy is reconstructed in three parts. Track fitting in the toroid spectrometer determines the muon energy at the front face of the toroid. However, the energy lost within the calorimeter must also be accounted for. Downstream of the hadron shower, this is done by summing up the scintillator pulse heights, calibrated from background muons. Within the region of the hadron shower (PLACE to SHEND-5), hadronic hits are overlaid with the muon pulse heights. Here we assume average muon energy loss, using the R_{MIP} function (Equation 4.10).

$$E_\mu = E_\mu^{FF} + \sum_{i=1}^{SHEND-6} C_\mu^{eff}(PH) \times PH + \sum_{i=SHEND-5}^{PLACE} C_\mu R_{MIP}(E_\mu) \quad (4.17)$$

$$C_\mu^{eff}(PH) \times PH = \begin{cases} C_\mu \times PH & PH < 3\ MIP's \\ (C_\mu \times 3) + (C_e \times (PH - 3)) & PH > 3\ MIP's \end{cases} \quad (4.18)$$

The muon momentum measurement requires a detailed map of the muon spectrometer's toroidal magnetic field. Such a map was prepared from Hall probe measurements of the field strength at numerous points along gaps in the magnets and from measurements of the current in the magnet windings, up to a single overall normalization, N_{field}. This normalization was determined using momentum-analyzed muon test beam.

The muon momentum measurement is made via an iterative procedure, using the same algorithm used to track the muon in the target. Using the initial determination of the muon angle and position at the front face of the spectrometer, the predicted muon trajectory is extrapolated through the magnets in 4-inch steps, and the energy loss due to ionization is accounted for in each step. The predicted muon track is compared to the hits in the drift chambers located between the toroids, and a χ^2 function comparing the predicted and measured hit positions(Equation 4.12) is minimized by varying the momentum. With each new momentum determination the full error matrix is recalculated. This procedure continues until the momentum differs by less than 0.5% from the previous iteration.

Coulomb scattering creates an absolute limit on the resolution of the spectrometer momentum measurement. This can be estimated by considering a track that traverses the entire spectrometer: receiving a transverse momentum kick of 2.4 GeV/c from the magnetic field, and passing through 500 cm of steel. The mean Coulomb scattering deflection is then given by

$$\frac{\sigma}{p_\mu} = \frac{\triangle\theta_{Coulomb}}{\triangle\theta_{Magnet}} = \frac{\left(\frac{0.015}{p_\mu}\sqrt{500/1.76}\right)}{2.4/p_\mu} = 10\% \quad (4.19)$$

The spectrometer resolution was measured using a $120 GeV/c$ muon test beam [Kin91]. Figure ?? shows the experimental resolution function obtained. The central region is well approximated by a Gaussian distribution with an RMS width of 10.1%, as expected.

The z-position of the vertex V_X is assigned to be halfway between $PLACE$ and the next counter upstream (i.e. in the intervening steel plates).

4.5 Analysis Cuts

Once the data has been analyzed, we need to define a select sample of which events we want to use in our analysis. This is a double-edged sword, however. On the one hand, the events should represent real, well-measured neutrino events. At the same time, a cut should not be applied unless the quantity being cut on is well understood – or else the acceptance corrections for that cut will be wrong.

Table 4.3 shows the analysis cuts and their rejection rates. The total rejection rate is the percentage of total data events a cut rejects (including all backgrounds). The exclusive rejection rate is the percentage of events which are rejected solely on the basis of that cut. Key cuts will have relatively high exclusive rejection rates.

Fiducial Volume Cuts

These are cuts based purely on the determination of when and where the neutrino interaction occurred. We want to strictly define a fixed volume inside of which we understand the effects very well. This volume needs to be constant for the cross-sectional analysis to work.

- RUN+IGATE
  Certain runs were identified as 'bad' due to temporary problems with the detector at that time. The run number is simply matched against the list of bad runs. IGATE is the timing gate in which the event occurred.
- NSTIME
  The time of the event must match with the time of the fast-spill "ping" of protons on the primary target.
- PLACE
  This assures that the z-vertex of the interaction (expressed as the number of the PLACE counter) is between 20 and 80. PLACE above 80 often indicates a non-neutrino event resulting from a muon or other particle from upstream. Inefficiencies in counters 83 and 84 would make this appear as a neutrino event. PLACE below 20 means that the hadron shower may extend beyond the calorimeter and not be well-measured.
- VERTX/Y
  This assures that the vertex is close to the center of the detector in x and y. Events near the edge will often have particles which exit out the side of the detector and are not measured.

Cut #	Name	Definition	Total Rej.	Exclusive Rej.
1(1)	ALL EVENTS			
2(2)	RUN+IGATE	Bad Runs	15.83%	0.00168%
3(3)	NSTIME		1.60%	0.163%
4(4)	PLACE	$20 \leq PLACE \leq 80$	44.70%	2.271%
5(5)	VERTEX/Y	$ABS(V_X/V_Y) \leq 50$	24.33%	1.085%
6(6)	RADIUS	$RADIUS < 99.$	4.282%	0.000%
7(7)	TRIGGER 1		61.08%	0.0527%
8(8)	TARGET TRK		33.67%	0.000%
9(9)	IFIDMC	Projected $R_{FF} < 64.$	19.63%	0.055%
10		Projected $(X_{T2}, Y_{T2}) < 55.$	23.29%	0.339%
11		$PSTEEL > 80\%$	1.57%	0.456%
12(10)	TOROID TRK		41.24%	0.000%
13(11)	GOOD FIT		18.69%	0.000426%
14(12)	CHI/DF		47.46%	0.00530%
15(13)	TWO GAPS		45.23%	1.003%
16(14)	THETA	$0. < \theta_\mu < .15$	40.46%	0.0439%
17	(Hole Cut)	$\theta_\mu > .007$ or $R_{FF} > 6.$	0.053%	0.00025%
18(15)	EMU	$15. \leq E_\mu$	8.72%	0.0891%
19		$E_\mu \leq 600.$	29.12%	0.000%
20		$E_\mu^{FF} > 3.$	0.66%	0.00002%
21(16)	EHAD	$SHEND - 5 \geq 1$	8.42%	0.0159%
22		$10. \leq EHAD$	43.87%	2.099%
23		$E_{HAD} \leq 600.$	0.13%	0.000%
24(17)	QSQ	$1. \leq QSQ$	25.82%	0.541%
25		$Q^2 \leq 1000.$	2.85%	0.000058%
26(18)	ENU	$30. \leq E_\nu$	7.08%	0.0085%
27		$E_\nu \leq 600.$	29.164%	0.0101%

Table 4.3: Definitions and rejection rates of the analysis cuts. The total rejection rate is the percentage of total data events this rejects. The exclusive rejection rate is the percentage of events which are rejected solely on the basis of that cut.

Dimuon Cut

This cut eliminates events with a second muon track that either enters the toroid spectrometer, or penetrates more than 19 counters (implying an energy $> 3\ GeV$). These events are cut because for low values of x it can be hard to distinguish which muon came from the direct neutrino interaction

and which came from a decay in the hadronic shower.

Geometric Cuts

These cuts are meant to assure good momentum resolution in the toroid spectrometer. This is very tricky because we have less information about exactly what occurred in the toroid, and it is difficult to simulate exactly.

Thus, where possible the cuts are based on the better-known quantities measured in the calorimeter.

- TRIGGER 1
  This is the charged current trigger, which is activated by a particle passing through a set of counters between the first and second toroids (sometimes called the 'T2' point). This is required for the muon to be well measured within the toroid.
- TARGET TRK
  This is the requirement that a good muon track is found within the target calorimeter. This is necessary for an accurate measure of THETA.
- IFIDMC
  To determine muon acceptance, the muon direction from the vertex is geometrically extended as a straight line through the toroid. Note that this is different (and better understood) than the true muon track which has bends due to scattering. The extrapolated track must have a radius at the front face of the toroid $R_{FF} < 64\ in$; must have a radius at the T2 counter $R_{T2} < 55\ in$, and must have 80% of its length within the steel of the toroid.

  The extrapolated track is used instead of the true track because the exact bending of a true muon track is difficult to simulate in a Monte Carlo. The extrapolated track is simpler and better understood.
- TOROID TRK
  Enough hits must be detected in the toroid drift chambers for a muon track to be identified in the toroid.
- GOOD FIT
- CHI/DF
  The χ^2 of the fit must be less than 10. Note that the number of degrees of freedom is the number of chambers that the muon passed through in the toroid, and the following cut assures that the muon will pass through at least 10 chambers.
- TWO GAPS
  This requires a linked track segment in at least 1 of the two toroid gaps, for each of the x- and y-views. In effect, this requires that the muon track must pass through both the first and second toroid carts, to assure good reconstruction efficiency of the muon momentum.

Cross-sectional Cuts

These cuts are used in the cross-sectional analysis, and are intended (along with the previous cuts) to assure that the muon is well-measured.

- $\theta_\mu < 150\ mr$ and $R_{FF} > 8\ in$
  The muon angle cut assures good acceptance of the muon track as it passes through the toroid spectrometer. R_{FF} is the radius of the actual muon track at the front face of the toroid. This radial cut assures that the muon does not pass through the hole in the center of the spectrometer where the magnetic fields are not well measured.

- EMU: $15 < E_\mu < 600\ GeV$ and $E_\mu^{FF} > 3\ GeV$
  Very high energy muons have almost straight tracks in the spectrometer, resulting in poor momentum resolution. Further, the chance of catastrophic energy loss (such as bremsstrahlung) rises linearly with energy, creating background hits which can confuse the tracking. Low energy muons have poor resolution due to multiple Compton scattering.

Structure-Function Cuts

These are cuts on the reconstructed kinematics of the event, which are well-understood. The events are cut because they are needed for other data sets, or because they are not well modeled in the theory or monte carlo.

- EHAD: $10 < EHAD < 600\ GeV$
  Low hadronic energy events are used to determine the flux of neutrinos in a parallel analysis. Thus, we require $EHAD > 10\ GeV$ to minimize the correlations between the flux and structure-function data sample. Very high hadronic energy means low muon energy because of the ENU cut (see below). In this case, the low-energy muon is difficult to distinguish from the very large shower.

- QSQ: $1 < Q^2 < 1000\ GeV^2$
  Very low Q^2, "quasi-elastic" events are not well understood in our assumed cross-sectional model. This cut minimizes their effect. Very high Q^2 events are almost entirely mis-measurements.

- ENU: $30 < E_\nu < 360 GeV$
  The flux is only well-measured within a certain range simply by statistics. We want to restrict the analysis to where there is a reasonable set of both flux and SF data. The lower limit of 30 GeV was chosen because below that energy a large acceptance correction is required. The upper limit was chosen because above that energy the error on the Monte-Carlo smearing corrections becomes greater than 10%. Also the number of anti-neutrino events above $360 GeV$ is small and hence would not make a significant impact on the analysis.

Chapter 5

Event Monte Carlo

The detector acceptance and energy resolution in this analysis were modeled by a detailed Monte Carlo simulation program called NUMONTE. This was used to check various of the detector corrections used in the analysis. The NUMONTE program is available for collaborators through a file management system called CVS. The complete documentation and code is accessible by the World-Wide-Web at:

`http://www-e815.fnal.gov/~jhkim/numonte.html`

5.1 Purpose

NUMONTE is a "fast" Monte Carlo which can simulate several million events in a matter of hours on our machines. It does this largely by relying on empirical tests of our detector's behavior rather than tracking individual particles. The only individual particles that it tracks are high energy muons which come from the neutrino interaction.

Within the GLS analysis, NUMONTE was used for investigating possible systematic errors. The structure function extraction was done earlier using a separate fast Monte Carlo [Sel97], whose output re-weighted to account for new effects. The formulas used by the two Monte Carlos are largely the same, and they were checked against the same data sample. NUMONTE was developed as a streamlined and faster program with the capability to investigate possible new effects. It was developed from a program used for simulating neutral current events (NCMONTE), and added tracking of muons through the toroid spectrometer.

The overall purpose of NUMONTE was to create a single analysis program that could be used for *all* analyses, including neutral current, cosmic ray, structure function, and others. Then new features were added which could be shared by all of these and which would be consistent throughout. Some examples of new feature include:

- "Higher Twist" cross-section options: NUMONTE includes calculated cross-sections based on

various theoretical models including target mass, meson vector dominance, elastic scattering, and others.

- Dimuon event generation: Options allow separately tracking events which produce high energy muons from the vertex or hadron shower and tracking that extra muon. (In normal running, the individual particles in the hadron shower including muons are not tracked.)
- Modified energy smearing: The default handling of energy smearing in NUMONTE was modified based on the muon tracking and studies done on very high energy cosmic rays.

5.2 Methodology

The program is designed to simulate actual neutrino events that occur in our detector – but restricts itself to those results which are most important to our analysis. With each iteration of the main program loop, it simulates a neutrino interaction within the primary portion of our detector and randomly determines how it is effected.

It does not simulate any background events caused by cosmic rays or other incoming particles: these are removed from our event sample by a stringent set of cuts.

In general, we randomly select each variable based on an empirically-determined distribution. This is usually based on a test sample of events: either test-beam events or a selection of neutrino events (separate from other events used in analysis). We use this sample to determine a distribution of how the variable goes, and then use a random number generator to pick a point on that distribution.

5.3 Overview

The program is basically broken up into three sections. First, we simulate the neutrino flux which enters our detector. Next we simulate the cross-section of that neutrino interacting. Finally we simulate the effects of that reaction on the detector.

1. **Neutrino Generation** (directory `/flux`)
   - `itype` : neutrino type (in FLUXGET)
     Choice of Muon- or electron-associated neutrino or anti-neutrino, based on study of low hadronic-energy events (see Section 6.3)
   - `enu` : neutrino energy (in FLUXGET)
     Based on study of low hadronic-energy events (see Section 6.3)
   - `vxg,vyg` : vertex position (in FLUXGET)
     Choice of X & Y coordinates of the neutrino interaction, based on a large sample of interactions in the detector

- `placeg` : vertex Z-position (in FLUXGET)
  PLACE is effectively the Z-position along the length of the detector, an integer number from 1 to 84 for the closest counter number. PLACEG is the "generated" or true PLACE (as opposed to the reconstructed PLACE). It known to be a flat distribution due to the regular construction of the detector.

2. **Cross-section Throw** (directory `/crossec`)

   - `xg` : true Bjorken X (in MCKINEM)
     Flat distribution
   - `yg` : true Bjorken Y (in MCKINEM)
     Flat distribution
   - `xsec*` : Calculate the cross-section for that x and y (in MCKINEM)

   - `ehadg,emug,thetag` : true hadron/muon energies and true muon angle calculated from `xg` and `yg` (in MCKINEM)
   - `wt2mu` : chance of a dimuon event, calculated in KINEM_ALT and thrown in the main program

3. **Detector Simultion/Smearing** (directory `/detector`)

   - `place` : smeared vertex Z-position (in FNDPLAC)
     Reconstructed Z-position of the vertex (known only as the closest counter number 1-84). The true PLACE is shifted using a random throw based on a GEANT/GHEISHA calculation using as input neutrons of energy 25, 50, 100, 200, 300, and 500 GeV.
   - `shend` : hadron shower length (in SHWREND)
     This is an arbitrary measure of the length of the hadron shower, defined as being when the counter response drops below a certain level. It's distribution for a given shower energy is extrapolated from test-beam data.
   - Track the primary muon (in TRACKMU and MAGPRJ)
     This simulates the muon passage using parameterized scattering and energy loss through the whole detector. This information is *only* for triggering and calorimeter response.
   - `theta,phi` : muon angle (in THETASMR)
     This smears the true muon angle based on a study of tracking using background straight-through muon tracks.
   - `emuff` : muon energy at the front face of the toroid spectrometer (in EMUSMEAR)
     This smears the muon energy based on a test-beam muon run, with added effects for chamber resolution and acceptance.
   - `emu` : total muon energy (in EMUSMEAR)
     This adds in visible muon energy loss in the calorimeter to the muon energy, using the same procedure as the data. The simulated pulse heights are based on studies of straight muons and test beam.

- `ehad` : hadron shower energy (in HADSMEAR)
  This smears the true hadron energy using a resolution function based on test-beam hadrons. It also adds in simulated muon pulse heights within the shower.

The neutrino is generated by a random throw against the relative flux that was extracted for this run.

5.4 Muon Tracking

The muon is tracked through the target by stepping through each counter-unit (two 2-inch plates of steel and a scintillation counter) and calculating energy loss and scattering. This tracking information is not used for many purposes in the Monte Carlo because we rely on empirical distributions which average over many muon track directions. It is used for determining:

1. Simulated counter pulse heights beyond the hadron shower
   This is used to calculate the total smeared muon energy by converting the simulated pulse heights. Within the hadron shower, the pulse heights are not properly simulated, since NUMONTE does not simulate the shape of the hadron energy deposition.
2. The exit point of the event in the calorimeter (CEXIT)
   This is less relevant to the charged current analysis, but it is the defining parameter in the neutral current analyses which measure $sin^2\theta_W$.
3. The number of magnetic toroids traversed before exiting
   This is used as a scale factor on the resolution of the magnetic spectrometer. If the muon only passes through a fraction of the toroid, the spectrometer has proportionally worse resolution. Note that the smeared momentum measurement does not actually depend on the simulated track except for this gross factor. Reproducing the actual fitting procedure used on the data would be much too time-consuming for the monte carlo.

Muon dE/dX Calculation

The simulated muon energy loss within the detector is handled by a calculation from a routine called DEDX, originally written by M. Mugge. This routine has been used for all analyses, but the exact input and calculation within it have been modified.

The muon energy loss is broken up into two categories: restricted and catastrophic. Restricted loss is a fixed function of the muon energy and amount of material. Catastrophic energy loss is stochastic, and is based on a random throw within DEDX.

There are three inputs to the DEDX calculation:

LENGTH is the amount of material which the muon passes through, in units of inches of iron. This is set based purely on the mass of the detector and dividing by the density of iron. In this analysis, LENGTH was set to 4.412 inches per counter within the calorimeter.

SCALE1 is the ratio of restricted energy loss in the detector versus restricted energy loss for an equivalent mass of pure iron. This is obviously 1 for pure iron, and was set to 1.005 based on the average $dE/dX\ |_{min}$ of all the detector materials. (See Appendix C.)

SCALE1 is the ration of catastrophic energy loss in the detector versus such loss in pure iron. This was set to 0.949 based on the average radiation length of all the detector materials. (See Appendix C.)

Muon Scattering Calculation

The muon scattering is based on basic multiple Coulomb scattering within the target. This is done by a single Gaussian random throw for each counter that it passes through.

$$\sigma(\frac{dx}{dz}) = \frac{0.014994}{p_\mu}\sqrt{L}\left(1 + \frac{\log_{10} L}{9}\right) \tag{5.1}$$

where L is in (inches of steel times 1.44321).

5.5 Muon Energy Smearing

The muon energy in the data is formed by the sum of three quantities. First, the unseen muon energy loss in the hadron shower region (PLACE to SHEND-5), which is assumed to be average. Second is the muon energy loss in the calorimeter downstream of the shower, which is converted to GeV using the muon calibration constant. Third is the muon energy at the front face of the toroid, determined by track fitting in the spectrometer.

$$E_\mu = E_\mu^{FF} + \sum_{i=1}^{SHEND-6} E_i^{ctr} + \sum_{i=SHEND-5}^{PLACE} R_{MIP}(E_\mu) \tag{5.2}$$

Here E_μ^{FF} is the reconstructed energy of the muon at the front face.

Spectrometer Simulation (E_μ^{FF})

The resolution of the toroid spectrometer (E_μ^{FF}) was measured by a test beam run of 120 GeV muons [Kin91]. However, only a single angle and energy of muons had sufficient statistics for a good measurement of this. NUMONTE attempts to scale this distribution so that it applies to all energies and angles.

The basic energy resolution is a direct binning of the measured spectrometer resolution, shown in Figure 5.1. This is shown as the error in the inverse of muon energy

$$R \quad = \quad \left(\frac{1}{P_\mu(meas)} - \frac{1}{P_\mu(true)}\right) / P_\mu(true) \tag{5.3}$$

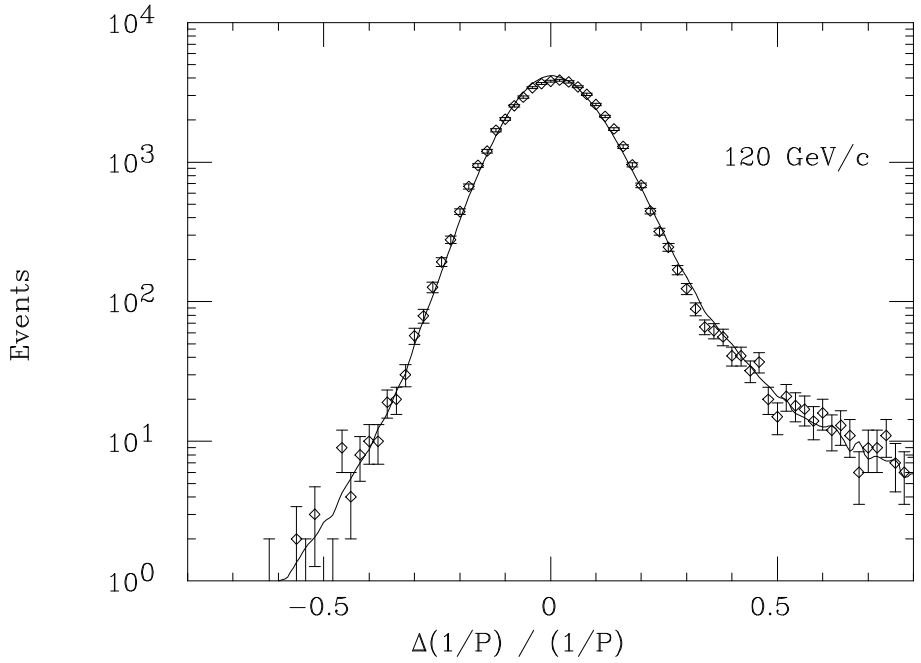

Figure 5.1: Muon momentum resolution in the toroid spectrometer, as measured by 120 GeV test beam muons. The points are the measurements of test beam muons, the solid line is an independent prediction.

This resolution is primarily due to multiple Coulomb scattering in the steel, which has a cross-section proportional to $1/P_\mu$ as explained in Section 5.4. Since the muon bend angle is also inversely proportional to momentum, this resolution should be roughly independent of energy.

Thus, the shape of R measured at 120 GeV is retained for all energies. This is corrected for two factors. First, the resolution is modified based on the number of toroidal magnets which the muon passed through. The test beam passed through all three toroids, so the resolution is decreased proportionally if a muon passes through fewer magnets. Second, a small term is added for chamber resolution, which is negligible at 120 GeV but becomes very important for very large momentums.

$$R \quad = \quad R_0 + 0.00004 * (P_\mu - 120.) \tag{5.4}$$

Muon Pulse Heights

Downstream of the hadron shower, the data uses the scintillator pulse heights to determine muon energy loss. In NUMONTE, the simulated pulse heights are proportional to true muon energy loss (cf. muon energy loss above) plus Gaussian smearing terms.

This reproduces well the distribution of muon energy loss averaged over several counters (10+). However, it does not simulate the distribution of individual counter pulse heights. In the data, a catastrophic loss of muon energy will result in an electromagnetic shower which, if large enough, may

extend across two or more counters. NUMONTE does not attempt to simulate the electromagnetic shower shape. Thus, it places all of the energy in the counter immediately following the loss.

The Gaussian smearing terms are handled separately for restricted and catastrophic loss. The restricted loss smearing is based on a study of straight-through muons, while the catastrophic loss is based on electron test beam studies. The total energy returned is then:

$$E(sim)\ |_1^{SHEND-6} = \sum_{i=1}^{SHEND-6} \begin{cases} C_\mu \times E_i^{ctr} & E_i^{ctr} < 3 \\ (C_\mu \times 3) + (C_e \times (E_i^{ctr} - 3)) & E_i^{ctr} > 3 \end{cases} \tag{5.5}$$

where E_i^{ctr} is the simulated MIP response, map corrected using an "estimated" muon position at that counter. The basic simulation is the sum of restricted and catastrophic simulated responses, which are each Gaussian smeared for energy resolution and map smeared for the true position of the muon.

$$E_i^{ctr} = \frac{E^{ctr}(res) + E^{ctr}(cat)}{XMUCORR(x_{est}, y_{est}, i)} \tag{5.6}$$

$$E_i^{ctr}(res) = \frac{resloss}{C_\mu} \times XMUCORR(x, y, i) \tag{5.7}$$

$$\sigma(resloss) = 0.360 \times C_\mu \tag{5.8}$$

$$E_i^{ctr}(cat) = \frac{catloss}{C_e} \times XMUCORR(x, y, i) \tag{5.9}$$

$$\sigma(catloss) = 0.60 \times \sqrt{catloss} \tag{5.10}$$

The restricted smearing in each counter is smeared by a Gaussian based on studies by Len Bugel using straight-through muons: 0.36 MIP's. In the study, a Gaussian was it to the lower edge of the muon response peak.

The catastrophic loss is smeared by a Gaussian based on the resolution found for test beam electrons: $0.6 \times \sqrt{dE}$ [Sak90]. Unfortunately, the test beam electrons were 25 and 50 GeV. Thus, it is not clear how applicable this is to $E < 1\ GeV$ deep muon showers.

Within the Shower Region

This is a simple function of the length of the shower and a rough estimate of the total muon energy, which should match the average true energy loss.

$$R_{MIP} = 0.92546 + 0.02418\ \log(E_\mu) \tag{5.11}$$

E_μ has a minimum of 0.1 in this equation. It was written by Carlos Arroyo (dated 12/92).

5.6 Hadron Energy Smearing

The hadron energy calculations are even more different than the muon energy calculations. The neutral current hadron energies are handled more or less the same (see below), but the charged current definitions are significantly different:

$$E^{CC}_{HAD}(1) = E^{NC}_{HAD} + E_{\mu}(smr) \mid^{PLACE}_{SHEND-5} - E_{\mu}(par) \mid^{PLACE}_{SHEND-5} \tag{5.12}$$

Here E^{NC}_{HAD} is the smeared hadronic energy, which would be the result for a neutral current event. $E_{\mu}(smr)$ is the simulated added response from the muon energy deposited in the shower region. $E_{\mu}(par)$ is a parameterized muon track through the shower region which is subtracted from the total in both data and MC.

In the data, for a charged current event, $(E^{NC}_{HAD} + E_{\mu}(smr))$ represents the sum of the map correct pulse heights ($TMAPLO$) times the hadron calibration constant. In PHDST is represented by the array EHNC.

There is also a variable EHCC which contains a parametrized muon subtraction, EMUCORR, which is described with the MC routines.

Hadronic Component

In the Monte Carlos, hadron smearing is based on a simple function of energy taken from the test beam. The result of this is also the smeared hadron energy for a Neutral Current event.

$$E^{NC}_{HAD} = E^{True}_{HAD} \times R(Poisson) \tag{5.13}$$

$$R(Poisson): \begin{cases} \sigma = 0.8767 & E_{HAD} < 1 \\ \sigma = 0.0297\ E + 0.847\sqrt{E} & 1 < E_{HAD} < 10 \\ \sigma = 0.297\ E + 0.847\sqrt{E} & E_{HAD} > 10 \end{cases} \tag{5.14}$$

Simulated Muon Response

The hadronic energy has added to it a term corresponding to the pulse heights from the muon. These are simply $E^{ctr}(res)$ and $E^{ctr}(cat)$ exactly as described in the muon energy smearing in the previous section. They are both converted to GeV using the hadron calibration constant.

As of the latest update, both the Old MC and NUMONTE use the same parameterized subtraction as the Data. In the data, this is described by the function "`dmudx1.f`". In the MCs, this is handled by a function called "`emuloss.f`". The function itself is described below:

$$E_\mu^{CORR} = \sum_{all\ \mu's} \sum_{PLACE}^{SHEND-5} (0.9315 + 0.02359\ \log E_i) \times C_{had} \tag{5.15}$$

$$E_i = \begin{cases} E_\mu^{FF} + \sum_i^{CEXIT} 0.159952 \cdot zlen & 8. < E_{est} < 450 \\ 8 & E_{est} < 8 \\ 450 & E_{est} > 450 \end{cases} \tag{5.16}$$

5.7 Simulated Cuts

Where possible, the cuts in the monte carlo are applied exactly as they are in the data, using the smeared MC variables in place of data quantities. However, certain cuts cannot be reproduced in the fast monte carlo. For these, it is assumed that the data cuts eliminate rare backgrounds which are not simulated in the Monte Carlo. Scanning of the data suggests that these cuts are highly efficient.

1. RUN+IGATE, NSTIME
   The bad data runs are ignored and do not require simulation. The fast monte carlo does not simulate non-neutrino events, which the IGATE and NSTIME cuts are largely designed to eliminate. These cuts appear to be 100% efficient, so no simulation is necessary.

   Overlay events do exist where a cosmic ray overlaps with a neutrino event, but these are extremely rare and are handled by specialized searches.

2. TARGET TRK, TOROID TRK, GOOD FIT, CHI/DF The fast monte carlo does not simulate the individual hits and fitting procedure of the data. Thus, it cannot check for the quality of fitting. It is assumed that if a muon track goes through good regions (as defined by other cuts), then it is well measured.

   This is confirmed by the extremely low percentage of events which are eliminated solely by these cuts (see Table 4.3). The few data events which are cut generally represent pathological cases which are not simulated in the Monte Carlo.

Other cuts are simulated somewhat more roughly than the exact calculation in the data. These are simulated, but somewhat more roughly than they are in the data.

1. TRIGGER 1, TWO GAPS In the fast monte carlo, it is assumed that if a muon passes through the first toroid gap (T2) then trigger-1 is always set and that there are no false triggers. Since there are three sets of overlapping trigger counters, this is a solid and well-understood assumption.

   It is also assumed that the tracking will always properly identify if a muon passes through the second gap (T3). This has been studied in general toroid tracking and is also well understood.

2. DIMUON In the data, identifying a dimuon event is a complex function of the efficiency of finding a muon. In the monte carlo, it is assumed that if a second muon must pass through 8 drift chambers before exiting before it is identified as a separate track.

Chapter 6

Physical Models

The monte carlo simulation depends on a set of assumed physical models. The basic physics within the detector has already been covered in Chapters 4 and 5. However, there are two basic inputs: the flux of neutrinos, and the cross-section of neutrinos.

These inputs are based on our data, given certain basic assumptions. First of all, we do not measure the absolute level of neutrino cross-section at all – that is taken from earlier experiments. Second, it is assumed (in the monte carlo) that the neutrino cross-section is linear with energy. Third, we assume the V-A structure of the neutrino cross-section, which allows the cross-section to vary only within the three structure functions: xF_1, F_2, and xF_3.

6.1 Iteration Procedure

Clearly the flux measurement and the cross-section measurement overlap heavily. The flux is purely a function of E_ν, while the cross-section is treated as strictly linear in E_ν. However, a variance in the cross-section model will produce a different extracted flux.

This was solved by using an iterative approach as follows:

1. Assume a flux ϕ_{EST} and a cross-section function q_{EST}
2. Generate Monte Carlo events using ϕ_{EST} and q_{EST}
3. Apply resolution smearing to the simulated events
4. Use the Monte Carlo events to correct the low-E_{HAD} events and extract a flux σ_{NEW} (described in Section 6.3)
5. Re-weight the Monte Carlo events to reflect the new flux and again apply resolution smearing
6. Use the re-weighted Monte Carlo events to extract a set of structure functions F_{NEW}

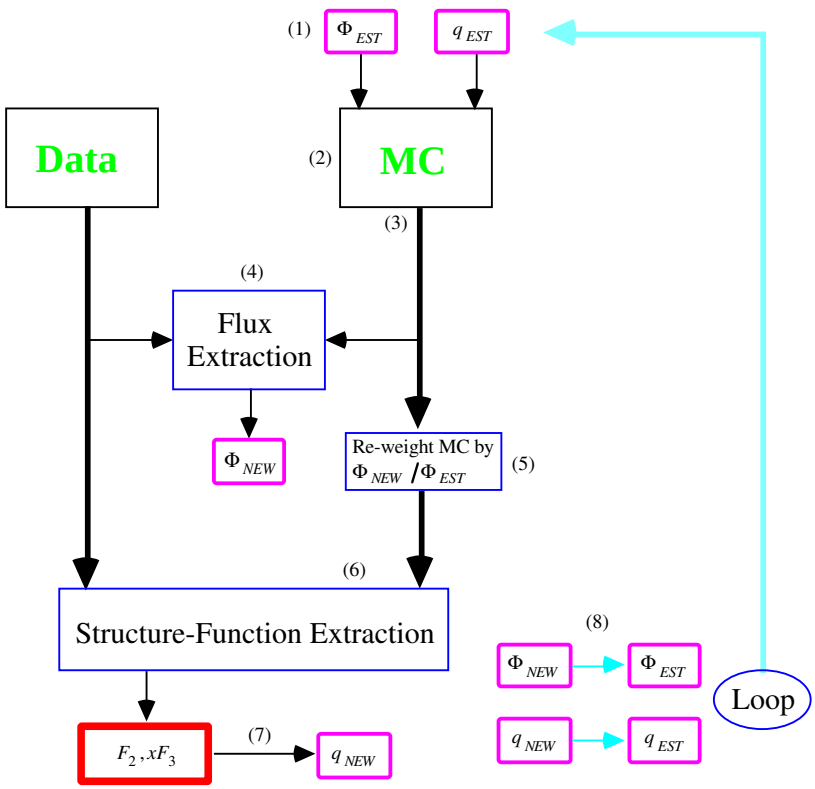

Figure 6.1: Flowchart of the iterative analysis procedure.

7. Fit parton distribution functions to the structure functions F_{NEW}, using the Buras-Gaemers method described in Section 6.2. This makes a new cross-section function, q_{NEW}.

8. Use the new flux ϕ_{NEW} and cross-section q_{NEW}, and repeat steps (1) through (7) until the difference from the previous iteration is small.

In practice, the results converge after three iterations of this procedure. This is shown diagrammatically in Figure 6.1. Note that with any iterative procedure, there is a danger of finding a local minima. This would represent a set of flux and structure functions which are consistent, but not the best (most likely) solution. However, the structure functions extracted were robust with numerous minor changes in the analysis. This was specifically checked for by varying the form of the cross-section parameterization, described in the next section.

6.2 Cross-section and Buras Gaemers Fitting

The fixed theoretical input to all aspects of the analysis is the neutrino cross-section model. It is used to extract the neutrino flux from the low-hadron-energy data, and then used again in the determination of corrections based on detector acceptance. Finally, it is used to apply phenomenological corrections for isoscalarity, target mass, radiative corrections, charm production thresholds, and propagator corrections.

The basic cross-section is the standard V-A form outlined in the Introduction:

$$\frac{d^2\sigma}{dxdy} = \frac{G^2ME}{\pi}\left[(1-y-\frac{Mxy}{2E})F_2(x,Q^2)+\frac{y^2}{2}2xF_1(x,Q^2)\pm(1-\frac{y}{2})xF_3(x,Q^2)\right] \quad (6.1)$$

Here the $\pm$ represents the neutrino $(+)$ and anti-neutrino $(-)$ cross-sections, respectively. The functions F_2, $2xF_1$, and xF_3 are required inputs to this calculation. Ideally, we would require a smooth function which will describe the CCFR data over the full range of x and Q^2. It also needs to extrapolate reasonably to beyond our visible kinematic range, to properly calculate the effect of outside events which are smeared into our region. The parameterization should allow for QCD scaling, but should not be restricted to QCD values or else we would be pre-supposing the point we are measuring. The fit should have a relatively small number of parameters so that it is assured of finding a unique solution. Finally, it should have a minimum of calculation so that it can be used in the 'fast' monte carlo.

This is no small task. The basics of the method used is taken from the work of A.J. Buras and K.J.F. Gaemers [Bur78]. They suggested a leading order calculation in QCD, using 13 parameters to simply describe the known structure functions at that time. The new fit used by CCFR adds some terms which allow it to vary from a strict leading order calculation, while also simplifying to eliminate some parameters which are not important for our purposes.

In qualitative terms, there are two basic behaviors to describe. *Valence* quarks, at the simplest level, should each carry on average 1/3 of the momentum of the nucleon ($x = \frac{1}{3}$), while their motion within the nucleon varies x around this center. In other words, we roughly expect a distribution peaked at ($x = \frac{1}{3}$), and going to zero at ($x = 0$) and ($x = 1$). *Sea* quarks should be negligible for ($x > 0.3$) but dominant for ($x < 0.1$). Thus we expect a rising but not asymptotic function as $x \to 0$.

The model used (known as BGPAR) is equivalent to a leading order model in QCD, but is intended as a simple phenomenological fit which should not depend on specifics of QCD. It is used only for detector acceptance corrections, and should not be relied upon for accurate QCD results. As NUMONTE is a "fast" Monte Carlo, the usefulness of this model is the minimum number of calculations it uses. In the future, a next-to-leading order model would be a useful check of the effect of this.

Quark Parton Distributions

The Buras-Gaemers method works by returning distributions to leading order. At leading order, the distribution of quarks can be broken up into four categories:

U-valence was characterized in Buras-Gaemers with a form of $(x^{\eta_1}(1-x)^{\eta_2})$. This fulfills basic expectations of the distribution. Also, according to their article it turned out to match the leading-order QCD scaling for the first 12 moments to within 2%.

D-valence: was fitted separately by Buras and Gaemers. However, the CCFR neutrino data is insensitive to the distinction between up and down. Overall, two-thirds of the valence distribution should be up quarks, and one third should be down quarks. However, the U-quarks are more affected by the Fermi Exclusion Principle. This means that if one U-quark is sitting at a lower momentum, then the other cannot be in the same quantum state and thus will tend to a higher momentum. This means that the U-quark distribution will have a higher average x than the D-quark distribution.

Sea: This represents U-Ubar and D-Dbar pairs, which are assumed to have the same behavior in x and Q^2.

Strange Sea: is similar to the Sea distribution, representing S-Sbar pairs of quarks. These are important because it is common for a neutrino event which strikes an S-quark (or Sbar) to push it to a charm quark. C-quarks have much greater mass than he others, and frequently decay into a high-energy muon.

This creates "dimuon" events where one muon comes out of the neutrino scattering, and a second muon comes from the decay of the charm quark. Luckily, these distinctive dimuon events can be used to precisely measure the Strange Sea [Rab92].

Charm Sea: is neglected in this model. Charm quarks are suppressed compared to the strange sea by their greater mass (a factor of about $\times 30$).

Gluons do not affect the neutrino cross-section at leading order, and are thus neglected in this model.

The object of this modeling, then, was to fit our data with a minimal number of parameters. We have two basic functions: one for the Valence and one for the Sea. We choose a rough form for how the function behaves in x, and then a set of rules for how that function evolves in Q^2. The final model used has twenty free parameters.

The structure functions at leading-order are derived from these quark parton distributions by:

$$2xF_1 = U_V + D_V + SEA\left(\frac{2}{F_S+2}\right) + SSEA\left(\frac{F_S}{F_S+2}\right) \tag{6.2}$$

$$F_2 = 2xF_1\left(\frac{1+R(x,Q^2)}{1+2(M_p\ x)^2/Q^2}\right) \tag{6.3}$$

$$xF_3 = U_V + D_V \tag{6.4}$$

Here $R(x,Q^2)$ is the longitudinal structure function. Its value is taken from a parameterization by Whitlow [Whi90], which defines the relation of $2xF_1$ and F_2. F_S is a factor for the strangeness of the quark sea, defined as the fraction $(s+\bar{s})/(\bar{u},\bar{d})$. The precise strange sea shape is taken from dimuon data, but in this small correction term, we assume a fixed fraction ($F_S = 0.37$) due to ease of calculation.

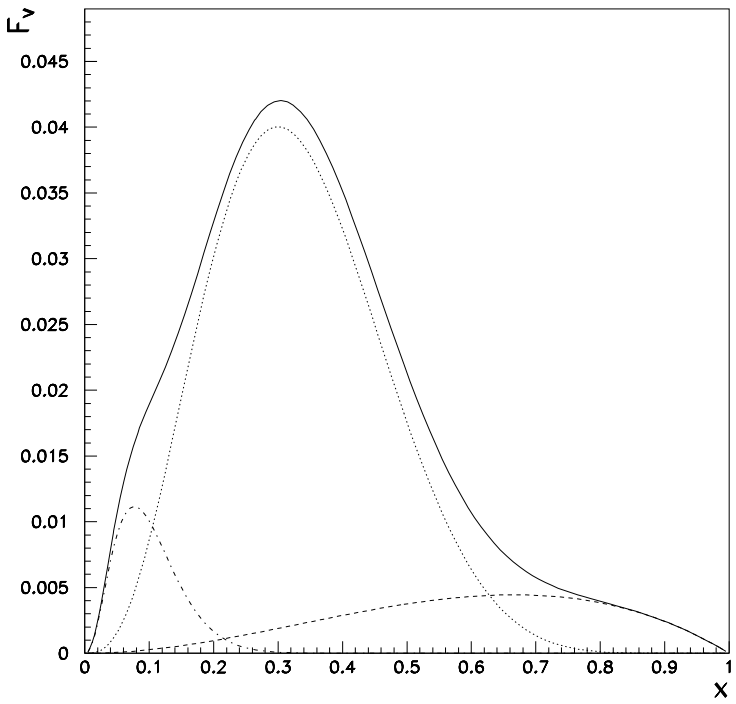

Figure 6.2: Conceptual diagram of the valence quark function in x. The solid line shows the total function. The dashed lines show the contribution of the three terms as shown in Equation 6.5, which allow varying behavior in different regions of x.

Choice of Functions in x

Our choice of the functional form within x is semi-arbitrary, based on the rough expected behavior outlined above and tuned to give a good fit to our data. The term $x^E(1-x)^{E'}$ was analyzed in-depth by Buras and Gaemers, so that was the basis for the general function. The shape in x is defined first for a central value of Q^2, chosen to be ($Q_0^2 = 12.6\ GeV^2$).

$$F_V(Q_0^2) = \left[X^{E_1}(1-x)^{E_2} + AV2 * x^{E_3}(1-x)^{E_4} + AV3 * x^{E_5}(1-x)^{E_6}\right] \quad (6.5)$$

$$U_V = U_{TOT} \times F_V \quad (6.6)$$

$$D_V = D_{TOT} \times F_V \times (1-x) \quad (6.7)$$

$$SEA = AS(1-x)^{ES} + AS_2(1-x)^{ES_2} \quad (6.8)$$

The three terms in the general shape F_V allow for varying characterizations of high-x, medium-x, and low-x regions – while still satisfying going to zero both at $x = 0$ and at $x = 1$. The down-quark portion of the valence will have a lower average x, and neutrino scattering is relatively insensitive to

Parameter	Description	Value
A_0	Lambda	0.661945
A_1	LO Valence Normalization	0.384862
A_2	NLO Valence Normalization	-0.283013
E_1^0	1st Valence term x exponent at Q_0^2	0.578665
E_1^1	Valence x exponents' slope in Q^2	0.030720
E_2^0	1st Valence term $(1-x)$ exponent at Q_0^2	2.747293
E_2^1	Valence $(1-x)$ exponents' slope in Q^2	1.458975
AV_2	2nd Valence term constant	28.31528
E_3^0	2nd Valence term x exponent at Q_0^2	2.964218
E_4^0	2nd Valence term $(1-x)$ exponent at Q_0^2	9.140378
AV_3	3rd Valence term constant	19.41696
E_5^0	2nd Valence term x exponent at Q_0^2	2.042780
E_6^0	2nd Valence term $(1-x)$ exponent at Q_0^2	30.68763
S_2	Total Sea 2nd moment in x at Q_0^2	0.147449
S_3	Total Sea 3rd moment in x at Q_0^2	0.0152760
G_3	Gluon 3rd moment in x at Q_0^2	0.0513642
AS_2^0	2nd SEA term constant at Q_0^2	0.407077
AS_2^1	2nd SEA term constant slope in Q^2	0.121723
ES_2^0	2nd SEA term $(1-x)$ exponent at Q_0^2	64.43626
ES_2^1	2nd SEA term $(1-x)$ exponent slope in Q^2	0.0514954

Table 6.1: The final parameters for the best BGPAR fit, with qualitative description for each parameter. The χ^2/DOF for this fit was 287/236.

U_V versus D_V difference. Thus, we assume a factor of $(1-x)$, which was the approximate relation between the two in the original Buras-Gaemers article.

The function for sea quarks is similarly chosen based on the simple requirement of a rising function as $x \to 0$. The original Buras-Gaemers article has a single term $((1-x)^E S)$. The additional term allows greater freedom of variation in x.

Scaling in Q^2

These function are evolved in Q^2 using functional forms similar to QCD, but we do not require the parameters to match any exact QCD calculation. This is done first because we only expect our model to work roughly within our range of x and Q^2. In particular, we expect deviations at very low x which may throw off the fit. Second, assuming QCD-based calculations in our extraction of structure functions could bias our results.

1. The total normalization of the valence partons are required to scale to a variant of the GLS sum rule. This uses an identical functional form, but avoids QCD-calculated parameters as described above. Instead, the parameters are allowed to freely vary to fit the CCFR data. Further, it is assumed that the sum for D_V is half of the sum of U_V.

$$A_{TOT} = `GLS' = 3\left(1 - \frac{A1}{log(Q^2/A_0^2)} - \frac{A2}{\left[log(Q^2/A_0^2)\right]^2}\right) \quad (6.9)$$

$$\int_0^1 (U_V)dx = U_{TOT}\int_0^1 (F_V)dx = \frac{2}{3}A_{TOT} \quad (6.10)$$

$$\int_0^1 (D_V)dx = D_{TOT}\int_0^1 (F_V)(1-x)dx = \frac{1}{3}A_{TOT} \quad (6.11)$$

where here F_V is the valence function in x defined earlier. Note that A_0 here takes the place of λ in QCD.

2. The behavior of the valence distribution in x uses the same function as in the original Buras-Gaemers article. There they claim this approximates the QCD scaling to within 10% for the first twelve moments.

$$F_V(Q^2) = F_V(Q_0^2) \times x^{E_1^1 s}(1-x)^{E_2^1 s} \quad (6.12)$$

$$s = \log\left[\frac{\log(Q^2/A_0^2)}{\log(Q_0^2/A_0^2)}\right] \quad (6.13)$$

Here Q_0^2 is chosen to be approximately central to our range. The value $12.6GeV^2$ was the mean Q^2 of previous Fermilab experiments E616/E701. Note that there is no rigorous assurance that this dependence matches QCD beyond the vague statement in the original Buras-Gaemers paper (which referred to their one-term valence function). However, this function is not used for any QCD-based extraction and is a good fit to the data.

3. The behavior of the sea quark in Q^2 is controlled in terms of their second and third moments in x, defined by $\int x(SEA)dx$ and $\int x^2(SEA)dx$. These moments are constrained by QCD-like functions, but again allowing the values to float. This constraint comes from three basic parameters: S_2, S_3, and G_3.

$$\int_0^1 x(SEA)dx = \frac{3}{4}D_{2,2}(S_2,Q^2) + \frac{1}{4}D_{1,2}(S_2,Q^2) \quad (6.14)$$

$$\int_0^1 x^2(SEA)dx = \frac{3}{4}D_{2,3}(S_3,G_3,Q^2) + \frac{1}{4}D_{1,3}(S_3,Q^2) \quad (6.15)$$

The functional form for $D_{2,N}$ can be found in [Bur78]. Note that there are only two constraints here on the shape in x, while there are four free parameters in x at Q_0^2 (Equation 6.8). The remaining parameters AS_2 and ES_2 are constrained to be linear in the log of Q^2. Thus, we have:

$$AS_2 = AS_2^0 + AS_2^1\ \log(Q^2) \quad (6.16)$$

$$ES_2 = ES_2^0 + ES_2^1\ \log(Q^2) \quad (6.17)$$

This is a semi-arbitrary choice for the behavior in Q^2, but since the overall moments including both terms are constrained, this can only deviate from QCD-like behavior via the fourth moment in x.

Parameter	Description	Value
A_0	Lambda	0.447670
A_1	LO Valence Normalization	0.662974
E_1^0	1st Valence term x exponent at Q_0^2	0.714670
E_1^1	Valence x exponents' slope in Q^2	-0.0607994
E_2^0	1st Valence term $(1-x)$ exponent at Q_0^2	3.26255
E_2^1	Valence $(1-x)$ exponents' slope in Q^2	1.77715
AV_2	2nd Valence term constant	0.0435841
E_3^0	2nd Valence term x exponent at Q_0^2	2.98967
E_4^0	2nd Valence term $(1-x)$ exponent at Q_0^2	1.19919
S_2	Total Sea 2nd moment in x at Q_0^2	0.142764
S_3	Total Sea 3rd moment in x at Q_0^2	0.0135942
G_3	Gluon 3rd moment in x at Q_0^2	0.0448591
S_4	Total Sea 4th moment in x at Q_0^2	0.00267237
G_4	Gluon 4th moment in x at Q_0^2	0.01
ES_2	2nd SEA term $(1-x)$ exponent	60.07506

Table 6.2: The final parameters for the alternate BGPAR fit, used as a check of the systematic uncertainty due to model choice. This has reduced parameters and increased QCD restrictions. The χ^2/DOF for this fit was 336/242.

The final values for each of the parameters in the best fit are given in Table 6.1. These are the values found after iteration.

Systematic Error

The systematic error was treated by iterating using a significantly varied functional form which had a similar (although slightly worse) χ^2. The primary model described has 21 parameters. In practice, it was found that the number of parameters could be reduced without greatly increasing the χ^2. However, in order to accurately test the dependence of our results on the form, the form would have to be significantly changed. The following changes were made to the previously described fit:

- The value of A_2 was fixed to the best-fit value. This had almost no effect on the results.
- The third term in the valence was dropped. This is equivalent to setting $AV_3 = 0$, and removes three parameters. This caused only a small rise in χ^2, but changed the shape noticably.
- An additional QCD constraint was put on the Q^2 scaling of the sea quark function. The fourth moment of the sea was constrained to QCD-like behavior. This constraint is exactly parallel to the constraints on the second and third moments described earlier. Thus, four parameters of the best fit (AS_2^0, AS_2^1, ES_2^0, ES_2^1) were replaced by two parameters of the alternate fit, S_4

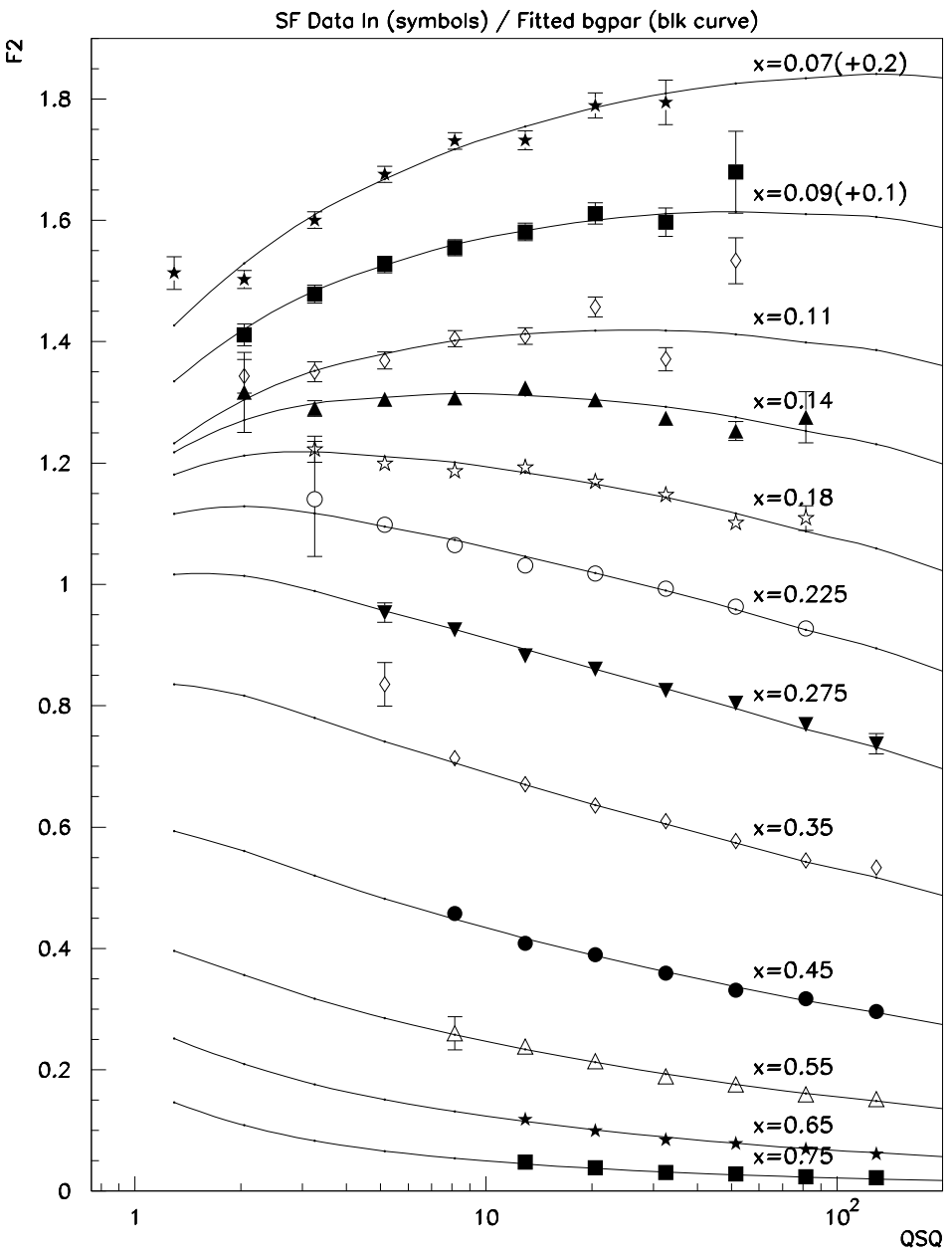

Figure 6.3: Extracted F_2 data and best BGPAR fit for $x > 0.06$.

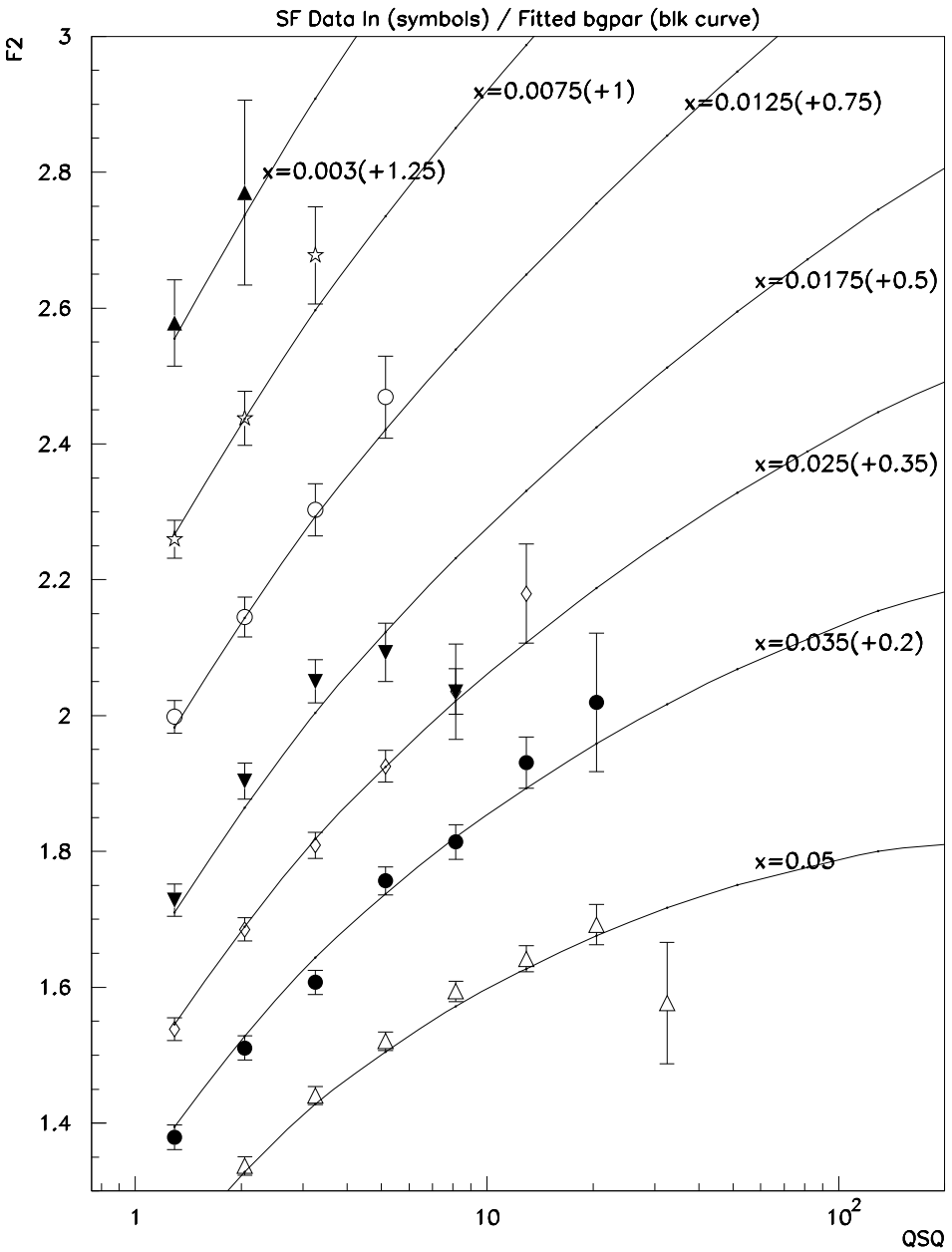

Figure 6.4: Extracted F_2 data and best BGPAR fit for $x < 0.06$.

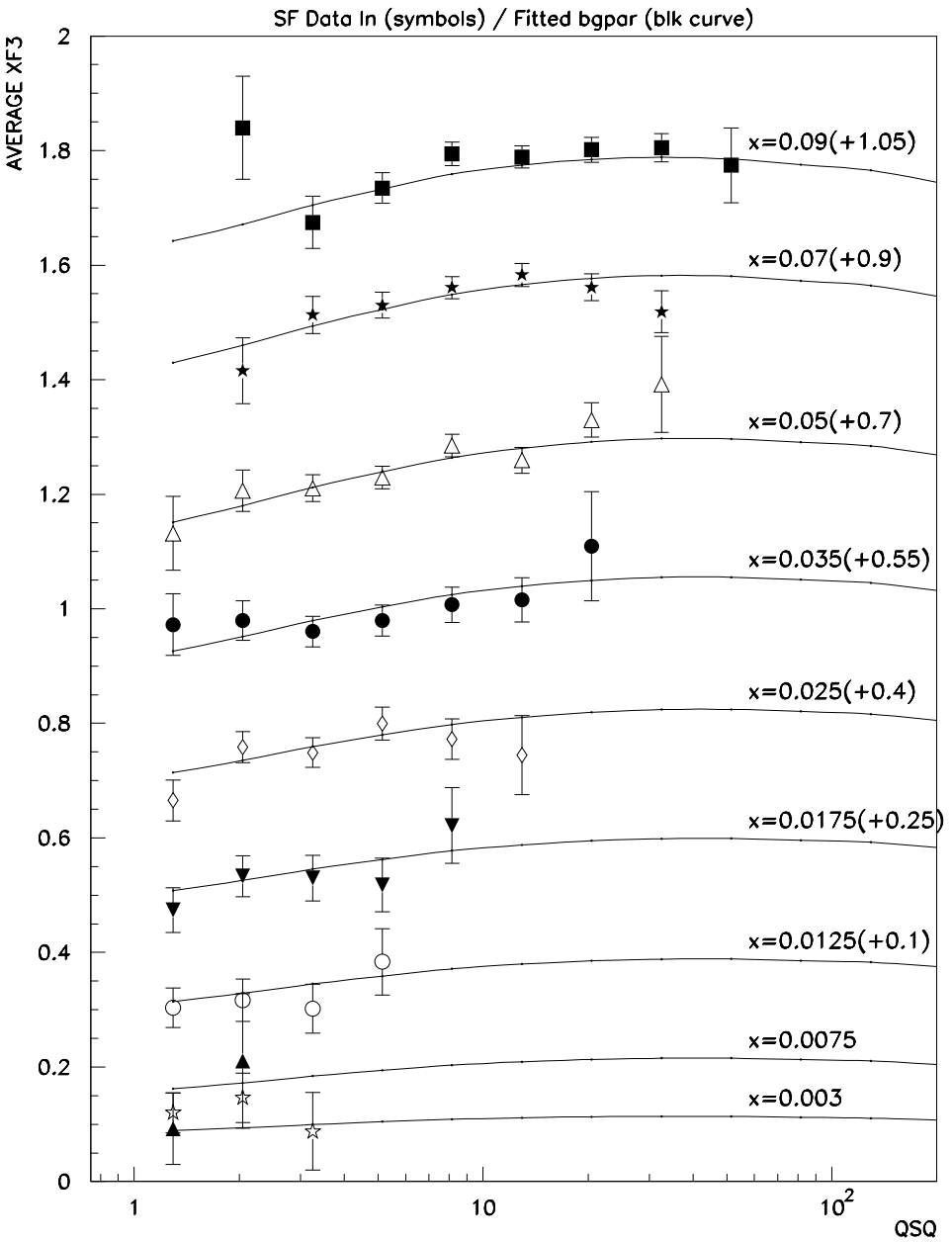

Figure 6.5: Extracted xF_3 data and best BGPAR fit for $x < 0.1$.

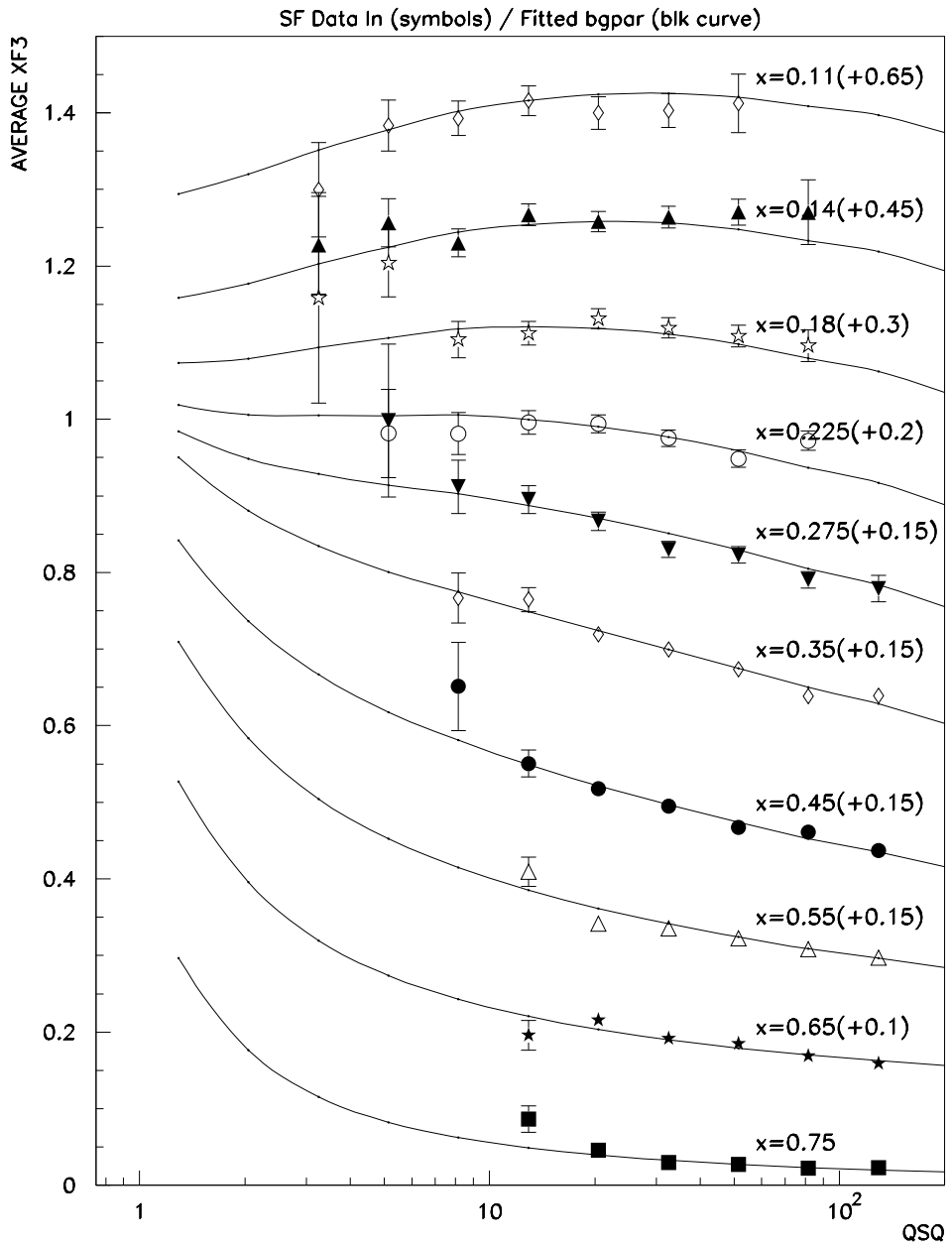

Figure 6.6: Extracted xF_3 data and best BGPAR fit for $x > 0.1$.

and G_4. These constrained the fourth moment as:

$$\int_0^1 x^3(SEA)dx \quad = \quad \frac{3}{4}D_{2,4}(S_4, G_4, Q^2) + \frac{1}{4}D_{1,4}(S_4, Q^2) \tag{6.18}$$

This constraint caused a significant jump in the χ^2 of the fit. However, a significant change in the shape of the function is bound to cause some disagreement.

The final parameters along with the resulting χ^2 of the fit are shown in Table 6.2. This alternate fit uses a significantly different functional form, while still giving a good fit. It constrains the parameterization to use less parameters and approximate QCD more closely. By iterating separately using this parameterization, an alternate SF data set was formed. The alternate SF set is used as an estimate of the systematic error due to the choice of acceptance model.

Previous Models

Various forms of the BGPAR parameterization have been used in many earlier analyses of CCFR data. These generally had only 8 or 9 parameters, and their total χ^2 was of order $500/332 DOF$ or greater. The parameterization used for the central value in the previously published structure functions [Sel97] was:

- Only the first term of the valence function was used, equivalent to setting AV_2 and AV_3 to zero.
- The valence normalization was accomplished with only two parameters (A_0 and A_1), which had a different meaning than the A parameters described here. The normalization condition was:

  $$\int_0^1 (U_V + D_V)dx = 3A_1 \left(1 - \frac{4/(11 - \frac{8}{3})}{log(Q^2/A_0^2)}\right) \tag{6.19}$$

  Note that the leading term of this is allowed to vary from 3 even at asymptotic Q^2 as $\alpha_S \to 0$, which is not allowed in the QCD or parton models.
- Only a single term of the sea function was used, equivalent to setting $AS_2 = 0$. Thus, only 3 parameters were needed for the sea distribution (S_2, S_3, G_3), compared to 7 in the full fit and 5 in the reduced-parameter fit. These constrained the moments in exactly the same way as the primary fit described here.

The fit using this parameterization has a larger χ^2 than the fit used for the GLS. However, this was covered by a larger model systematic error. The systematic error was estimated by using yet another parameterization (suggested by C. McNulty) which added a small term to the valence function of $(1-x)_i^E$. This meant that the parameterization did not go to zero as $x \to 0$. The fit did produce a better χ^2 but did not have an established theoretical basis. While large for the GLS, this error was minor for the global fits which do not have a strong dependence on low x.

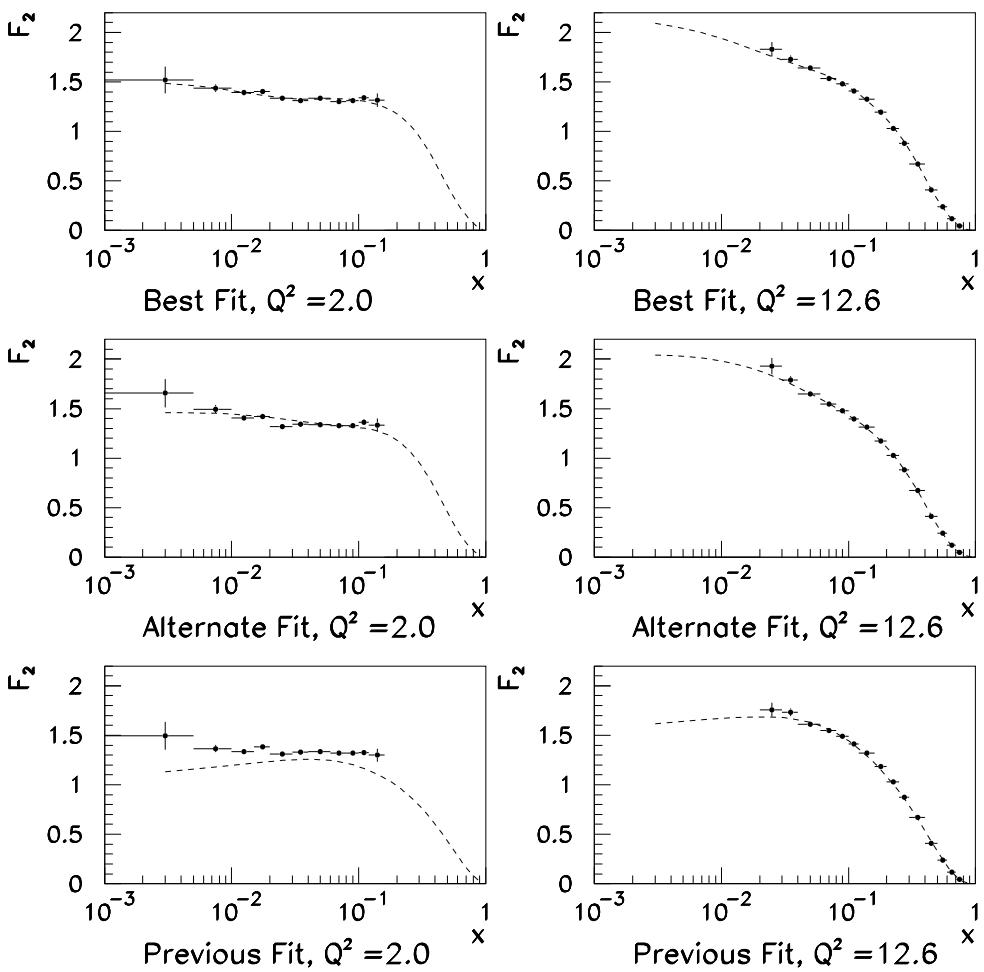

Figure 6.7: Comparison of different BGPAR fits on F_2 vs x, for two Q^2 bins. The top is the best fit; the middle is the alternate fit used as a systematic error; the bottom is the previous fit. Note the divergence at low Q^2 and hence low x.

Fit	Filename	# of Parameters	χ^2/DOF
Best	`QTB581-jhk`	20	287/236
Model Error	`QTB585-jhk2`	14	336/242
Previous	`ccfr-base`	9	572/247

Table 6.3: The χ^2/DOF for each BGPAR fit.

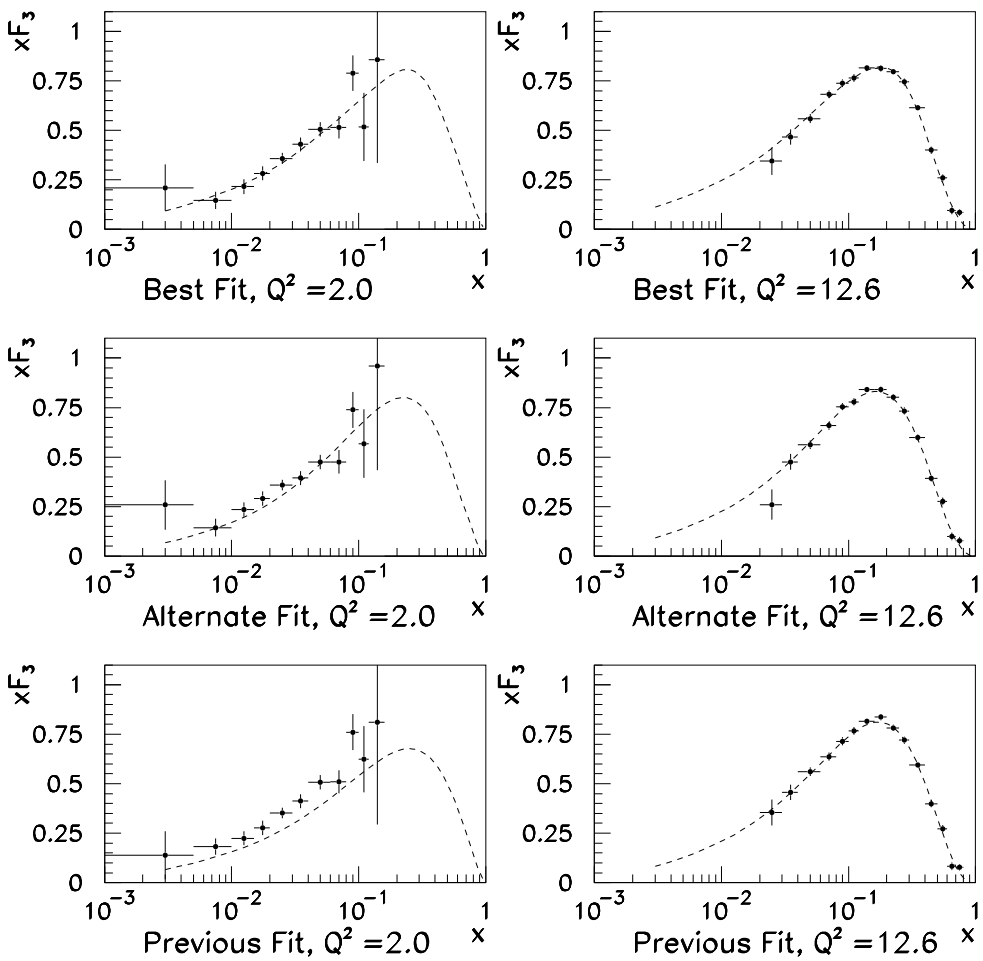

Figure 6.8: Comparison of different BGPAR fits on xF_3 vs x, for two Q^2 bins. The top is the best fit; the middle is the alternate fit used as a systematic error; the bottom is the previous fit. Note the divergence at low Q^2 and hence low x.

6.3 Flux Extraction Procedure

A neutrino beam cannot be monitored directly, and in this experiment the secondary meson beam that produced the neutrino beam was too intense for monitoring as well. Therefore, the flux of neutrinos and anti-neutrinos had to be determined from the number of interactions in the detector itself, using a low-hadron-energy sample of the data.

The method employed is called the fixed-E_{HAD} method, or the fixed-ν method ($\nu = yE_\nu = E_{HAD}$. This provides a measurement off the *relative* flux of neutrinos and anti-neutrinos between energy bins. The *absolute* incident lepton flux is found by normalizing the measured total neutrino cross section for $E_\nu < 230\ GeV$ to the world average:

$$\sigma^{\nu N} = (0.676 \pm .014) \times 10^{-38} cm^2 E_\nu \tag{6.20}$$

The general formula for the differential cross-section with respect to E_{HAD} is obtained by integrating the structure functions over all x as follows:

$$\frac{d\sigma}{dE_{HAD}} = \frac{G^2 M}{\pi} \int dx F_2 \left[1 - y \left(1 \mp \frac{\int xF_3}{\int F_2} \right) + \frac{y^2}{2} \left(1 \mp \frac{\int xF_3}{\int F_2} + \int \tilde{R} \right) \right] \tag{6.21}$$

$$\tilde{R} = \frac{E_{HAD} + 2Mx}{(1+R)E_{HAD}} - \frac{Mx}{E_{HAD}} - 1 \tag{6.22}$$

where here xF_3, F_2, and R are the singlet, non-singlet, and longitudinal structure functions, respectively. The leading term of the differential cross section with respect to E_{HAD} is a constant, and E_{HAD}-dependent corrections are of order (E_0/E_ν) and $(E_0/E_\nu)^2$.

The number of events with $E_{HAD} < E_0$ is found by integrating this differential from zero to E_0, resulting in an expression for the *flux*:

$$N(E, E_{HAD} < E_0) = \phi(E_\nu) \frac{G^2 M}{\pi} \int dx F_2 E_0 \left[1 - \frac{E_0}{2E} \left(1 \mp \frac{\int xF_3}{\int F_2} \right) + \frac{E_0^2}{6E^2} \left(1 \mp \frac{\int xF_3}{\int F_2} + \int R(x, Q^2) \right) \right] \tag{6.23}$$

The value of $R(x, Q^2) = \sigma_L / \sigma_T$ used comes from an empirical parameterization of the world's available data on R [Whi90]. The formula used is:

$$R = \frac{0.0635}{s}\theta + \frac{0.5747}{Q^2} - \frac{0.3534}{Q^4 + 0.09} \tag{6.24}$$

$$\theta = 1 + \frac{12Q^2}{Q^2+1} \times \frac{c^2}{c^2 + x^2} \tag{6.25}$$

where $s = \ln(Q^2/0.04)$, and $c = 0.125$. At the time that Ref [Whi90] was published, the world's available data on R was restricted to the region $x > 0.1$ and $Q^2 < 75\ GeV^2$. For this analysis, it is assumed that the data is good over the full kinematic region of the CCFR data.

The corrections that depend on $(\int xF_3 / \int F_2)$ are determined by fitting the low E_{HAD} data to a quadratic polynomial of the form:

$$\frac{dN}{dE_{HAD}} = \phi(E_\nu) \left(A + By + C(\frac{y^2}{2}) \right) \tag{6.26}$$

$$A(E) = \frac{G^2 M}{\pi} \int F_2 \phi(E_\nu) \tag{6.27}$$

$$B(E) = -\frac{G^2 M}{\pi} \int F_2 left(1 - \frac{\int xF_3}{\int F_2} right) \phi(E_\nu) \tag{6.28}$$

$$C(E) = B + A \int \tilde{R} \tag{6.29}$$

The ratio of coefficients determines the ratio of integrated structure functions:

$$\frac{B}{A} = -\left(1 \mp \frac{\int xF_3}{\int F_2}\right) \tag{6.30}$$

Whereas the structure functions depend on $Q^2 = 2ME_{HAD}$, imposing a fixed-E_{HAD} cut means that the same Q^2 range is used at all energies, and therefore B/A is approximately constant with energy. The average of B/A from fits in all energy bins determines $< B/A >$ to high precision. Using these coefficients, the relative flux is:

$$\phi(E_\nu) = \int_0^{E_0} \frac{(dN/dE_{HAD})}{\left[1 + y(< \frac{B}{A} >) - \frac{1}{2} y^2 (< \frac{B}{A} > - \int F_2 \tilde{R} / \int F_2)\right]} \, dE_{HAD} \tag{6.31}$$

The fixed-E_{HAD} cut is chosen at ($E_0 = 20\ GeV$), to ensure sufficient numbers of events in the high energy bins. Other data quality cuts that are imposed are $E_\mu > 15\ GeV$ and $\theta_\mu < 0.15\ rad.$ A total of 407,000 neutrino and 140,000 antineutrino events are used for the flux extraction.

Values of B/A are shown in Figure 6.9, from fits to the $E_{HAD} < 20\ GeV$ data for experiment E744. The values do not show any energy dependence and the averages are $< B/A >_\nu = -0.266 \pm .05$ and $< B/A >_{\overline{\nu}} = -1.682 \pm .04$. The relative neutrino and antineutrino fluxes are show in Figure 6.10.

The flux extraction procedure includes corrections of the raw events for detector acceptance, smearing, and kinematic cuts by using a Monte Carlo simulation (which is described in Chapter 5). Through this Monte Carlo, the flux determination depends on the structure functions themselves. Therefore the flux determination and the structure function extraction are performed using a coupled procedure, which iterates the determinations until neither the flux nor the structure functions change with more iterations (i.e. they converge). The structure function extraction includes model corrections to account for the slight non-isoscalarity of the target, the effects of producing massive charm quarks, and for higher-order QED radiative effects.

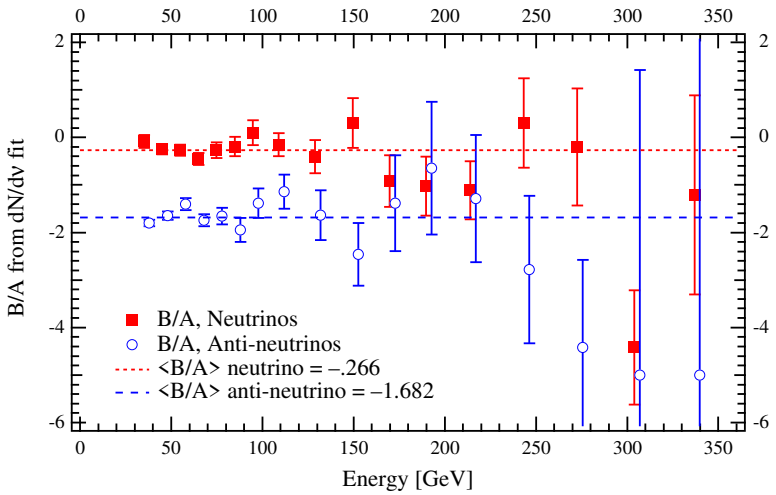

Figure 6.9: B/A as a function of energy for experiment E744. The two lines indicate the average B/A, derived from a fit to the points in the figure. The χ^2 of the fits were 25.0 (ν) and 18.4 ($\overline{\nu}$) for 16 degrees of freedom.

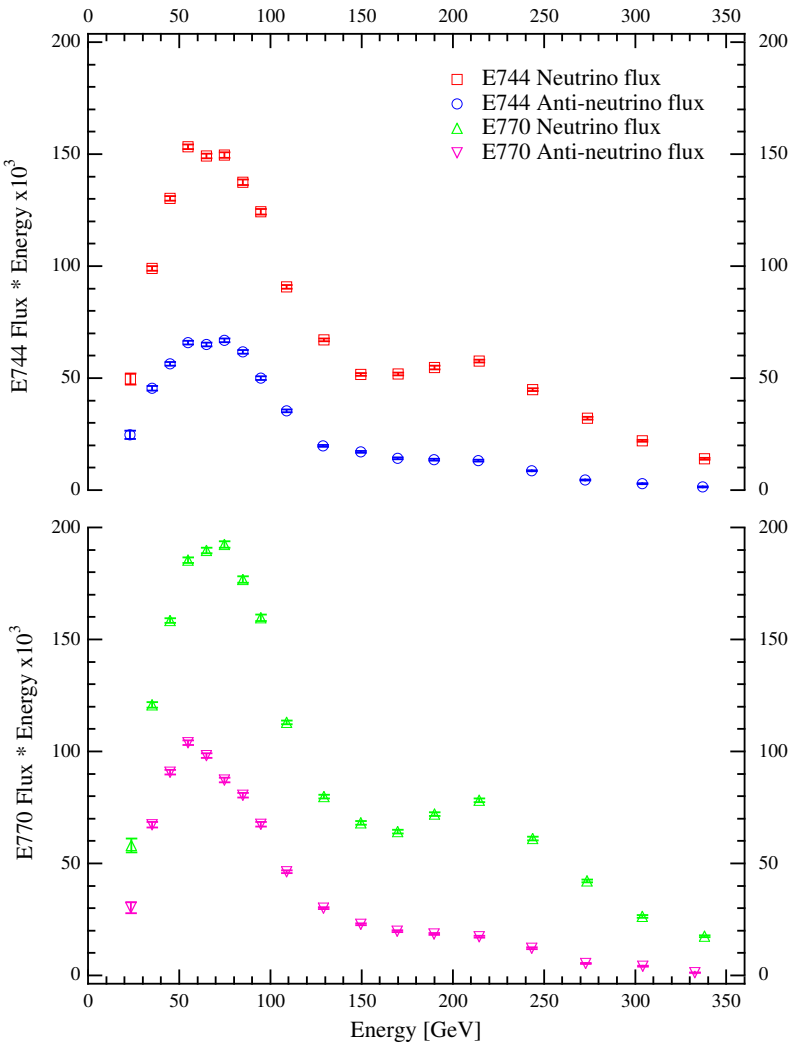

Figure 6.10: The fully corrected flux × energy spectra for E744 and E770. The normalization along the left axes is arbitrary.

Chapter 7

Integration of xF_3

The key to this measurement is developing an experimental measure of $\int (xF_3/x)dx$ with as few assumptions as possible. This is done first by evaluating the integral across x separately for each Q^2 bin. This eliminates any dependence on the scaling of xF_3 with Q^2, but it also means that we have to combine experiments to cover the full range of x.

Figure 7.1 shows the range of each experiment in x and Q^2. As you can see, at low Q^2 the CCFR data only covers the low end of the x range. The other experiments are necessary to cover the high-x range. After combining, we have 16-20 data points across a range of x for each Q^2 bin.

7.1 Data Handling

The GLS data points are combined from several experiments. Since the CCFR data is the most accurate, we read in other experiments and correct them to match with the parameters of the CCFR data.

In addition to CCFR, there are five $\nu - N$ experiments whose data is used in this result. These are generally bubble-chamber experiments with lower statistics than CCFR, but conducted at a lower neutrino energy which gives them a better window at high-x. The experiments used are listed below in chronological order.

BEBC-Gargamelle This is the combined data from the original BEBC and Gargamelle experiments, published in 1982. The Gargamelle data consists of 3000 ν and 2000 $\overline{\nu}$ events of $2 < E < 12\ GeV$ on freon (CF_3Br). The BEBC data consists of 3100 ν and 1120 $\overline{\nu}$ events of $5 < E < 210\ GeV$ on a neon-hydrogen mixture (74% molar Ne). [Amm78]

FNAL-E180 This is data from the E180 experiment at Fermilab, published in 1982. The data consists of 1202 ν and 7197 $\overline{\nu}$ events of $10 < E_\nu < 200\ GeV$ on a neon-hydrogen mixture (64% molar Ne). [Amm82]

WA25 This is data from a later experiment using the BEBC bubble chamber at CERN, published

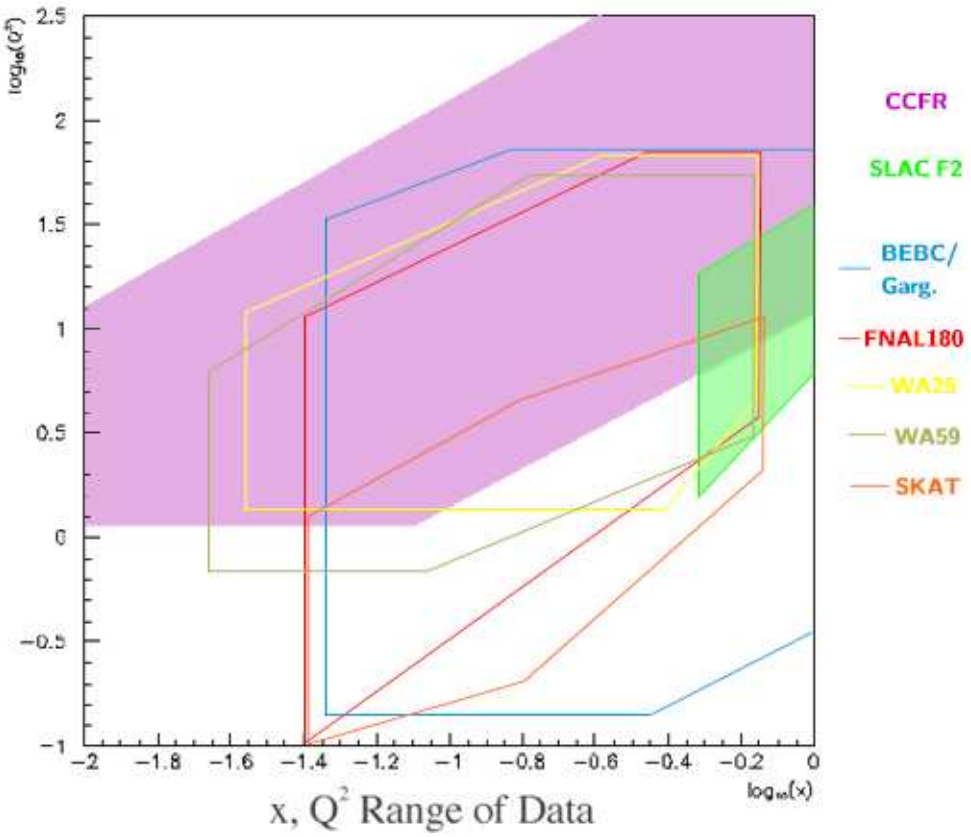

Figure 7.1: The range of each experiment in x and Q^2.

in 1985. The data consists of 15405 ν and 13793 $\overline{\nu}$ events of $10 < E < 200\ GeV$ on deuterium. [All85]

SKAT This is the data from the SKAT collaboration at IHEP Serpukhov in the USSR, published in 1986. The data consists of 4250 ν and 650 $\overline{\nu}$ events of $3 < E < 40\ GeV$ on freon (CF_3Br). [Amm86]

WA59 This is data from a later experiment using the BEBC bubble chamber at CERN, published in 1987. The data consists of 8141 ν and 13334 $\overline{\nu}$ events of $10 < E < 200\ GeV$ on a neon-hydrogen mixture (75% mole Ne). [Var87]

The bubble-chamber experiments have significantly different procedures from the CCFR detector. However, the systematic errors are minor compared to the statistical limit. Systematic differences between the experiments are corrected for by normalization (see below).

Combining Experiments

The other experiments are subjected to three small corrections to combine them with CCFR data. First of all, the xF_3 data is generally given by a set of values, each at the center of the bin in x and Q^2 – where the binning scheme is different than CCFR. To combine these, we simply find the closest CCFR bin center and shift it using the BGPAR fit (see Section 6.4).

This procedure does result in an unevenness to the data coverage. For example, a single point from another experiment might cover three CCFR bins, and the data would be put into a single bin. However, splitting the data up between the CCFR bins would simply introduce greater model dependence for no benefit. The binning correction is generally small except in the $x > 0.5$ region, where we use a special procedure (see section 7.3).

The second correction is only for experiments which use a deuterium target (specifically WA25). There we apply a correction to simulate the difference between a deuterium target and an iron target. This difference is known as the "EMC Effect," first observed by the European Muon Collaboration in 1983. As a function of x, they observed that the total μ-Fe cross-section is significantly reduced compared to the μ-D cross-section for the $0.4 < x < 0.8$ region.

For these relatively high values of x, the neutrino non-singlet SF xF_3 should be the same as the F_2 which defines the muon cross-section. Thus, for the WA25 experiment we apply the EMC effect as a correction. The other experiments are primarily heavy nuclei such as neon or freon (CF_3Br). It is assumed that there is no shape difference in xF_3 between these nuclei and iron.

Finally, to eliminate systematic differences, the other experiments are normalized to CCFR by calculating the ratio in the regions of overlap. This is calculated by a sum of logs.

$$R_{sum} = \sum_{(x,Q^2)} \left[\frac{log(xF_3^{CCFR}/xF_3^{Exp})}{\sqrt{(dxF_3^{CCFR})^2 + (dxF_3^{Exp})^2}} \right] \tag{7.1}$$

$$\Delta R_{sum} = \sum_{(x,Q^2)} log \left[\frac{1.}{\sqrt{(dxF_3^{CCFR})^2 + (dxF_3^{Exp})^2}} \right] \tag{7.2}$$

$$C_{NORM} = e^{r_{sum}/er_{sum}} \tag{7.3}$$

$$xF_3^{Exp} = xF_3^{Raw} \times C_{BIN} \times C_{EMC} \ / \ C_{NORM} \tag{7.4}$$

The normalization should remove systematic differences between different experiments.

Target Mass Correction

The final xF_3 correction, and the sole correction to the CCFR data, is the target mass correction. As explained in the introduction, these are expected in perturbative theory due to anomalous dimensions in the leading-twist operators [Nac74]. It is expected that mass correction terms of the form M^2/Q^2 play an important role in this region of Q^2. We therefore use the Nachtmann moments[Nac73] in

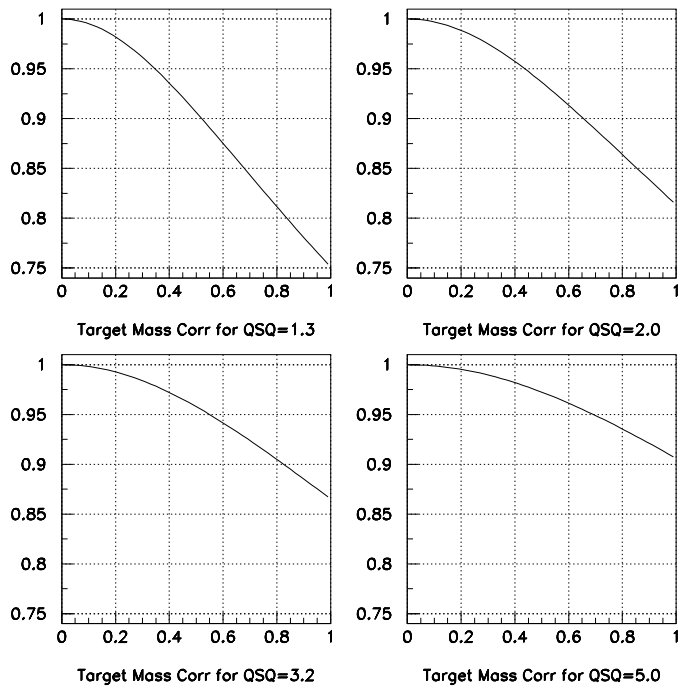

Figure 7.2: Target mass correction function in terms of x for the four lowest Q^2 bins.

terms of the variable

$$\xi = \frac{2x}{\left(1+\sqrt{1+4M^2x^2/Q^2}\right)} \tag{7.5}$$

which is assumed to absorb most of the mass corrections at finite Q^2. This can be converted into a function of the form:

$$\int_0^1 (xF_3)\frac{d\xi}{\xi} = \int_0^1 F_{TM}(xF_3)\frac{dx}{x} \tag{7.6}$$

$$F_{TM} = \left(\frac{\xi}{x}\right)^2 \frac{\left(1+2\sqrt{1+4M^2x^2/Q^2}\right)}{3} \tag{7.7}$$

F_{TM} is multiplied as a correction factor for each bin of the integral. The effect of this function is shown in Figure 7.2 for the four lowest Q^2 bins.

Calculating the Integral

Once we have a full set of data point in x, then it is fairly straightforward to calculate the integral. For now, we neglect the extrapolation at low-x below the data and the high-x ($x > 0.5$) interpolation shape. Assuming that the data is flat within the bin, the integral is simply:

$$\int_{x_1}^{x_2} \frac{[xF_3]_i}{x} dx = [xF_3]_i log\frac{x_2}{x_1} \tag{7.8}$$

This is modified by a shape correction for within the bin, again using the BGPAR function from Chapter 6. The flat-bin contribution is multiplied by the ratio of the BGPAR integral over the contribution assuming a flat bin around the BGPAR central value. In practice, this shape correction is very small except for high-x, where a special procedure is used (see Section 7.3).

7.2 Low-x Extrapolation

The CCFR data has a minimum x value of roughly ($x = 0.002 \times Q^2$). To extrapolate below this, we fit a function to all points with $x < 0.1$. The form of this extrapolation is a theoretical input to the measurement. Therefore, we should have systematic uncertainty which estimates our dependence upon this assumption.

The function form used was a power-law fit (Ax^B) to all points with $x < 0.1$, suggested by Regge theory [Bro73] as described below. The combined xF_3 data points are shown in Figure 7.3 on a log scale for x. The curve shows the fit, while the shaded region represents the contribution to the GLS integral from the fit.

Regge Theory

Regge theory is a phenomenological approach, which generalizes interaction by particle exchange. It characterizes the cross-section of two-body scattering as a function of the center of mass energy W of the interaction – where the angular momentum of the interaction is put on a complex plane. The poles of this complex plane (aka. "Regge poles") correspond to exchanged particles.

The position of each pole is described by a trajectory function $\alpha(t)$ where t is the momentum transfer of the interaction. The value of the trajectory function for $t = 0$ is called the intercept. In the Regge approximation the high energy behavior of the total cross section is given by:

$$\sigma_{tot}\left(\sqrt{s}\right) = \sum_i \beta_i (W^2)^{\alpha_i - 1} \tag{7.9}$$

$$\tag{7.10}$$

where α_i are the intercepts of the Regge poles, and β_i are their couplings. The intercepts α_i are universal quantities, i.e. they depend only on the quantum numbers of the Regge poles themselves. Phenomenologically, hadronic cross sections can be described by two poles: the first with $\alpha = 1$, which has vacuum quantum numbers and is known as the "pomeron"; and the second with $\alpha = 0.5$, which corresponds to the $\rho - f - w - A_2$ isovector exchange.

As $x \to 0$, the center of mass energy $W^2 \to \infty$ (since $x \sim Q^2/W^2$). Thus, this is the Regge limit where the sum is dominated by its leading terms. For the non-singlet structure function F_3, this

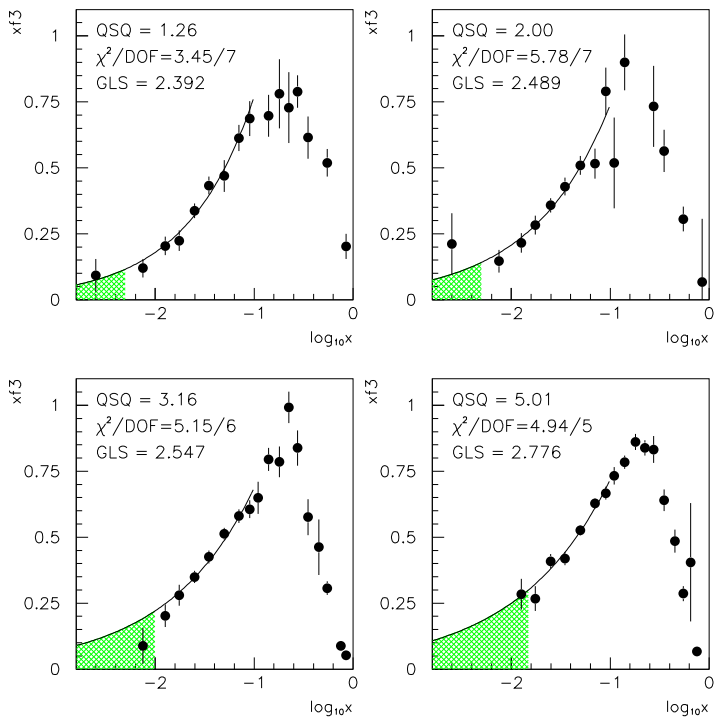

Figure 7.3: Combined data for $xF_3(x)$ showing the low-x fit. The log scale for x means that the area under the curve represents the contribution to the GLS integral.

limit translates to:

$$F_3(x,Q^2) = \sum_i \beta_i(Q^2)(W^2)^{\alpha_i - 1} \tag{7.11}$$

$$= \sum_i \beta_i(Q^2)(Q^2)^{\alpha_i - 1}(x)^{\alpha_i - 1} \tag{7.12}$$

$$xF_3(x,Q^2) = \sum_i \beta_i(Q^2)(Q^2)^{\alpha_i - 1}(x)^{\alpha_i} \tag{7.13}$$

For non-singlet exchange (i.e. xF_3), the pomeron cannot satisfy the helicity requirement. Therefore the leading pole for xF_3 is $\alpha = 1/2$ and $xF_3 \sim x^{1/2}$ in the Regge limit.

Fitting Procedure

Keeping this phenomenology in mind, we fit each of the xF_3 points for $x < 0.1$ to a function of form Ax^B. The results are shown on Table 7.1. As you can see, the Regge prediction is fairly accurate except in the lowest and highest Q^2 bins. The best fit (Ax^B) was used to calculate the integral

Q^2	A	B	Int	χ^2/DOF	C	Int	χ^2/DOF
1.26	3.70 ± 1.05	$0.68 \pm .08$	0.15	2.2/7	2.35 ± 0.12	0.23	7.3/8
2.00	2.63 ± 0.54	$0.55 \pm .06$	0.26	5.8/7	2.62 ± 0.09	0.26	6.5/8
3.16	2.42 ± 0.36	$0.53 \pm .05$	0.40	5.2/6	2.57 ± 0.06	0.37	5.5/7
5.01	2.17 ± 0.28	$0.47 \pm .04$	0.62	3.0/5	2.69 ± 0.05	0.49	3.3/5
7.94	2.40 ± 0.31	$0.48 \pm .05$	0.75	2.6/4	2.88 ± 0.05	0.61	2.8/4
12.59	2.48 ± 0.39	$0.49 \pm .06$	0.72	2.0/3	2.86 ± 0.05	0.76	2.0/3

Table 7.1: Results from fitting $x < 0.1$ to Ax^B and $Cx^{0.5}$, shown in different Q^2 bins. Int shows the contribution of that fit to the GLS integral. At higher Q^2 the fit is used over a wider range in x and has a larger contribution.

within and below the lowest x-bin where there was data (shown by the shaded region in Figure 7.3).

Estimating Fitting Error

The (Ax^B) function described above does not correspond exactly to Regge theory, but it was the best fit to the data. To test our dependence on this assumed form, we tried an alternate fit of form ($Ax^{0.5}$). This fit also produced a reasonable χ^2, but not as good as the primary fit. The alternate fit and the difference it makes is shown in Table 7.1. To be conservative, we have taken the best fit as the central value, and included the difference of the alternate fit as a systematic uncertainty on both sides.

7.3 High-x Interpolation

For $x > 0.5$, there are also few data points. Most of the data here comes from BEBC and SKAT which quote only two points for the range $0.5 < x < 1.0$. xF_3 is falling rapidly in this region and thus the exact shape within the bin is vital for accurate integration.

Further, the quoted points are bin-center corrected. That is, within a bin, the data has an average x value ($\langle x \rangle$) which is different from the center of the bin (i.e. $(x_{min} + x_{max})/2$). The experiments used some function to correct for the difference. In most cases, the bin-center correction is only a few percent and much less than the statistical error. Thus, the potential for bias is negligible. However, for the large bins at high-x, the correction can be up to 50% or more. It is unclear what functional shape BEBC or SKAT assumed for their correction.

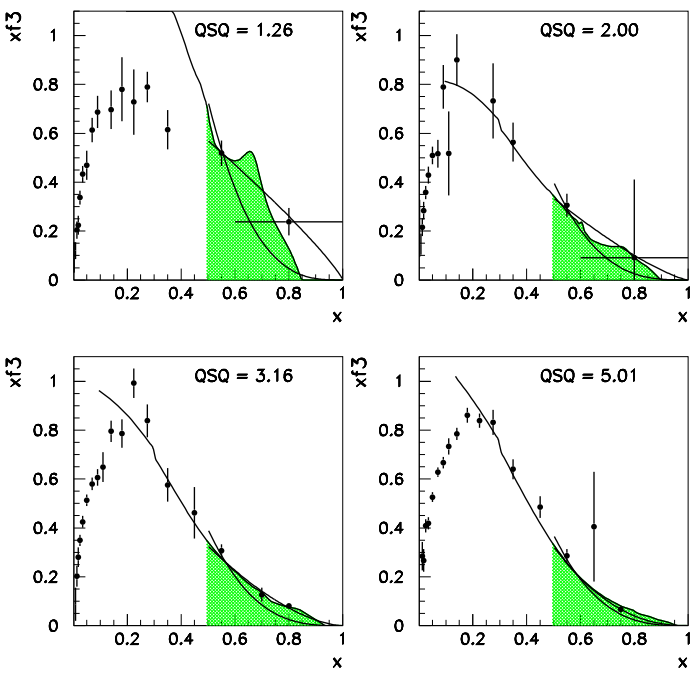

Figure 7.4: High-x data for combined xF_3, including corrected SLAC F_2 data as the shaded region. The other curves show the power-law fits to the xF_3 data. The linear scale for x means that the area under the curve does not represent the contribution to the GLS integral.

SLAC F_2 Data

For our central value, we use the principle that at high-x, the shape of F_2 should be the same as xF_3. SLAC has precisely measured F_2 in this region[Whi92]. Using this data corrected for the EMC effect[Gee95] and e-ν differences gives the same value as taking the shape and fitting the normalization to the xF_3 date.

The EMC effect has already been discussed earlier. The e-ν difference is known as the 5/18'ths rule, because neutrinos probe a different fraction of the quarks than electrons.

$$C_{SEA} = \frac{18}{5} \times \frac{1}{1 + \frac{6}{5}\frac{S(x,Q^2) - C(x,Q^2)}{Q(x,Q^2) + \overline{Q}(x,Q^2)}} \tag{7.14}$$

$$F_2^{\nu-N} = C_{SEA} F_2^{e-N} \tag{7.15}$$

where here S and C represent the strange and charm sea distributions, divided by the total quark and antiquark distributions.

$\langle Q^2 \rangle$	D	E	Int	χ^2/DOF	F	Int	χ^2/DOF
1.26	$1.09 \pm .28$	$0.91 \pm .24$	0.20	0/0	$4.69 \pm .49$	0.11	13.3/1
2.00	$0.88 \pm .35$	$1.36 \pm .47$	0.10	0/0	$2.75 \pm .41$	0.07	5.0/1
3.16	$1.07 \pm .22$	$1.68 \pm .18$	0.09	3.2/1	$2.96 \pm .22$	0.07	25.5/2
5.01	1.65 ± 1.1	$2.32 \pm .71$	0.08	0.7/1	$2.71 \pm .26$	0.07	1.5/2
7.94	$0.49 \pm .28$	$1.32 \pm .42$	0.07	0.4/2	$2.18 \pm .38$	0.06	9.3/3
12.59	$2.26 \pm .69$	$2.79 \pm .33$	0.07	7.9/2	$2.69 \pm .14$	0.07	7.5/3

Table 7.2: Results from fitting $x > 0.5$ to $D(1-x)^E$ and $F(1-x)^3$, shown in different Q^2 bins. Int shows the contribution of that fit to the GLS integral.

The results for the corrected SLAC F_2 are shown in Figure 7.4. While their overall level and shape at high Q^2 is in good agreement with the neutrino data, the shape at low Q^2 is in disagreement with the points from BEBC and SKAT. This is well within the systematic errors (see below).

Estimating Fitting Error

There are reasons to believe that the SLAC F_2 shape is not the same as the shape of xF_3. First of all, the SLAC eN scattering data has resonance peaks which result from production of excited states of the proton. These resonances correspond to particles of charge +1. Neutrino charged current reactions will have different resonances, corresponding to particles of charge +2 (+0) for ν ($\bar{\nu}$). The integrated totals of the different resonances should be similar, but there is not firm prediction that they are identical. In addition, the SLAC F_2 shape does not fit the two BEBC points in the first Q^2 bin.

Therefore, we attempt to be conservative with our systematic error. As alternatives to the F_2 shape, we fit the xF_3 data using two power law functions: $D(1-x)^E$ and $F(1-x)^3$. As shown in Figure 7.4, these functions bracket the SLAC F_2 shape and serve as limits of reasonable interpolation forms. The power law form is motivated by resonance behavior at low Q^2 coupled with approximate scaling. This predicts[Rob90] a form of $(1-x)^3$ as $x \to 1$. The $D(1-x)^E$ fit is less well motivated theoretically but more closely matches the shape of the data.

The results for the power law fits are shown in Table 7.2.

Quasi-elastic Term

The quasi-elastic term represents the special cross-section at $x = 1$ resulting from scattering where the proton remains a single particle in the final state. Such a scattering is quasi-elastic, rather than elastic, because the proton changes charge and mass in this scattering. Quasi-elastic scattering

Q^2	$\int_0^{.02} F_3$	$\int_{.02}^{.5} F_3$	$\int_{.5}^{1.} F_3$	qElas
1.0- 1.6	$0.376 \pm .082$	1.730	$0.183 \pm .073$	0.103
1.6- 2.5	$0.523 \pm .002$	1.843	$0.091 \pm .026$	0.033
2.5- 4.0	$0.558 \pm .026$	1.889	$0.092 \pm .020$	0.009
4.0- 6.3	$0.700 \pm .137$	1.991	$0.084 \pm .016$	0.002
6.3-10.0	$0.748 \pm .139$	2.004	$0.064 \pm .008$	0.0004
10.0-15.5	$0.718 \pm .113$	2.007	$0.073 \pm .003$	0.0001

Table 7.3: Contributions to the GLS integral from different regions of x and the quasi-elastic peak added at $x = 1$, shown as a function of Q^2 (in GeV^2). For high and low x, it shows the estimated uncertainties due to the model choice only. The values include the target mass corrections.

cannot be predicted by perturbative calculations, but it is included in the non-perturbative higher-twist correction.

Table 7.3 shows the contributions to the GLS from different regions of x, including the quasi-elastic peak.

7.4 Systematic Errors

The uncertainties are divided into two classes. First is calibration, normalization, and other purely experimental issues. Second is model-based errors in the integration of experimental xF_3, estimated by varying the assumed functional form.

The dominant experimental systematic uncertainties are in the overall normalization of xF_3, which comes from the total neutrino and anti-neutrino cross-sections (σ_ν and $\sigma_{\overline{\nu}}$). Absolute σ_ν is not measured by CCFR, so we use the world average ($\sigma_\nu / E_\nu = 0.677 \pm .007 \times 10^{-38} cm^2/GeV$). The ratio $\sigma_{\overline{\nu}}/\sigma_\nu$ is measured by CCFR, and combined with the world average yields ($\sigma_{\overline{\nu}}/\sigma_\nu = 0.499 \pm .007$). Other experimental uncertainties include the energy scale calibration of the detector and the effects of charm on the cross-section.

The model errors are estimated by varying the assumed functional forms in the analysis. First is the model used for acceptance and smearing corrections of the SF data. This is a fit to the SF data with a form suggested by leading-order QCD. The low-x model uncertainty is estimated by making a fit of form ($Ax^{0.5}$) instead of (Ax^B). The high-x model uncertainty is estimated by using similar power law fits ($C(1-x)^D$ and $E(1-x)^3$) rather than the measured F_2 shape.

Chapter 8

Extraction of α_s and Conclusions

The results from the previous chapter are a set of purely experimental values for the GLS integral at different values of Q^2. This chapter describes the QCD calculation which those values are compared to, extracting a value of $\alpha_s$which represents the best fit to those points. The fit is done in a standard manner, forming a chi-squared between the experimental GLS and GLS theory.

8.1 GLS Theory

The theoretical prediction for the GLS sum rule is calculated as a function of $\alpha_s$and the number of accessible quark flavors, n_f. In its final form, the NNLO perturbative QCD and non-perturbative QCD calculations result in a prediction of:

$$GLS(n_f) = 3(1 - \tfrac{\alpha_s}{\pi} - a(n_f)(\tfrac{\alpha_s}{\pi})^2 - b(n_f)(\tfrac{\alpha_s}{\pi})^3) - \frac{\Delta HT}{Q^2} \quad (8.1)$$

$$a(n_f) = 55/12 - n_f/3 \quad (8.2)$$

$$b(n_f) = 41.441 - 8.02n_f + 0.177n_f^2 \quad (8.3)$$

$$\Delta HT = 0.15 \pm .15\ GeV^2 \quad (8.4)$$

The theoretical prediction for GLS is shown in Figure 8.1. This prediction is using the $\overline{MS}$ renormalization scheme, although the values for other renormalization schemes have also been calculated. Because of the high order to which this has been calculated, the differences between renormalization schemes are minimal. In addition to the standard $\overline{MS}$ scheme, the GLS prediction was calculated in the principle of minimal sensitivity (PMS) scheme[Ste81] and the effective charges (ECH) scheme[Gru84]. These produced minimal difference in the results[Kat92]. The change caused by other schemes corresponds to a difference of order ± 0.002 in $\alpha_s(M_Z^2)$ in the $\overline{MS}$ scheme.

Note that α_s and the correction terms is rapidly decreasing as Q^2 increases. Therefore, the power of the measurement is primarily in the low-Q^2 bins. At higher Q^2, the same error in the GLS integral results in a much larger error in α_s. For $Q^2 > 5\ GeV$ most points, including all uncertainties, are within error of $GLS(Q^2) = 3$. In addition, the low-x extrapolation uncertainty

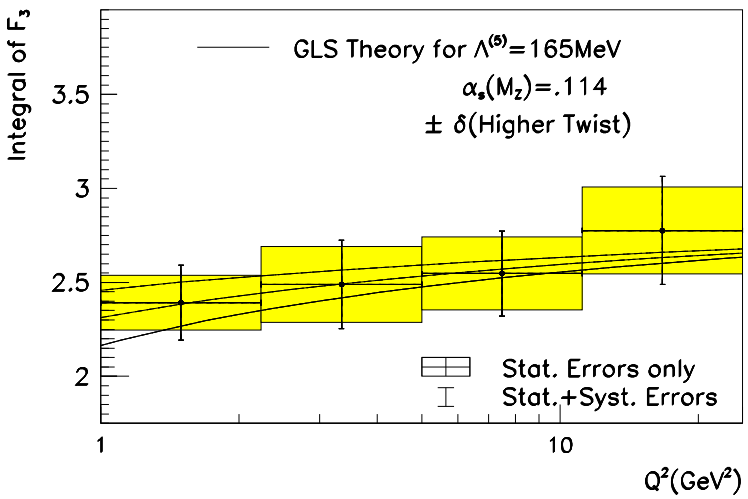

Figure 8.1: The data for the GLS integral as a function of Q^2. The central curve is the theoretical prediction for $\Lambda_{\overline{MS}}^{(5)} = 165\ MeV$, corresponding to the best fit. The other curves correspond to the higher twist error.

increases with increasing Q^2.

Perturbative Terms

The perturbative terms are calculated as a function of the n_f, the number of quark flavors. For high values of Q^2, this is commonly set to a fixed value, such as 5.

However, at small values of x and Q^2, the situation is complicated by quark mass thresholds. As all the NNLO QCD calculations have been performed assuming massless quarks, the effect of quark mass thresholds must be added in. Specifically, n_f depends on whether the total hadronic energy W is above the threshold to create a quark-antiquark pair. These thresholds can be expressed as a function of W by:

$$W^2 = Q^2\frac{(1-x)}{x} + m_p^2 \tag{8.5}$$

$$n_f = \begin{cases} 3 & W^2 < 4m_c^2 \\ 4 & 4m_c^2 < W^2 < 4m_b^2 \\ 5 & W^2 > 4m_b^2 \end{cases} \tag{8.6}$$

At fixed Q^2, these thresholds divide up the x range into three regions. At very high Q^2, n_f is 5 for the great majority of the x range. However, at low Q^2, there is a significant admixture of $n_f = 3, 4, 5$. Ideally, the NNLO calculation should be done for massive quarks to take into account these thresholds – but in practice this is impossible.

As an approximation, the theoretical prediction for the GLS sum rule is formed by calculating

GLS separately for each n_f, and then averaging them based on the importance at each n_f. For a given Q^2, we estimate the fraction of the GLS integral which comes from each region in x. The fraction of the theoretical GLS taken from each x-region should match the fraction of the experimental sum from that range. However, in practice this is a minor effect and we can use the BGPAR model of xF_3 (see Chapter 6) and get the approximate fractions.

$$GLS = \sum_{n_f=3,5} \frac{\int_{xmin(n_f)}^{xmax(n_f)} (xF_3)^{Model} \frac{dx}{x}}{\int_0^1 (xF_3)^{Model} \frac{dx}{x}} GLS(\alpha_s(n_f)) \tag{8.7}$$

$$xmin(3) = 0 \tag{8.8}$$

$$xmax(3) = xmin(4) = Q^2/(Q^2 + 4m_c^2 - m_p^2) \tag{8.9}$$

$$xmax(4) = xmin(5) = Q^2/(Q^2 + 4m_b^2 - m_p^2) \tag{8.10}$$

$$xmax(5) = 1 \tag{8.11}$$

Reasonable variations in the model produced negligible change in the overall GLS prediction. Besides the central BGPAR, an alternate BGPAR and MRS parameterizations were tried.

Calculating Alpha

As mentioned in Chapter 1, the strong coupling "constant" (α_s) is actually a variable function of Q^2 and the scale $\Lambda_{\overline{MS}}$. To be consistent with the NNLO perturbative calculation, we need to calculate $\alpha_s$to the third term of $\Lambda_{\overline{MS}}$.

$$\frac{\alpha_s(Q^2)}{4\pi} = \frac{1}{\beta_0\ L}\left[1 - \frac{\beta_1 \log L}{\beta_0^2\ L} + \frac{\beta_1^2 \log^2 L - \beta_1^2 \log L + \beta_2\beta_0 - \beta_1^2}{\beta_0^4\ L^2}\right] \tag{8.12}$$

$$L = \log[Q^2/\lambda^2(n_f)] \tag{8.13}$$

$$\beta_0 = 11 - \frac{2}{3}n_f \tag{8.14}$$

$$\beta_1 = 102 - \frac{38}{3}n_f \tag{8.15}$$

$$\beta_2 = \frac{2857}{2} - \frac{5033}{18}n_f + \frac{325}{54}n_f^2 \tag{8.16}$$

The results for $\alpha_s(\Lambda_{\overline{MS}})$ are shown in Figure 8.2. Here β_0 and β_1 are scheme-independent, while the value given for β_2 is in the $\overline{MS}$ scheme. Note that this "three-loop" calculation is different than the "two-loop" calculation used in most other measurements of $\alpha_s$which are NLO rather than NNLO in QCD. The difference is illustrated in Figure 8.3. This difference is inherent with trying to compare predictions calculated in different orders.

Higher Twist

The higher twist correction is calculated as a twist-4 contribution, resulting in a single correction term proportional to $(1/Q^2)$. It is estimated by averaging the results of non-perturbative quantum

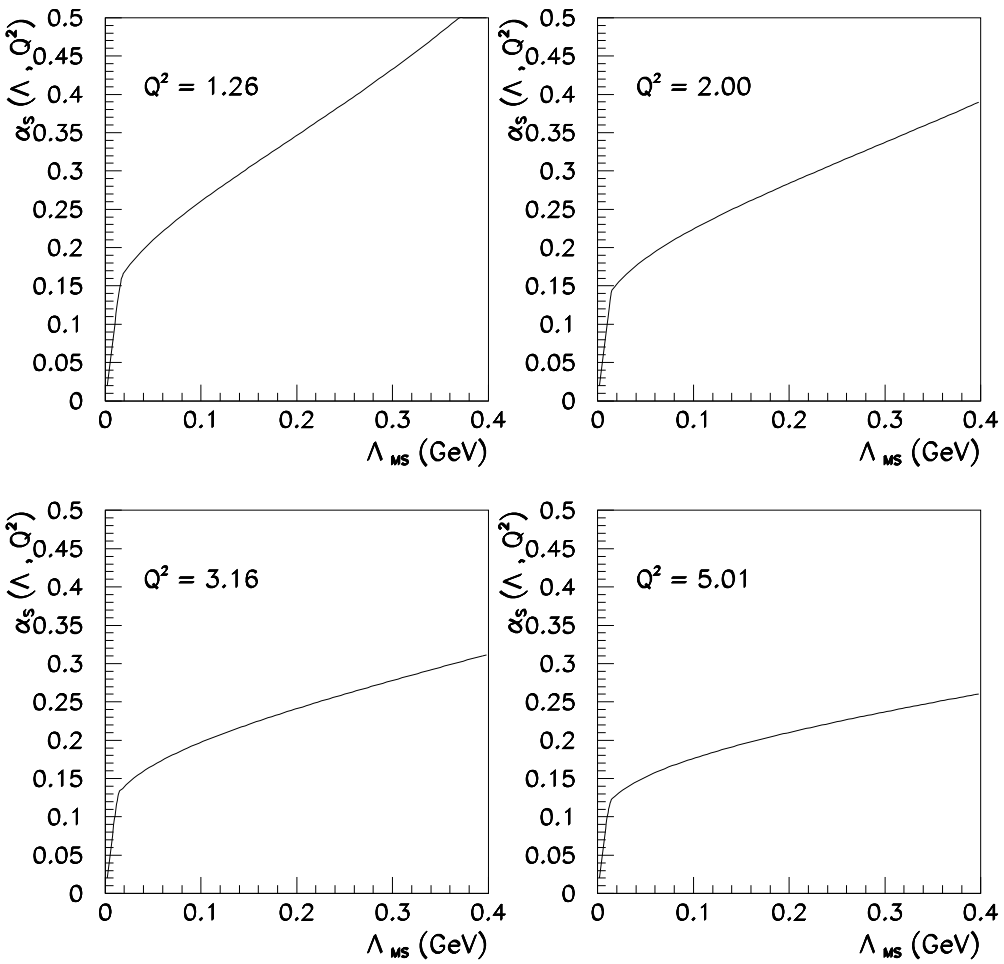

Figure 8.2: α_s as a function of $\Lambda_{\overline{MS}}^{(5)}$. The different plots here show the progression for four values of Q^2 corresponding to the four lowest Q^2 bins.

calculations using various phenomenological models for the proton wave-function. The error is estimated by the amount this prediction varies among different techniques.

The basic calculation is for the first matrix element, $\langle\langle O^S \rangle\rangle$.

$$O_\mu^S = \overline{u}\tilde{G}_{\mu\nu}\gamma_\nu\gamma_5 u \pm \overline{d}\tilde{G}_{\mu\nu}\gamma_\nu\gamma_5 d \tag{8.17}$$

$$\tilde{G}_{\mu\nu} = \frac{1}{2}\varepsilon_{\mu\nu\alpha\beta}G^a_{\alpha\beta}\frac{\lambda^a}{2} \quad , \quad a = 1, ..., 8 \tag{8.18}$$

$$< P|O_\mu^S|P >_{\text{spin averaged}} = 2\ p_\mu \langle\langle O^S \rangle\rangle \tag{8.19}$$

$$\Delta HT = \frac{8}{9}\langle\langle O^S \rangle\rangle \tag{8.20}$$

Various non-perturbative techniques are used to estimate the wavefunction for the proton ($< P|$

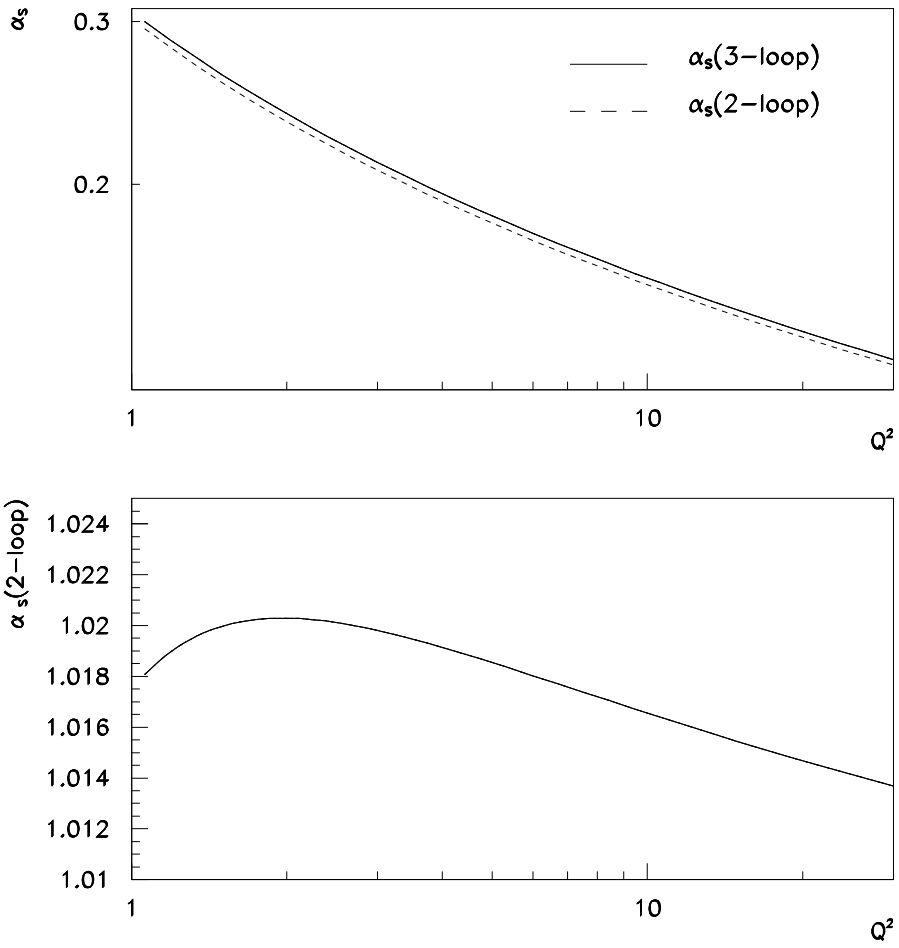

Figure 8.3: Two-loop and three-loop predictions for $\alpha_s(Q^2)$. This shows the predictions for $\lambda^{(5)}_{\overline{MS}} = 165\ MeV$. The top plot shows separately the three-loop and two-loop function. The bottom plot shows the ratio of these two.

in the calculation above), which produce varying results for $\langle\langle O^S \rangle\rangle$. Three techniques attempted by Braun and Kolesnichenko[Bra87] found values of $\langle\langle O^S \rangle\rangle$which indicated a significant correction to the GLS. Other techniques, including a recent NNLO renormalon approach[Bod98] and an earlier MIT bag model[Faj85] found that the higher twist correction is negligible. The models considered include:

1. QCD Sum Rules Approach [Bra87]
   This approach is an approach using phenomenological data from hadron resonance, while estimating QCD matrix elements in an independent way using various approximations [Shi79]. This has an input of $\alpha_s(Q^2 = 1\ GeV^2) = 0.368$ (page 735 of [Bra87]). It gives a result of

$\langle\langle O^S \rangle\rangle = 0.33\ GeV^2$.

2. Vector (ω)ρ-Dominance Approximation [Bra87]
   Vector dominance is the assumption that the exchanged W boson couples most strongly to the lightest possible vector mesons; the vector mesons then interact hadronically with the nucleon. This technique uses QCD sum rules under the VD approximation. This gives a result of $\langle\langle O^S \rangle\rangle = 0.18 - 0.27\ GeV^2$.

3. Simple Non-relativistic Quark Model [Bra87]
   This is a non-QCD-based technique which employs massive quarks ($m_q \sim 350\ MeV$), interacting via exchange of gluons [Isg78]. Rederiving the operators with massive quarks, this gives a result of $\langle\langle O^S \rangle\rangle = 0.2\ GeV^2$.

4. MIT Bag Model [Faj85]
   This is a technique using various quark confinement models to estimate the proton wavefunction. The models produce widely varying results compared to each other, but all of them produce very small values of the correction, $0.0002 < \langle\langle O^S \rangle\rangle < 0.009\ GeV^2$.

5. Renormalon approach [Bod98]
   This is a recent NNLO technique being done by CCFR collaborators. The renormalon approach[Das96] condenses higher twist into one or two parameters which can be fitted experimentally. Fitting to non-CCFR deep inelastic scattering data results in $\langle\langle O^S \rangle\rangle \cong .0087\ GeV^2$. There is minor variation with the exact Q^2 and α_s chosen.

As a result of this, we choose a value of $\langle\langle O^S \rangle\rangle$which covers the large values suggested by Braun and Kolesnichenko, but also covers a value of zero as suggested by the other techniques. This corresponds to $\langle\langle O^S \rangle\rangle = 0.17 \pm .17$ or equivalently $\Delta HT = 0.15 \pm .15$. This result will be different for an iron target due to nuclear effects. However, the nuclear effects of the target are predicted to be small[Kul97] ($-0.01/Q^2$ for iron), and are thus easily covered by our error.

As an added test, the higher twist constant (ΔHT) was allowed to vary. The value for ΔHT and $\alpha_s$were extracted as a two-parameter fit, with the constraint that the χ^2 increased by 1 for every 1σ that ΔHT was allowed to vary from its average value. This produced a slightly lower value of $\alpha_s$and a slightly higher value of ΔHT, but well within the quoted error.

8.2 Fitting Procedure and Results

The experimental results for the GLS integral in each Q^2 bin are fitted to the NNLO pQCD function and higher-twist term. This gives a best fit of $\Lambda^{(5)}_{\overline{MS}} = 165\ MeV$. Evolving to M_Z^2 at NNLO, this corresponds to:

$$\alpha_s(3\ GeV^2) = 0.278 \pm .035(stat) \pm .05(syst) \pm^{.035}_{.03} (thry) \quad (8.21)$$

$$\alpha_s(M_Z^2) = 0.114 \pm^{.005}_{.006} (stat) \pm^{.007}_{.009} (syst) \pm .005(thry) \quad (8.22)$$

If the higher-twist term is neglected, the central value becomes $\alpha_s(M_Z^2) = 0.118$. The results for GLS and α_s at each Q^2 bin are shown in Table 8.1.

$\langle Q^2 \rangle$	$GLS(Q^2)$	$\alpha_s(Q^2)$
1.26	$2.39 \pm .08 \pm .14$	$0.330 \pm .023 \pm .042 \pm .050$
2.00	$2.49 \pm .08 \pm .10$	$0.303 \pm .020 \pm .026 \pm .036$
3.16	$2.55 \pm .06 \pm .10$	$0.287 \pm .008 \pm .034 \pm .026$
5.01	$2.78 \pm .06 \pm .19$	$0.165 \pm .033 \pm .144 \pm .024$
7.94	$2.82 \pm .07 \pm .19$	$0.145 \pm .061 \pm .136 \pm .022$
12.59	$2.80 \pm .13 \pm .18$	$0.164 \pm .068 \pm .101 \pm .014$

Table 8.1: The total GLS integral and α_s for each bin in Q^2. The errors on the GLS are $\pm(stat) \pm (syst)$. The errors on $\alpha_s(Q^2)$ are $\pm(stat) \pm (syst) \pm (thry)$. Systematic errors are correlated.

Systematic Uncertainties

The systematic uncertainties are divided into three classes. The first includes calibration, normalization, and other purely experimental issues. The second is uncertainty in the integration of experimental xF_3, estimated by varying the assumed functional form as described above. The third class includes uncertainties in the theoretical prediction of the GLS integral itself. A summary of all the uncertainties is shown in Table 8.2.

The dominant experimental systematic uncertainties are in the normalization of xF_3, which comes from the total neutrino and anti-neutrino cross-sections (σ_ν and $\sigma_{\bar{\nu}}$). The absolute σ_ν is not measured by CCFR, so we use the world average[Auc90,Bla83,Ber91] ($\sigma_\nu / E_\nu = 0.677 \pm .007 \times 10^{-38} cm^2/GeV$). The ratio $\sigma_{\bar{\nu}}/\sigma_\nu$ is measured by CCFR, and combined with the world average[Bla83,Ber91,Sel97] yields $\sigma_{\bar{\nu}}/\sigma_\nu = 0.499 \pm .007$. Other experimental uncertainties include the energy scale calibration of the detector and the effects of charm production on the measured structure functions.

Additionally, there is a small uncertainty in the revised calculation of acceptance and smearing corrections. These corrections depend on a parameterization of the SFs. Reasonable variations of the functional form of the parameterization were used to estimate the systematic error.

The dominant theoretical uncertainty is the error on the higher-twist correction ($\Delta HT/Q^2$). Braun and Kolesnichenko[Bra87] use three models which predict a correction term ΔHT between 0.16 and 0.29 GeV^2. Other models, such as bag models[Faj85] and a recent NNLO analysis[Bod98] using a renormalon[Das96] approach, predict a negligible correction term ($\Delta HT < 0.02\ GeV^2$). For our central value, we take $\Delta HT = 0.15 \pm .15\ GeV^2$, thus covering both predictions. The nuclear effects of the target are predicted to be small[Kul97] ($-0.01/Q^2$ for iron). We also use estimates of the renormalization scheme dependence[Kat92] and the order α_s^4 term in the pQCD expansion[Kat95] as uncertainties in the perturbative calculation.

Source	**Error**
Statistical	$\left(\begin{smallmatrix}+.005\\-.006\end{smallmatrix}\right)$
σ_ν Normalization	$\left(\begin{smallmatrix}+.003\\-.005\end{smallmatrix}\right)$
$\sigma_\nu/\sigma_{\bar{\nu}}$ Ratio	$\left(\begin{smallmatrix}+.005\\-.006\end{smallmatrix}\right)$
Energy Calibration	$\left(\begin{smallmatrix}+.002\\-.003\end{smallmatrix}\right)$
Charm Production	$\pm.0005$
Acceptance model	$\pm.002$
Total Experimental Error	$\left(\begin{smallmatrix}+.006\\-.008\end{smallmatrix}\right)$
High-x fitting	$\pm.003$
Low-x fitting	$\pm.002$
Total Model Error	$\pm.004$
Combined Systematic Error	$\left(\begin{smallmatrix}+.007\\-.009\end{smallmatrix}\right)$
Higher-twist	$\left(\begin{smallmatrix}+.004\\-.005\end{smallmatrix}\right)$
Renormalization Scheme[Kat96]	$\pm.001$
Order α_s^4	$\pm.0003$
Total Theory Error	$\pm.005$

Table 8.2: Uncertainties in $\alpha_s(M_Z^2)$.

8.3 Comparison to other Measurements and Conclusions

There already exist several measurements of α_s with comparable errors to the GLS sum rule method. However, an important test of QCD as a theory is that measurements by differing methods achieves the same results. The GLS is one of the few quantities calculated to NNLO in QCD, and which consequently has low dependence on renormalization scheme. Systematic differences between the GLS and other measurements could be a signal for the need for higher orders in the other measurements (i.e. NNLO), the need for better understanding of higher twist, or even new physics.

The measurement of α_s by the GLS sum rule has a nearly unique level of theoretical understanding, and is conducted at a lower value of Q^2 than most other measurements. An independent CCFR calculation[Sel97] used global NLO fits to xF_3 and F_2 for $15 < Q^2 < 125\ GeV^2$. This found $\alpha_s(M_Z^2) = 0.119 \pm .004$ at an average Q^2 of 30 GeV. The other values shown in Figure 8.4 are averages computed by the Particle Data Group [Bar96]. Summarized below are the physical processes used to derive these values, starting with the lowest

- The Bjorken Sum Rule can be used to put a loose constraint on α_s at low Q^2. This is a parton level integral for polarized structure functions, calculated to NLO in QCD. This Bjorken Sum Rule measurement[Alt97] corresponds to $\alpha_s(M_Z^2) = 0.120^{+.010}_{-.008}$, at an average Q^2 of 2.5 GeV.
- The hadronic branching ratio of τ decay, BR$[\tau \rightarrow \nu_\tau + hadrons]$, can be used to compute

$\alpha_s(M_\tau^2) = 0.370 \pm .033$. This corresponds to $\alpha_s(M_Z^2) = 0.115 \pm .003$.

- Lattice QCD calculation of the energy levels of a $Q\overline{Q}$ system $\alpha_s(M_Z^2) = 0.115 \pm .003$ This is the more accurate "unquenched" calculation which does not use the quenching approximation for light quark masses.

- The HERA DIS result [Bal95] determines $\alpha_s = 0.120 \pm .005(\text{exp}) \pm .009(\text{theory})$ by including the x-dependence, rather than just the Q^2-dependence, of the structure functions at very small x and very large Q^2.

- The jet rates at HERA can also be used to determine α_s, by comparing the rates for $(e + q \rightarrow e + q)$ to $(e + q \rightarrow e + q + g)$. The first process produces a (1+1) jet, since one jet is associated with the proton fragment and the other with the struck quark, while the second process produces a (2+1) jet. The result shown is the average for H1 and ZEUS of $\alpha_s(M_Z^2) = 0.121 \pm .004(\text{stat}) \pm .008(\text{syst})$.

- The decays of $Q\overline{Q}$ systems such as the Υ can be used to determine α_s by measuring the ratio:

$$R_\Upsilon = \frac{\Gamma(\Upsilon \rightarrow hadrons)}{\Upsilon \rightarrow \mu^+\mu^-} \tag{8.23}$$

  This finds a value of $\alpha_s(M_Z^2) = 0.108 \pm .010$.

- The fragmentation function $d_i(x, E)$ is the probability that a hadron of type i is produced with energy E in e^+e^- collisions at $(\sqrt{s} = 2E)$. QCD predicts the E-dependence of the fragmentation function. Experiments at LEP have determined the value of $\alpha_s(M_Z^2) = 0.125 \pm .006$ (exp) $\pm .006$ (theory) from this technique.

- The total cross-section for $e^+e^- \rightarrow hadrons$, known as $R(e^+e^-)$, has QCD corrections which can be used to measure α_s. This method yields $\alpha_s(34\ GeV) = 0.146 \pm .030$, which corresponds to $\alpha_s(M_Z^2) = 0.125 \pm .023$.

- In e^+e^- collisions, the total jet rates for two-jet, three-jet, and four-jet events can be used to determine α_s. A search for jets in special kinematic configurations can also be used. This technique yields an average $\alpha_s(M_Z^2) = 0.122 \pm .007$.

Figure 8.4 shows a comparison of the different methods of measuring α_s as a function of Q^2. Figure 8.5 shows these measurements extrapolated to the mass of the Z.

8.4 Conclusions

The GLS sum rule has been used to measure α_s in a new kinematic region and with a high degree of theoretical accuracy. This result is in agreement with other measurements at Q^2 four orders of magnitude higher. This agreement is a confirmation of the power of perturbative QCD across a very wide range of scales.

The value of α_s from the GLS sum rule is not the most accurate in total uncertainty. However, it forms an important check on possible theoretical and systematic effects on other measurements.

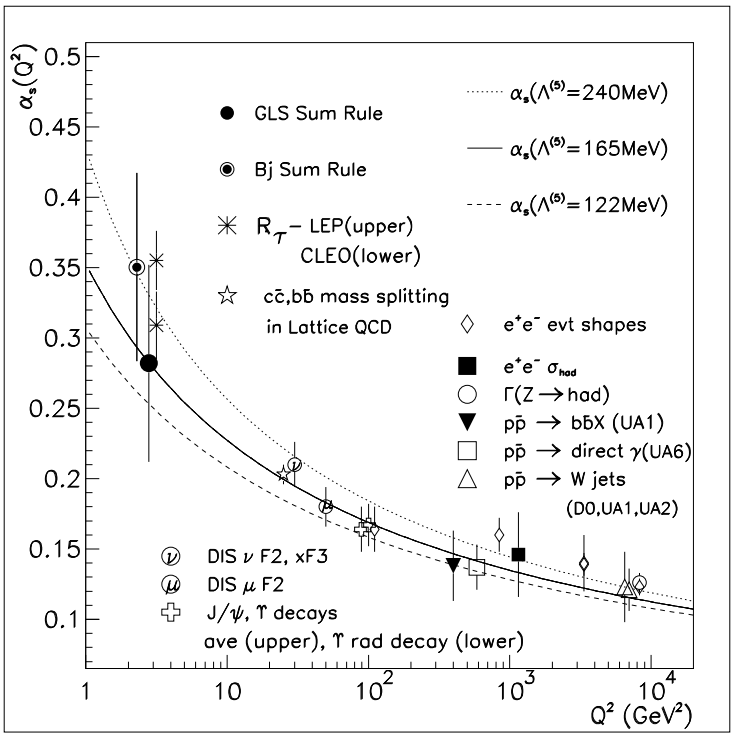

Figure 8.4: $\alpha_s(Q^2)$ for different experiments. The lines show the predicted extrapolation of the central GLS result, and the lines corresponding to its statistical (only) errors.

Several years ago, it had been noted that measurements at low Q^2 tended to favor lower values of $\alpha_s$than the high-Q^2 measurements such as those at LEP. There were a number of suggestions of mechanisms which would account for this. For example, the existence of a light gluino [Blu94] or light superpartners [Kan95] in supersymetry could produce a lower value of $\alpha_s$at low Q^2 than $\alpha_s$measured at high Q^2. With this result, there is no evidence for a systematic difference – so if an effect exists, it would be at a level below the known uncertainties. More recent results, including the GLS, have tended to rule out such mechanisms within the level of current uncertainties.

The GLS result can be improved in the future first by additional data from the NuTeV experiment, which should reduce the statistical error and the $\sigma_{\bar{\nu}}/\sigma_\nu$ systematic error. Better understanding of the higher twist effects may confirm the renormalon approach a significantly reduce the theoretical error.

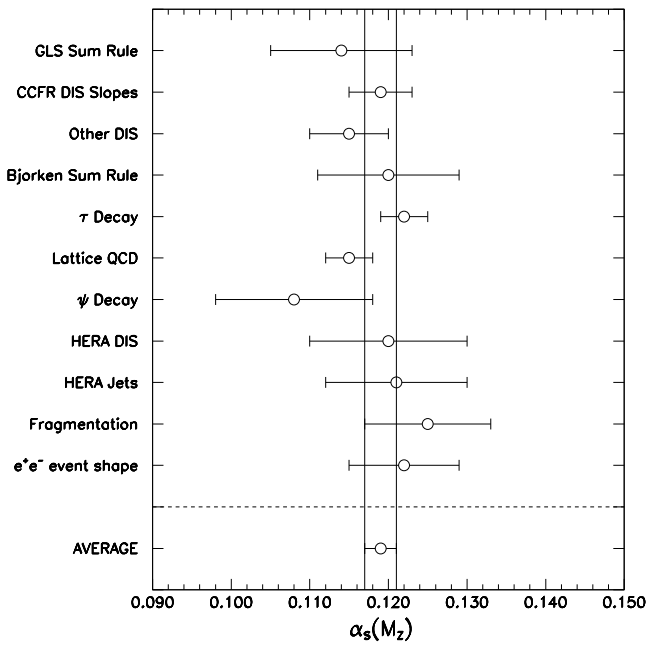

Figure 8.5: $\alpha_s(M_Z^2)$ for different experiments.

Bibliography

[All85] "Q^2 Dependence of the Proton and Neutron Structure Functions from Neutrino and Anti-neutrinos Scattering in Deuterium"; Allasia et al., *Zeit. Phys.* **C28** (1985) 321.

[Amm78] Ammosov et al., *Nucl. Phys.* **B142** (1978) 1.

[Amm82] Ammosov et al., *JETP Lett.* **36** (1982) 300.

[Amm86] "Inclusive Study of Neutrino and Anti-neutrino interactions with Nuclei at Energies $E_{\bar{\nu}} \leq 30\ GeV$"; Ammosov et al., *Zeit. Phys.* **C30** (1986) 175.

[Bal95] "Determination of α_sFrom F2(P) at HERA"; R.D. Ball and S. Forte (CERN); *Phys. Lett.* **B358** (1995) 365.

[Bar79] D.Y. Bardin and O.M. Fedorenko, *Sov. J. Nucl. Phys.* **30(3)** (1979) 418.

[BCD87] BCDMS Collab., A.C. Benvenuti et al., *Phys. Lett.* **B195** (1987) 91.

[BCD90] BCDMS Collab., A.C. Benvenuti et al., *Phys. Lett.* **B237** (1990) 592.

[Blu94] "Do Deep Inelastic Scattering Data Favor a Light Gluino"; J. Blumlein and J. Botts DESY-94-008(Jan 1994); hep-ph/9401291

[Bod98] "Corrections to Parton Distribution Functions and Higher Twist Coefficients at High x from a Global Study of Deep Inelastic Scattering Experiments"; A. Bodek and U.K. Yang, University of Rochester Preprint UR-1519 (1998)

[Bra87] V.M. Braun and A.V. Kolesnichenko, *Nucl. Phys.* **B283** (1987) 723.

[Bro73] S.J. Brodsky and G. Farrar, *Phys. Rev. Lett.* **31** (1973) 1153.

[Bur78] "Simple Parametrizations of Parton Distributions with Q^2 Dependence Given by Asymptotic Freedom"; A.J. Buras and K.J.F. Gaemers *Nucl. Phys.* **B132** (1978) 249.

[Chy95] "What does the the CCFR measurement of the Gross-Llewellyn Smith sum rule tell us?"; J. Chyla and J. Rames, *Phys. Lett.* **B343** (1995) 351.

[Das96] "Power corrections and renormalons in deep inelastic structure functions"; M. Dasgupta and B.R. Webber, *Phys. Lett.* **B382** (1996) 273.

[Faj85] "Non-perturbative QCD Corrections to the Bjorken and Gross-Llewellyn Smith Sum Rules"; S. Fajfer and R.J. Oakes *Phys. Lett.* **B163** (1975) 385.

[Gee95] D.F. Geesaman et all, *Ann. Rev. Nucl. Part. Sci.* **45** (1995) 337.

[Gro69] "High-energy Neutrino-nucleon Scattering, Current Algebra and Partons"; D.J. Gross and C.H. Llewellyn Smith, *Nucl. Phys.* **B14** (1969) 337.

[Gru84] "Renormalization scheme independent of QCD and QED: the method of effective charges."; G. Grunberg, *Phys. Rev.* **D29** (1984) 2315.

[Isg78] "P Wave Baryons in the Quark Model"; N. Isgur and G. Karl, *Phys. Rev.* **D18** (1978) 4187;.

[Kan95] "A Global Fit of LEP/SLC Data with Light Superpartners"; G.L. Kane, R.G. Stuart, J.D. Wells *Phys. Lett.* **B354** (1995) 350.

[Kat92] A.L. Kataev and A.V. Sidorov, *Phys. Lett.* **B297** (1992) 385.

[Kat94] "The Jacobi polynomials QCD analysis of the CCFR data for xF_3 and the Q^2-dependence of the Gross-Llewellyn Smith Sum Rule"; A.L. Kataev and A.V. Sidorov, *Phys. Lett.* **B331** (1994) 179.

[Kat95] "Estimates of the Higher-order QCD Corrections to $R(S)$, R_τ and Deep Inelastic Scattering Sum Rules"; A.L. Kataev and V.V. Starshenko, *Mod. Phys. Lett.* **A10** (1995) 235.

[Kin91] "Measuring Muon Momenta With the CCFR Neutrino Detector"; B.J. King et al., *Nucl. Instr. Meth. Phys. Res., Sect. A* **302** (1991) 254.

[Kin94] "A Precise Measurement of the Weak Mixing Angle in Neutrino-Nucleon Scattering"; B.J. King, Ph.D. Thesis (Columbia University); Nevis Reports 283 (1994)

[Kul97] S.A. Kulagin (Moscow,INR), INR-0967-97, Dec 1997

[Lar91] "The ${\alpha_s}^3$ Corrections to the Bjorken Sum Rule for Polarized Electroproduction and to the Gross-Llewellyn Smith Sum Rule"; S.A. Larin and J.A.M. Vermarseren, *Phys. Lett.* **B259** (1991) 345.

[Leu93] "A Measurement of the Gross-Llewellyn Smith Sum Rule from the CCFR xF_3 Structure Function"; W.C. Leung et al., *Phys. Lett.* **B317** (1993) 655.

[Mar84] W.J. Marciano, *Phys. Rev.* **D29** (1984) 580.

[Nac73] "Posivity Constraints for Anomalous Dimensions"; O. Nachtmann, *Nucl. Phys.* **B63** (1973) 237.

[Nac74] "Is There Evidence for Large Anomalous Dimensions?"; O. Nachtmann, *Nucl. Phys.* **B78** (1974) 455.

[NMC92] "Proton and deuteron F_2 structure functions in deep inelastic muon scattering."; NMC Collab., P. Amaudruz et al., *Phys. Lett.* **B295** (1992) 159.

[Qui93] "Measurement of λ_{QCD} from ν_μ-Fe Nonsinglet Structure Functions at the Fermilab Tevatron"; P.Z. Quintas et al., *Phys. Rev. Lett.* **71** (1993) 1307.

[Rab92] "Opposite Sign Dimuon Production in Neutrino Interactions at the Fermilab Tevatron"; S.A. Rabinowitz (Columbia University); Ph. D. Thesis, Nevis Reports 291 (1992)

[Rab93] "Measurements of the Strange Sea Distribution Using Neutrino Charm Production"; S.A. Rabinowitz et al., *Phys. Rev. Lett.* **70** (1993) 134.

[Rob90] *The Structure of the Proton*; R.G. Roberts; Cambridge University Press (1990).

[Sak90] "Calibration of the CCFR Target Calorimeter"; W.S. Sakumoto et al., *Nucl. Instr. Meth. Phys. Res., Sect. A* **294** (1990) 179.

[Sel97] W.G. Seligman et al., *Phys. Rev. Lett.* **79** (1997) 1213.

[Shi79] "QCD and Resonance Physics Theoretical Foundations"; M.A. Shifman, A.I. Vainshtein, and V.I. Zakharov, *Nucl. Phys.* **B147** (1979) 385.

[Sid96] "Next to Next-to-Leading Order QCD Analysis of Combined Data for xF_3 Structure Function and Higher Twist Contribution"; A.V. Sidorov, Published in JINR Rapid Commun.80(1996)11 (e-Print Archive: hep-ph/9609345)

[Ste81] "Optimized Perturbation Series"; P.M. Stevenson *Phys. Rev.* **D23** (1981) 2916.

[Var87] "Measurement of the structure functions F_2 and xF_3 and comparison with QCD predictions including kinematical and dynamical higher twist effects"; Varvell et al., *Zeit. Phys.* **C36** (1987) 1.

[Whi90] "A Precise Extraction of $R = \sigma_L/\sigma_T$ From a Global Analysis of the SLAC Deep Inelastic eP and eD Scattering Cross-Sections"; L.W. Whitlow et al., *Phys. Lett.* **B250** (1990) 193.

[Whi92] "Precise measurements of the proton and deuteron structure functions from a global analysis of the SLAC deep inelastic electron scattering cross-sections"; L.W. Whitlow et al., *Phys. Lett.* **B282** (1992) 475.

Appendix A

The CCFR/NuTeV Collaboration

R. Johnson, G. Troha and M. Vakili
University of Cincinnati, Cincinnati Ohio 45221

J. Conrad, J. Kim, C. McNulty, A. Romosan, P. Spentzouris, E.G. Stern, M.H. Shaevitz, and A. Vaitaitis
Columbia University, New York NY 10027

R.H. Bernstein, M.J. Lamm, K. McFarland-Porter, W. Marsh and J. Yu
Fermilab, Batavia IL 60510

T. Bolton and D. Naples
Kansas State University, Lawrence, Kansas 66045

D. Buchholz, H. Schellman, G. Zeller
Northwestern University, Evanston Illinois

J. Brau, R. Drucker and R. Frey
University of Oregon, Eugene Oregon 97403

P. Auchincloss, S. Avvakumov, A. Bodek, H.S. Budd, P. DeBarbaro, D. Harris, W. Sakumoto, and U.K. Yang
University of Rochester, Rochester NY 14627

P. Nienaber
Xavier University, Cincinnati Ohio, 45207

Appendix B

Structure Function Tables

Table B.1: F_2 and xF_3 for the central GLS result, including their associated statistical errors.

x	Q^2	F_2	ΔF_2	xF_3	ΔxF_3	$\Delta F_2 \Delta xF_3$
0.0025	1.3	1.3280	0.0638	0.0921	0.0623	-0.002627
	2.0	1.5198	0.1360	0.2107	0.1175	-0.010677
0.0075	1.3	1.2596	0.0282	0.1199	0.0349	-0.000480
	2.0	1.4375	0.0397	0.1461	0.0433	-0.001038
	3.2	1.6777	0.0715	0.0876	0.0676	-0.003444
0.0125	1.3	1.2481	0.0244	0.2036	0.0346	-0.000313
	2.0	1.3951	0.0293	0.2162	0.0370	-0.000470
	3.2	1.5529	0.0381	0.2018	0.0430	-0.000876
	5.0	1.7190	0.0605	0.2836	0.0582	-0.002064
0.0175	1.3	1.2282	0.0236	0.2240	0.0389	-0.000276
	2.0	1.4035	0.0263	0.2831	0.0359	-0.000312
	3.2	1.5503	0.0318	0.2799	0.0396	-0.000530
	5.0	1.5931	0.0428	0.2675	0.0468	-0.001153
	7.9	1.5350	0.0704	0.3717	0.0663	-0.002738
0.025	1.3	1.1884	0.0169	0.2653	0.0357	-0.000190
	2.0	1.3353	0.0173	0.3582	0.0272	-0.000108
	3.2	1.4592	0.0192	0.3489	0.0258	-0.000158
	5.0	1.5755	0.0235	0.3995	0.0289	-0.000260
	7.9	1.6853	0.0334	0.3724	0.0356	-0.000658
	12.6	1.8296	0.0728	0.3445	0.0687	-0.003328

(Continued next page)

x	Q^2	F_2	ΔF_2	xF_3	ΔxF_3	$\Delta F_2 \Delta xF_3$
0.035	1.3	1.1791	0.0182	0.4223	0.0540	-0.000269
	2.0	1.3107	0.0178	0.4294	0.0343	-0.000160
	3.2	1.4072	0.0179	0.4104	0.0268	-0.000118
	5.0	1.5566	0.0205	0.4294	0.0270	-0.000155
	7.9	1.6140	0.0254	0.4572	0.0307	-0.000322
	12.6	1.7305	0.0376	0.4658	0.0387	-0.000738
	20.0	1.8196	0.1021	0.5592	0.0951	-0.005955
0.050	1.3	1.2016	0.0151	0.4318	0.0644	-0.000300
	2.0	1.3371	0.0137	0.5061	0.0361	-0.000111
	3.2	1.4406	0.0131	0.5106	0.0236	-0.000061
	5.0	1.5206	0.0137	0.5291	0.0199	-0.000056
	7.9	1.5939	0.0151	0.5852	0.0197	-0.000073
	12.6	1.6419	0.0193	0.5592	0.0227	-0.000167
	20.0	1.6921	0.0296	0.6297	0.0301	-0.000399
	31.6	1.5770	0.0893	0.6915	0.0838	-0.003771
0.070	1.3	1.3131	0.0267	0.6666	0.1647	-0.001309
	2.0	1.3024	0.0151	0.5158	0.0574	-0.000247
	3.2	1.4004	0.0138	0.6130	0.0325	-0.000080
	5.0	1.4759	0.0134	0.6301	0.0227	-0.000048
	7.9	1.5309	0.0137	0.6608	0.0193	-0.000033
	12.6	1.5321	0.0156	0.6829	0.0201	-0.000058
	20.0	1.5890	0.0207	0.6614	0.0236	-0.000167
	31.6	1.5945	0.0369	0.6187	0.0367	-0.000642
0.090	2.0	1.3113	0.0181	0.7898	0.0898	-0.000436
	3.2	1.3781	0.0149	0.6247	0.0458	-0.000171
	5.0	1.4271	0.0136	0.6847	0.0270	-0.000048
	7.9	1.4547	0.0132	0.7445	0.0204	-0.000013
	12.6	1.4806	0.0144	0.7388	0.0194	-0.000026
	20.0	1.5113	0.0174	0.7514	0.0216	-0.000079
	31.6	1.4969	0.0233	0.7551	0.0249	-0.000156
	50.1	1.5795	0.0674	0.7243	0.0654	-0.002231

(Continued next page)

x	Q^2	F_2	ΔF_2	xF_3	ΔxF_3	$\Delta F_2 \Delta xF_3$
0.110	2.0	1.3429	0.0279	0.5177	0.1719	-0.001534
	3.2	1.3502	0.0162	0.6494	0.0614	-0.000270
	5.0	1.3688	0.0141	0.7333	0.0331	-0.000065
	7.9	1.4046	0.0133	0.7429	0.0225	-0.000020
	12.6	1.4089	0.0136	0.7657	0.0193	-0.000013
	20.0	1.4571	0.0162	0.7498	0.0211	-0.000047
	31.6	1.3713	0.0192	0.7530	0.0220	-0.000098
	50.1	1.5336	0.0378	0.7625	0.0382	-0.000534
0.140	2.0	1.3166	0.0660	0.8561	0.5201	-0.011626
	3.2	1.2900	0.0131	0.7773	0.0637	-0.000226
	5.0	1.3053	0.0104	0.8064	0.0312	-0.000059
	7.9	1.3077	0.0093	0.7801	0.0182	-0.000005
	12.6	1.3236	0.0091	0.8168	0.0140	0.000006
	20.0	1.3041	0.0097	0.8081	0.0132	0.000003
	31.6	1.2740	0.0114	0.8137	0.0142	-0.000008
	50.1	1.2525	0.0157	0.8205	0.0170	-0.000031
	79.4	1.2755	0.0423	0.8202	0.0420	-0.000437
0.180	3.2	1.2227	0.0216	0.8584	0.1374	-0.000867
	5.0	1.1993	0.0113	0.9038	0.0441	-0.000102
	7.9	1.1867	0.0098	0.8041	0.0237	-0.000021
	12.6	1.1930	0.0090	0.8122	0.0156	0.000010
	20.0	1.1696	0.0090	0.8312	0.0129	0.000018
	31.6	1.1473	0.0100	0.8191	0.0132	0.000010
	50.1	1.1013	0.0120	0.8087	0.0141	0.000007
	79.4	1.1092	0.0201	0.7961	0.0208	-0.000009
0.225	3.2	1.1408	0.0946	1.7378	0.7559	-0.017659
	5.0	1.0981	0.0116	0.7815	0.0576	-0.000187
	7.9	1.0646	0.0090	0.7812	0.0275	-0.000033
	12.6	1.0312	0.0078	0.7961	0.0154	0.000012
	20.0	1.0179	0.0075	0.7941	0.0117	0.000013
	31.6	0.9931	0.0079	0.7754	0.0108	0.000020
	50.1	0.9632	0.0091	0.7485	0.0115	0.000015
	79.4	0.9276	0.0115	0.7718	0.0126	0.000038

(Continued next page)

x	Q^2	F_2	ΔF_2	xF_3	ΔxF_3	$\Delta F_2 \Delta xF_3$
0.275	5.0	0.9535	0.0163	0.8482	0.0999	-0.000452
	7.9	0.9247	0.0092	0.7617	0.0349	-0.000056
	12.6	0.8820	0.0078	0.7452	0.0182	0.000006
	20.0	0.8600	0.0071	0.7168	0.0120	0.000021
	31.6	0.8255	0.0072	0.6801	0.0103	0.000023
	50.1	0.8038	0.0080	0.6730	0.0105	0.000024
	79.4	0.7686	0.0093	0.6404	0.0109	0.000025
	125.9	0.7373	0.0167	0.6289	0.0174	0.000086
0.35	5.0	0.8353	0.0357	0.3066	0.2814	-0.004313
	7.9	0.7139	0.0068	0.6166	0.0326	-0.000047
	12.6	0.6709	0.0053	0.6145	0.0157	-0.000004
	20.0	0.6359	0.0046	0.5694	0.0091	0.000008
	31.6	0.6095	0.0045	0.5497	0.0069	0.000012
	50.1	0.5768	0.0046	0.5239	0.0063	0.000012
	79.4	0.5452	0.0051	0.4882	0.0064	0.000011
	125.9	0.5334	0.0069	0.4892	0.0076	0.000026
0.45	7.9	0.4575	0.0091	0.5013	0.0575	-0.000133
	12.6	0.4086	0.0045	0.4005	0.0177	-0.000009
	20.0	0.3897	0.0039	0.3675	0.0094	0.000003
	31.6	0.3596	0.0035	0.3451	0.0061	0.000008
	50.1	0.3311	0.0035	0.3175	0.0051	0.000009
	79.4	0.3167	0.0038	0.3111	0.0049	0.000010
	125.9	0.2959	0.0043	0.2869	0.0051	0.000012
	199.5	0.2755	0.0079	0.2571	0.0083	0.000037
0.55	7.9	0.2601	0.0269	0.3543	0.2106	-0.001631
	12.6	0.2381	0.0039	0.2593	0.0189	-0.000016
	20.0	0.2141	0.0032	0.1918	0.0095	-0.000003
	31.6	0.1894	0.0027	0.1853	0.0052	0.000004
	50.1	0.1761	0.0026	0.1727	0.0040	0.000005
	79.4	0.1599	0.0027	0.1583	0.0036	0.000006
	125.9	0.1514	0.0029	0.1473	0.0036	0.000006
	199.5	0.1321	0.0039	0.1321	0.0043	0.000013

(Continued next page)

x	Q^2	F_2	ΔF_2	xF_3	ΔxF_3	$\Delta F_2 \Delta xF_3$
0.65	12.6	0.1182	0.0034	0.0960	0.0194	-0.000019
	20.0	0.0996	0.0020	0.1157	0.0073	-0.000001
	31.6	0.0844	0.0017	0.0918	0.0038	0.000001
	50.1	0.0782	0.0016	0.0850	0.0027	0.000002
	79.4	0.0686	0.0016	0.0689	0.0023	0.000002
	125.9	0.0615	0.0017	0.0589	0.0022	0.000002
0.75	12.6	0.0479	0.0026	0.0863	0.0173	-0.000009
	20.0	0.0388	0.0011	0.0458	0.0046	-0.000001
	31.6	0.0310	0.0009	0.0301	0.0024	0.000000
	50.1	0.0281	0.0008	0.0273	0.0015	0.000000
	79.4	0.0237	0.0008	0.0224	0.0012	0.000000
	125.9	0.0223	0.0009	0.0233	0.0011	0.000001
0.85	20.0	0.0085	0.0004	0.0094	0.0017	0.000000
	31.6	0.0063	0.0003	0.0077	0.0007	0.000000
	50.1	0.0054	0.0002	0.0061	0.0005	0.000000
	79.4	0.0045	0.0002	0.0045	0.0003	0.000000
	125.9	0.0038	0.0002	0.0035	0.0003	0.000000
0.95	20.0	0.0002	0.0000	0.0003	0.0001	0.000000
	31.6	0.0002	0.0000	0.0003	0.0000	0.000000
	50.1	0.0001	0.0000	0.0001	0.0000	0.000000
	79.4	0.0001	0.0000	0.0001	0.0000	0.000000

Table B.2: F_2 and xF_3 for the acceptance model systematic error.

x	Q^2	F_2	ΔF_2	xF_3	ΔxF_3	$\Delta F_2 \Delta xF_3$
0.0025	1.3	1.4300	0.0678	0.1239	0.0662	-0.002876
	2.0	1.6557	0.1451	0.2582	0.1253	-0.011641
0.0075	1.3	1.3776	0.0313	0.0927	0.0389	-0.000636
	2.0	1.4938	0.0415	0.1434	0.0453	-0.001145
	3.2	1.6831	0.0701	0.1178	0.0663	-0.003197
0.0125	1.3	1.3309	0.0261	0.2066	0.0371	-0.000370
	2.0	1.4053	0.0293	0.2343	0.0370	-0.000451
	3.2	1.5791	0.0392	0.1809	0.0443	-0.000963
	5.0	1.7887	0.0653	0.2408	0.0629	-0.002613
0.0175	1.3	1.3094	0.0256	0.1626	0.0424	-0.000399
	2.0	1.4183	0.0265	0.2905	0.0361	-0.000307
	3.2	1.5901	0.0326	0.2875	0.0407	-0.000560
	5.0	1.6262	0.0436	0.2724	0.0476	-0.001192
	7.9	1.6457	0.0811	0.2876	0.0765	-0.004227
0.025	1.3	1.2339	0.0175	0.2805	0.0370	-0.000200
	2.0	1.3162	0.0171	0.3579	0.0267	-0.000102
	3.2	1.4889	0.0196	0.3560	0.0263	-0.000166
	5.0	1.6042	0.0241	0.3902	0.0297	-0.000287
	7.9	1.6992	0.0332	0.4043	0.0353	-0.000619
	12.6	1.9302	0.0811	0.2593	0.0765	-0.004517
0.035	1.3	1.2038	0.0187	0.4008	0.0554	-0.000301
	2.0	1.3407	0.0184	0.3943	0.0355	-0.000193
	3.2	1.4425	0.0184	0.4129	0.0276	-0.000129
	5.0	1.5759	0.0208	0.4313	0.0274	-0.000162
	7.9	1.6530	0.0262	0.4467	0.0317	-0.000358
	12.6	1.7893	0.0391	0.4760	0.0403	-0.000809
	20.0	1.8233	0.1026	0.5472	0.0955	-0.006079
0.050	1.3	1.2245	0.0153	0.4586	0.0654	-0.000302
	2.0	1.3359	0.0138	0.4739	0.0363	-0.000123
	3.2	1.4628	0.0134	0.4828	0.0242	-0.000073
	5.0	1.5397	0.0139	0.5197	0.0203	-0.000063
	7.9	1.6301	0.0156	0.5670	0.0204	-0.000087
	12.6	1.6467	0.0193	0.5621	0.0227	-0.000167
	20.0	1.7066	0.0298	0.6411	0.0303	-0.000400
	31.6	1.6302	0.0934	0.6727	0.0876	-0.004367

(Continued next page)

x	Q^2	F_2	ΔF_2	xF_3	ΔxF_3	$\Delta F_2 \Delta xF_3$
0.070	1.3	1.3107	0.0266	0.7495	0.1635	-0.001200
	2.0	1.3283	0.0155	0.4757	0.0590	-0.000279
	3.2	1.4005	0.0138	0.5985	0.0326	-0.000084
	5.0	1.4988	0.0137	0.6163	0.0232	-0.000056
	7.9	1.5315	0.0138	0.6477	0.0194	-0.000037
	12.6	1.5481	0.0160	0.6591	0.0206	-0.000073
	20.0	1.6126	0.0211	0.6578	0.0241	-0.000181
	31.6	1.6106	0.0369	0.6562	0.0368	-0.000610
0.090	2.0	1.3273	0.0184	0.7384	0.0915	-0.000486
	3.2	1.3781	0.0150	0.6291	0.0459	-0.000171
	5.0	1.4339	0.0137	0.6997	0.0270	-0.000045
	7.9	1.4534	0.0133	0.7195	0.0205	-0.000020
	12.6	1.4789	0.0143	0.7549	0.0193	-0.000021
	20.0	1.4947	0.0172	0.7580	0.0213	-0.000072
	31.6	1.4918	0.0230	0.7667	0.0246	-0.000140
	50.1	1.5225	0.0595	0.7763	0.0578	-0.001269
0.110	2.0	1.3605	0.0282	0.5676	0.1738	-0.001523
	3.2	1.3451	0.0161	0.6589	0.0611	-0.000262
	5.0	1.3782	0.0142	0.7269	0.0335	-0.000070
	7.9	1.3823	0.0130	0.7536	0.0220	-0.000013
	12.6	1.3976	0.0134	0.7789	0.0190	-0.000006
	20.0	1.4330	0.0158	0.7644	0.0205	-0.000033
	31.6	1.3583	0.0188	0.7632	0.0216	-0.000082
	50.1	1.4717	0.0342	0.8110	0.0345	-0.000284
0.140	2.0	1.3321	0.0666	0.9588	0.5244	-0.011257
	3.2	1.3047	0.0133	0.7154	0.0647	-0.000252
	5.0	1.3012	0.0104	0.7960	0.0312	-0.000060
	7.9	1.3042	0.0092	0.8050	0.0180	-0.000001
	12.6	1.3136	0.0090	0.8403	0.0138	0.000010
	20.0	1.2959	0.0096	0.8302	0.0129	0.000008
	31.6	1.2548	0.0110	0.8320	0.0137	0.000001
	50.1	1.2414	0.0153	0.8362	0.0165	-0.000016
	79.4	1.2655	0.0398	0.8643	0.0394	-0.000183

(Continued next page)

x	Q^2	F_2	ΔF_2	xF_3	ΔxF_3	$\Delta F_2 \Delta xF_3$
0.180	3.2	1.2172	0.0215	0.8366	0.1366	-0.000864
	5.0	1.1959	0.0112	0.9103	0.0439	-0.000100
	7.9	1.1817	0.0097	0.8162	0.0236	-0.000018
	12.6	1.1727	0.0088	0.8404	0.0152	0.000016
	20.0	1.1503	0.0088	0.8399	0.0126	0.000021
	31.6	1.1328	0.0098	0.8380	0.0129	0.000017
	50.1	1.0797	0.0114	0.8261	0.0134	0.000021
	79.4	1.0828	0.0191	0.7926	0.0199	0.000016
0.225	3.2	1.0428	0.0868	1.5754	0.6945	-0.014557
	5.0	1.1010	0.0116	0.7918	0.0578	-0.000188
	7.9	1.0600	0.0090	0.7649	0.0275	-0.000036
	12.6	1.0286	0.0077	0.8013	0.0153	0.000013
	20.0	1.0077	0.0074	0.8210	0.0114	0.000018
	31.6	0.9837	0.0078	0.7882	0.0106	0.000022
	50.1	0.9403	0.0088	0.7550	0.0110	0.000020
	79.4	0.9258	0.0114	0.7829	0.0124	0.000043
0.275	5.0	0.9327	0.0158	0.9008	0.0971	-0.000391
	7.9	0.9099	0.0090	0.7874	0.0341	-0.000046
	12.6	0.8836	0.0078	0.7328	0.0183	0.000003
	20.0	0.8578	0.0070	0.7193	0.0119	0.000021
	31.6	0.8196	0.0072	0.6769	0.0102	0.000022
	50.1	0.8012	0.0080	0.6839	0.0104	0.000027
	79.4	0.7641	0.0092	0.6395	0.0108	0.000026
	125.9	0.7327	0.0166	0.6293	0.0172	0.000089
0.35	5.0	0.8023	0.0342	0.3289	0.2693	-0.003861
	7.9	0.7133	0.0067	0.6193	0.0326	-0.000046
	12.6	0.6711	0.0053	0.5993	0.0158	-0.000005
	20.0	0.6335	0.0046	0.5695	0.0090	0.000008
	31.6	0.6050	0.0045	0.5520	0.0069	0.000012
	50.1	0.5769	0.0046	0.5262	0.0063	0.000012
	79.4	0.5447	0.0051	0.4886	0.0064	0.000011
	125.9	0.5300	0.0069	0.4831	0.0076	0.000025

(Continued next page)

x	Q^2	F_2	ΔF_2	xF_3	ΔxF_3	$\Delta F_2 \Delta xF_3$
0.45	7.9	0.4624	0.0092	0.4985	0.0582	-0.000139
	12.6	0.4113	0.0046	0.3926	0.0179	-0.000011
	20.0	0.3911	0.0039	0.3651	0.0095	0.000003
	31.6	0.3641	0.0036	0.3486	0.0062	0.000008
	50.1	0.3345	0.0036	0.3221	0.0051	0.000009
	79.4	0.3164	0.0038	0.3093	0.0049	0.000010
	125.9	0.2978	0.0044	0.2873	0.0052	0.000012
	199.5	0.2736	0.0078	0.2588	0.0082	0.000039
0.55	7.9	0.2879	0.0308	0.2044	0.2425	-0.003173
	12.6	0.2433	0.0040	0.2754	0.0192	-0.000015
	20.0	0.2162	0.0032	0.1955	0.0095	-0.000002
	31.6	0.1909	0.0027	0.1856	0.0052	0.000004
	50.1	0.1752	0.0026	0.1716	0.0040	0.000005
	79.4	0.1577	0.0026	0.1572	0.0035	0.000006
	125.9	0.1516	0.0029	0.1435	0.0037	0.000005
	199.5	0.1324	0.0039	0.1314	0.0043	0.000013
0.65	12.6	0.1179	0.0033	0.0982	0.0193	-0.000018
	20.0	0.0999	0.0021	0.1128	0.0073	-0.000001
	31.6	0.0834	0.0017	0.0934	0.0037	0.000002
	50.1	0.0775	0.0016	0.0829	0.0027	0.000002
	79.4	0.0697	0.0017	0.0676	0.0023	0.000002
	125.9	0.0609	0.0017	0.0588	0.0022	0.000002
0.75	12.6	0.0497	0.0027	0.0776	0.0183	-0.000013
	20.0	0.0389	0.0011	0.0411	0.0047	-0.000001
	31.6	0.0311	0.0009	0.0325	0.0024	0.000000
	50.1	0.0270	0.0008	0.0283	0.0014	0.000001
	79.4	0.0239	0.0008	0.0225	0.0012	0.000000
	125.9	0.0225	0.0009	0.0219	0.0012	0.000001
0.85	20.0	0.0104	0.0004	0.0140	0.0020	0.000000
	31.6	0.0078	0.0003	0.0079	0.0010	0.000000
	50.1	0.0062	0.0003	0.0070	0.0005	0.000000
	79.4	0.0048	0.0002	0.0049	0.0004	0.000000
	125.9	0.0041	0.0003	0.0036	0.0004	0.000000
0.95	20.0	0.0008	0.0001	0.0004	0.0003	0.000000
	31.6	0.0006	0.0000	0.0003	0.0001	0.000000
	50.1	0.0003	0.0000	0.0004	0.0000	0.000000
	79.4	0.0003	0.0000	0.0003	0.0000	0.000000

Table B.3: xF_3 data from BEBC/Gargamelle [Amm78].

x_{min}	x_{max}	$< x >$	Q^2	xF_3	ΔxF_3
0.00	0.10	0.05	0.15	0.156	0.090
			0.25	0.499	0.107
			0.40	0.304	0.080
			0.60	0.493	0.172
			0.85	0.702	0.216
			1.25	0.457	0.241
			1.75	0.690	0.380
			3.15	0.589	0.160
			7.00	0.608	0.132
			14.00	0.646	0.172
			31.00	0.114	0.220
0.10	0.20	0.15	0.15	0.254	0.363
			0.25	0.818	0.244
			0.40	0.747	0.119
			0.60	0.570	0.107
			0.85	0.549	0.113
			1.25	0.626	0.162
			1.75	0.826	0.352
			3.15	0.453	0.237
			7.00	0.957	0.170
			14.00	0.857	0.114
			31.00	0.848	0.117
			70.00	0.611	0.246
0.20	0.30	0.25	0.15	0.584	0.809
			0.25	-.097	0.538
			0.40	1.499	0.268
			0.60	0.967	0.168
			0.85	0.637	0.112
			1.25	0.477	0.087
			1.75	0.711	0.164
			3.15	0.597	0.140
			7.00	0.961	0.237
			14.00	0.682	0.122
			31.00	0.914	0.081
			70.00	0.652	0.125

x_{min}	x_{max}	$< x >$	Q^2	xF_3	ΔxF_3
0.30	0.40	0.35	0.15	1.092	0.475
			0.25	-1.190	0.871
			0.40	0.839	0.392
			0.60	0.498	0.275
			0.85	0.690	0.153
			1.25	0.640	0.099
			1.75	0.660	0.116
			3.15	0.579	0.613
			7.00	0.479	0.306
			14.00	0.593	0.142
			31.00	0.536	0.064
			70.00	0.672	0.076
0.40	0.60	0.50	0.25	0.090	0.489
			0.40	-.183	0.409
			0.60	1.116	0.309
			0.85	0.908	0.179
			1.25	0.887	0.100
			1.75	0.440	0.068
			3.15	0.377	0.046
			7.00	0.242	0.075
			14.00	0.460	0.097
			31.00	0.219	0.036
			70.00	0.269	0.035
0.60	1.00	0.80	0.40	-.109	0.056
			0.60	0.192	0.230
			0.85	0.235	0.121
			1.25	0.272	0.064
			1.75	0.123	0.043
			3.15	0.092	0.014
			7.00	0.077	0.023
			14.00	0.034	0.048
			31.00	0.034	0.013
			70.00	0.024	0.006

Table B.4: xF_3 data from FNAL-E180 [Amm82].

x_{min}	x_{max}	$< x >$	Q^2	xF_3	$\Delta xF_3 f$
0.00	0.10	0.05	0.3	0.82	0.54
			0.5	0.78	0.51
			0.8	0.61	0.30
			1.5	1.04	0.25
			2.5	0.61	0.26
			3.5	0.61	0.33
			5.0	0.27	0.25
			7.6	0.67	0.27
			13.8	1.10	0.50
0.10	0.20	0.15	1.5	0.90	0.40
			2.5	0.69	0.31
			3.5	0.40	0.29
			5.0	0.78	0.23
			7.6	0.81	0.19
			13.8	0.74	0.18
			24.3	0.60	0.30
0.20	0.30	0.25	2.5	1.03	0.50
			3.5	0.95	0.39
			5.0	0.52	0.23
			7.6	0.40	0.18
			13.8	0.69	0.15
			24.3	0.47	0.18
			37.5	0.54	0.21
0.30	0.40	0.35	2.5	0.47	0.64
			3.5	0.67	0.48
			5.0	0.49	0.30
			7.6	0.56	0.19
			13.8	0.79	0.15
			24.3	0.52	0.15
			37.5	0.66	0.19
			66.0	0.41	0.17
0.40	0.50	0.45	3.5	0.31	0.30
			5.0	0.55	0.37
			7.6	0.47	0.18
			13.8	0.29	0.10
			24.3	0.20	0.10
			37.5	0.17	0.09
			66.0	0.18	0.10
0.50	0.60	0.55	3.5	0.32	0.58
			5.0	0.21	0.25
			7.6	0.25	0.15
			13.8	0.24	0.09
			24.3	0.21	0.09
			37.5	0.15	0.09
			66.0	0.16	0.09
0.60	0.70	0.65	5.0	0.41	0.32
			7.6	0.11	0.09
			13.8	0.05	0.05
			24.3	0.14	0.13
			37.5	0.10	0.06
			66.0	0.08	0.06

Table B.5: xF_3 data from SKAT [Amm86].

x_{min}	x_{max}	$< x >$	Q^2	xF_3	$\Delta xF_3 f$
0.00	0.10	0.05	0.15	0.399	0.281
			0.28	0.398	0.133
			0.56	0.338	0.127
			0.94	0.552	0.252
0.10	0.20	0.15	0.25	0.801	0.503
			0.45	0.837	0.311
			0.84	0.685	0.145
			1.69	0.962	0.125
			2.82	1.011	0.222
0.20	0.30	0.25	0.42	0.638	0.496
			0.75	1.041	0.278
			1.41	1.140	0.127
			2.82	0.927	0.113
			4.69	0.924	0.190
0.30	0.40	0.35	1.05	0.596	0.240
			1.97	0.514	0.122
			3.94	0.592	0.088
0.40	0.60	0.50	1.50	0.392	0.105
			2.82	0.489	0.057
			5.63	0.371	0.042
0.60	0.80	0.70	3.94	0.110	0.024
			7.88	0.106	0.028

Table B.6: xF_3 data from WA25 [All85].

x_{min}	x_{max}	$< x >$	Q^2	xF_3	$\Delta xF_3 f$
0.00	0.06	0.030	1.5	0.380	0.076
			3.0	0.398	0.084
			6.0	0.296	0.120
			11.0	0.255	0.237
0.06	0.10	0.080	1.5	0.611	0.117
			3.0	0.508	0.089
			6.0	0.542	0.089
			11.0	0.632	0.116
			24.0	0.660	0.286
0.10	0.15	0.125	1.5	0.645	0.151
			3.0	0.611	0.095
			6.0	0.688	0.080
			11.0	0.720	0.082
			24.0	0.485	0.117
0.15	0.20	0.175	1.5	0.717	0.241
			3.0	0.704	0.117
			6.0	0.755	0.082
			11.0	0.699	0.076
			24.0	0.565	0.079
0.20	0.30	0.250	1.5	0.432	0.260
			3.0	0.874	0.105
			6.0	0.831	0.065
			11.0	0.679	0.051
			24.0	0.699	0.052
			55.0	0.535	0.089
0.30	0.40	0.350	1.5	0.975	0.405
			3.0	0.365	0.146
			6.0	0.624	0.068
			11.0	0.639	0.049
			24.0	0.442	0.038
			55.0	0.575	0.058
0.40	0.50	0.450	6.0	0.573	0.076
			11.0	0.467	0.045
			24.0	0.372	0.031
			55.0	0.305	0.038
0.50	0.60	0.550	6.0	0.258	0.073
			11.0	0.300	0.040
			24.0	0.269	0.026
			55.0	0.180	0.026
0.60	0.80	0.700	6.0	0.099	0.038
			11.0	0.099	0.019
			24.0	0.090	0.011
			55.0	0.059	0.010

Table B.7: xF_3 data from WA59 [Var87].

x_{min}	x_{max}	$< x >$	Q^2	xF_3	$\Delta xF_3 f$
0.00	0.05	0.028	0.79	0.313	0.125
			1.47	0.498	0.110
			2.91	0.374	0.123
			5.73	0.512	0.170
0.05	0.10	0.076	0.79	0.529	0.230
			1.47	0.659	0.127
			2.91	0.547	0.100
			5.73	0.661	0.114
			11.28	0.715	0.143
0.10	0.20	0.149	1.47	0.769	0.163
			2.91	1.023	0.096
			5.73	0.767	0.071
			11.28	0.851	0.078
			22.32	0.883	0.095
			43.54	0.941	0.218
0.20	0.30	0.248	1.47	0.750	0.309
			2.91	1.001	0.137
			5.73	0.860	0.076
			11.28	0.812	0.064
			22.32	0.829	0.071
			43.54	0.691	0.090
0.30	0.40	0.347	2.91	0.773	0.176
			5.73	0.699	0.086
			11.28	0.585	0.053
			22.32	0.682	0.057
			43.54	0.684	0.066
0.40	0.50	0.447	2.91	0.537	0.221
			5.73	0.298	0.081
			11.28	0.384	0.047
			22.32	0.365	0.043
			43.54	0.405	0.047
0.50	0.60	0.545	5.73	0.257	0.082
			11.28	0.207	0.042
			22.32	0.176	0.029
			43.54	0.206	0.033
0.60	0.70	0.649	11.28	0.087	0.034
			22.32	0.093	0.022
			43.54	0.078	0.020

Appendix C

Detector Material

This is an overview of the exact composition of the CCFR calorimeter. The exact material is important for the simulation of muon energy loss in the Monte Carlo which is a basis for energy calibration. All of the Monte Carlo's on CCFR have used the same calculation for dE_μ/dX. This M. Mugge's FORTRAN routine "`DEDX`" (used in the old Fast MC, NCMONTE, and NUMONTE). However, there are significant differences between how this is used: the defined input and modifications to the operation and output.

There are three inputs to the DEDX calculation:

LENGTH is the amount of material which the muon passes through, in units of inches of iron. This is set based purely on the mass of the detector and dividing by the density of iron. In this analysis, LENGTH was set to 4.412 inches per counter within the calorimeter.

SCALE1 is the ratio of restricted energy loss in the detector versus restricted energy loss for an equivalent mass of pure iron. This is obviously 1 for pure iron, and was set to 1.005 based on the average $dE/dX\ |_{min}$ of all the detector materials.

SCALE1 is the ration of catastrophic energy loss in the detector versus such loss in pure iron. This was set to 0.949 based on the average radiation length of all the detector materials.

DEDX was designed to simulate muon energy loss in iron. Other materials besides iron can be approximated by this routine by altering the values of SCALE1 and SCALE2. For iron SCALE1 and SCALE2 should be set to 1.0 (a DATA statement does this so no need to set unless you change it.) To model other materials or compounds, the following procedure is used:

1. Set grams to equivalent amount of iron that this material corresponds to for purposes of pair production and brem.
2. Set SCALE1 to scale non-stocastic ionization losses for this material, I.E.
   SCALE1=(non-sto ion loss)/grams/(non-sto for iron)
3. Set SCALE2 to scale the stocastic ionization losses for this material, I.E.
   SCALE2=(sto prob for material)/grams/(sto prob for iron)

A study is in progress to see if the DEDX correction factor used in NUMONTE is still neccessary, since the GEANT-based correction has been removed in favor of this more first-principles-based calculation. DEDX takes as input LENGTH which is in units of equivalent inches of steel. Thus, the basis of comparison would be how many of these are within each unit of our detector.

C.1 Calculating Correct LENGTH

The length variable and scale factors must be set by closely examining the material in the detector. Table C.1 (on its own page) shows a breakdown of the materials in a single 'unit' of the detector. This consists of two scintillation counters and one drift chamber.

Table C.1 breaks apart the materials into their constituent elements. The $dE/dX\ |_{min}$ is as listed in the Particle Data Book's table: "Atomic and Nuclear Properties of Materials".

The inverse radiation length, $1/X_0$, is taken from the EGS manual (R.Ford and W.Nelson SLAC 210, UC 32. SLAC, June 1978) as printed in the GEANT manual p48.

$$\frac{1}{\rho X_0} = 4\alpha r_0^2 N_{Av} \frac{1}{A} Z(Z + \xi(Z)) \left[ln \frac{183}{Z^{1/3}} - F_c(Z) \right] \tag{C.1}$$

where X_0 is radiation length (in cm); ρ is density in gcm^{-3}; α is the fine structure constant; r is the classical electron radius (in cm); N_{Av} is Avogadro's number; A is atomic weight; Z is atomic number; and $F_c(Z)$ is the Coulomb correction function.

$$F_c(Z) = (\alpha Z)^2 \left[\frac{1}{1 + (\alpha Z)^2} + 0.20206 - 0.0369(\alpha Z)^2 + 0.0083(\alpha Z)^4 - 0.0020(\alpha Z)^6 \right] \tag{C.2}$$

$$\xi(Z) = \frac{ln \frac{1440}{Z^{2/3}}}{\ln \frac{183}{Z^{1/3}} - F_c(Z)} \tag{C.3}$$

AMOL is the effective atomic weight per molecule of the material.

Aeff is the effective atomic weight of the material, the weighted average of the atomic weights.

Zeff is the weighted average of the Z of materials.

Neff is the weighted average of N, the number of neutrons. Note that because of the neutron-proton weight difference, $Neff + Zeff \neq Aeff$.

rho is the density in g/cm^3.

X0 is the radiation length, shown in g/cm^2 and in cm.

T is the thickness per detector unit, in g/cm^2 (i.e. density times thickness in centimeters).

RL is the number of radiation lengths per unit of the detector (i.e. two scintillation counters with associated iron plus one drift chamber), calculated using the numbers for X0 above. **RL%** is the percentage of the total RL due to that material.

RHOT

$dedx(GeV)$ is the ionization loss per one unit of the detector, as defined by the Bethe-Block formula at $10GeV$.

Now, to make use of these numbers in `DEDX`, we will be making use of two variables, `SCALE1` and `SCALE2`. These are designed to alter the response of the routine to mimic materials other than iron. This procedure is outlined in the routine itself.

C.2 Previous Estimates

In previous analyses, there were several differing calculations of the detector material.

Old Fast MC: $LENGTH = \Delta Z/1.838$ (inches of steel)

$< LENGTH > = 4.531$ (inches of steel) (average per counter)

The factor of 1.838 is set by a variable called SCALE, which is stored in MCPAR.CMN and set in various routines.

NCMONTE: $LENGTH = 4$ (inches of steel per counter)

This length is clearly not correct, since it does not incude any non-steel material. NCMONTE uses two corrections to the process which adjust for this. The corrections are:

- **GEANT-based Correction to DEDX output** in TARSTEP

```
C..add in correction for loss in ctrs, water bags, and chambers
C..(correction is from T.Bolton GEANT study 6/21/91)
      EDXT = EDXT * (1.101843-.00433*LOG(EST))
```

  The GEANT correction somewhat inconsistantly applied. It modifies EDXT, which is the *total* muon energy loss. However, it does not modify EDCAT, the *catastrophic* energy loss which is summed for use in hadron energy calculations, for example.

- **Internal Correction to DEDX Calculation**

```
cx..fudge factors   06/26/1992  CGA
        if(e.lt.250.)then
          fudge=1.015
        else
          fudge=1.010
        endif
        ppergm=fudge*ppergm
```

  This correction is based on an end comparison of the DEDX in the Data versus the DEDX from "`trackmu.f`" in the Monte Carlo.

DETECTOR MATERIAL SUMMARY																	
element	*AMOL*	*Aeff*	*Zeff*	*Neff*	*rho*	*X0(gm/cm^2)*	*X0(cm)*	*T (g/cm^2)*	*RL*	*% RL*	*RHOT*	*% RHOT*	*dedx (GeV)*	*%dedx*	*moles/cm^2*	*p/cm^2*	*n/cm^2*
Steel(Fe)	55.638	55.638	25.899	29.801	7.870	13.850	1.760	20.684	11.753	96.51%	162.781	92.07%	0.3242	91.03%	2.926	75.773	87.188
Scint. Oil (CH(1.8))	13.800	10.585	5.348	5.232	0.840	40.697	48.448	5.080	0.105	0.86%	4.267	2.41%	0.0099	2.79%	0.309	2.412	1.860
Water(H2O)	18.015	14.321	7.217	7.109	1.000	35.999	35.999	5.080	0.141	1.16%	5.080	2.87%	0.0117	3.29%	0.282	2.820	2.258
Lucite(C5H8O2)	100.117	12.399	6.236	6.164	1.180	39.700	33.644	1.280	0.038	0.31%	1.510	0.85%	0.0035	0.97%	0.015	0.815	0.695
Mylar(C5H4O2) +++	96.085	12.877	6.456	6.423	1.390	39.092	28.124	0.110	0.004	0.03%	0.153	0.09%	0.0003	0.10%	0.002	0.080	0.073
Polyethylene(C2H4)	28.054	10.430	5.281	5.147	0.940	43.376	46.145	0.200	0.004	0.04%	0.188	0.11%	0.0004	0.12%	0.007	0.107	0.081
Al-Hexcel	26.982	26.982	13.000	14.000	2.700	23.877	8.843	0.320	0.036	0.30%	0.864	0.49%	0.0018	0.52%	0.032	0.416	0.448
Al-I beams	26.982	26.982	13.000	14.000	2.700	23.877	8.843	0.055	0.006	0.05%	0.148	0.08%	0.0003	0.09%	0.005	0.071	0.077
Copper Cladding	63.546	63.546	29.000	34.618	8.960	12.849	1.434	0.000	0.000	0.00%	0.003	0.00%	0.0000	0.00%	0.000	0.001	0.001
Wires*	63.546	63.546	29.000	34.618	8.960	12.849	1.434	0.080	0.056	0.46%	0.714	0.40%	0.0014	0.39%	0.011	0.326	0.389
G10(Si(0.60)O(2.2)C(1)H(2)	66.076	17.899	8.953	8.955	1.700	31.064	18.273	0.635	0.035	0.29%	1.080	0.61%	0.0024	0.68%	0.016	0.555	0.524
DC Gas (ArC2H6)	70.018	27.000	12.415	14.606	0.002	25.673	16045	2.858	0.000	0.00%	0.005	0.00%	0.0000	0.00%	0.000	0.002	0.002
Air(N(0.79)O(0.21))**	13.588	15.363	7.679	7.683	0.001	34.791	26970	6.050	0.000	0.00%	0.008	0.00%	0.0000	0.01%	0.001	0.004	0.004
TOTAL								42.432	12.179	1.000	176.800	1.000	0.356	1.000	3.606	83.382	93.601
TOTAL MASS	689.86	MT															
TOTAL THICKNESS	17.82	m															
DENSITY	4.17	g/cm^3															
RADIATION LENGTHS	6.09	/counter															
(N-Z)/(N+Z)	5.77	percent															
IONIZATION LOSS	8.39	MeV/cm															

Table C.1: Detector material summary table.